Development of Compliant Mechanism for Real-Time Machine Tool Accuracy Enhancement Using Dual Servo Principle

ARAVIND RAGHAVENDRA M.R.
(*B.Eng., AU*)

A THESIS SUBMITTED

FOR THE DEGREE OF DOCTOR OF PHILOSOPHY

DEPARTMENT OF MECHANICAL ENGINEERING

NATIONAL UNIVERSITY OF SINGAPORE

2013

DECLARATION

I hereby declare that this thesis is my original work and it has been written by me in its entirety.

I have duly acknowledged all the sources of information which have been used in the thesis.

This thesis has also not been submitted for any degree in any university previously."

Aravind Raghavendra M R

ACKNOWLEDGEMENTS

First of all, I want to express my sincerest gratitude to my advisor, Associate Professor A. Senthil Kumar for his insightful input and guidance, and most importantly for his confidence in the direction of my research work throughout the duration of my research. He has supported me extensively throughout my thesis with his patience and knowledge whilst allowing me the room to work in my own way. His friendly approach and advices provided me a platform to view the life from a different perspective. Without his supervision and extended support, this dissertation would not have been possible.

I feel this thesis is incomplete without thanking Dr. P.M. Beulah Devamalar, who has been a motivator and well-wisher to me since my undergraduate days. I would not have pursued my research without her advice and constant push to get elevated. She is always an inspiration for me and will be a continuous source of inspiration.

I would like to thank Mr. Suresh Babu who has been my undergraduate guide, who made me to realize my potential. His involvement and support during my undergraduate project had taught me so many things about being a good teacher. I would follow your footsteps to be an effective and inspirational teacher, sir. I would like to thank all my teachers who had been instrumental in nurturing me to be a good human being.

These set of people are important part of my life and without them I am incomplete. Dr. Rajasekar (Just a thanks is not enough, Brother), Mr.Venkatesh Krishnamoorthy, Mr.Mohan Gunasekaran, Dr. Karthikeyan, (who had been a source of positive energy in my research life), Mr. Vignesh,

Mr. Nishanth, Mr. Selvakumar and his family, Mr. Dinesh, Mr. Krishna, Dr.OPK whom I cannot just thank. I am indebted to them throughout my life. I would not have completed this thesis without their love, affection and yes support as well (not only technically but personally as well). They helped me stay sane through these difficult years and their care helped me overcome setbacks and stay focused on my graduate study. They made my stay in Singapore as a best home which I could not have relished without accepting to do my PhD. More than being friends, you all made me feel like my own brother.

I would like to thank National University of Singapore and the Minister of Education (MOE) for providing me an opportunity to pursue my PhD and for their financial support. I also thank the Department of Mechanical Engineering and the Mikrotools Pte. Ltd. who have provided the support and equipment which I have needed to complete my thesis. I personally thank Ms.Sharen of Mechanical department and Ms. Azzlina, for being systematic with procedures and helping me with the administrative processes throughout my candidature. Thank you for your strenuous efforts which I will not forget in my lifetime.

Without mentioning these names, I am not rightful. Mr.Prakash Chandar, thank you for being a very good friend and supportive during the most difficult period of my life. I owe you so much in life. Mr. Balaji Mohan, Mr. Willson, Mr. Hari, Ms. Yuvareka, Mr. Aravindh Swaminathan, Dr. Karthik Somasundaram and Mr. Sasitharan who had helped me out of the way to successfully complete this thesis. Thank you everyone.

A special mention of Dr. Ramesh & Dr. Soneela Ramesh is inevitable for their timely help and motivation during my difficult period which helped me to finish this thesis. Thank you both of you so much. A special thanks to my roommate, Dr. Sucheendra for tolerating all my mood-swings and my blabbering about my research. Thank you Doc.

I would like to thank Dr. Venkata Rayalu for his critical comments about my research, which helped me in many ways to answer the technicality of my research. I want to acknowledge several machinists from Fabrication supports lab, Mr. Lam, Mr. Lobo, Mr. Raja, Mr. Rajendran for their contribution to the hardware made for this thesis and to my learning. I would like to Thank Mr. Weiyong, Mr. Vijay and Ms. Nora from Mikrotools for helping me in conducting my experiments.

Writing this thesis was not a lonely experience as it could have been because of the cherished labmates Mr.Dennis Neo, Mr.Akshay, Mr.Afzal, Mr. Genglin, Ms. Zhong Xin, Ms. Wang Yan and many others who provided enthusiasm and empathy in just the right doses. Thank you all my friends in Singapore and India and in Facebook. I would like to thank "google.com" for the limitless support with which the search/answers for many of my research needs were found at a mouse click. Thank you Larry Page and Sergey Brin for understanding the graduates' needs.

Most importantly, none of this would have been possible without the patience of my mom and dad to whom this dissertation is dedicated to. Special thanks to you, Jan. I would like to express my heart-felt gratitude to my family for all that you have taught me in life.

"THANK YOU GOD FOR PROVIDING ME THE STRENGTH"

Dedicated

To My Friends whom I consider as my Family

And

My Teachers

Contents

SUMMARY

The quality of machined precision components is defined by the degree of accuracy of the machine tools used in its manufacturing process. So every process and its corresponding machine tool, needs to maintain the high degree of accuracy and precision in order to realize the end product with the desired surface quality. The cost of manufacturing and maintenance of such high precision tools defines the cost of the finished product. Hence the product cost and machine tools accuracy has its own tradeoffs. Real-time error compensation technique is well applauded for its efficiency in improving the machine tools quality without an increase in its cost. But the accuracy of such compensation technique depends on the resolution of the machine tool system. Hence, to effectively improve the accuracy of the machine tool without an increase in initial investment, a real-time compensation based on auxiliary axis using proven precision compliant mechanism will be effective.

Diamond turning machines (DTM) are widely used in high precision optics and energy sectors due to its single step final finishing process to produce mirror-finish surfaces. Though the capabilities of using the DTM are manyfolds, still its cost is sky-high. To improve the surface integrity of machined components in DTM and to reduce the initial cost of machine a dual servo based real-time compensation system is developed and the outcome of the implementation are presented in this thesis. Single axis fine tool servo (FiTS) system is developed, analyzed and implemented in the DTM for improving the surface quality. Mirror finished flat-faces are produced with

combined real-time geometric and kinematic error compensation and pre-compensation techniques.

Novel efficient compliant mechanism module called “Inverted Double Parallelogram” was introduced and the performance study of the new design revealed that for both axial and transverse loading, parasitic error, which is one of the important aspect in deciding the accuracy of the compliant mechanism is reduced significantly.

The accuracy of a basic DTM is determined by its two motion slides (X and Z). Hence, a dual axis complainant mechanism is required to compensate the errors of the axes. Effective actuator isolation and avoidance of cross-axis error is critical in designing a dual axis complaint mechanism. A dual axis compliant, planar mechanism is developed and successfully implemented in real-time dual servo error compensation of DTM during contour machining operation.

The design, development, analysis and implementation of the single and dual axis FiTS systems on DTM, together with the findings on the improvements of the machined workpiece quality are presented in this thesis.

List of Tables

List of Figures

Nomenclature

r	Radius of the Hinge
t	Web Thickness
b	Thickness of full circular Hinge
K	Stiffness of the material
K_B	Bending Stiffness of the flexure hinge
K_A	Axial Stiffness of the flexure hinge
E	Young's Modulus of the material
R_a	Surface Roughness
f	feed per tooth
R_t	Peak to valley Roughness
d	Depth of cut

Abbreviations

CAD	Computer Aided Design
CNC	Computer Numeric Control
CPU	Central Processing Unit
DAQ	Data Acquisition
DOC	Degree of Constraint
DOF	Degree of Freedom
DSP	Digital signal processor
DTM	Diamond Turning Machine
EDM	Electric Discharge Machining
FEA	Finite Element Analysis
FEM	Finite Element Method

GUI	Graphical User Interface
HMI	Human Machine Interface
HVPZT	High Voltage Piezo-electric actuator
FTS	Fast tool servo
FiTS	Fine tool servo
LVDT	Linear Variable Differential Transducer
MEMS	Micro Electro Mechanical Systems
MDI	Manual Data Input
MLA	Micro Lens Array
MPA	Micro Pyramid Array
PEA	Piezo-electric actuator
PID	Proportional Integral derivative
PLC	Programmable Logic Controller
PSD	Photo Sensitivity Detector
PRBM	Pseudo Rigid Body Model
PWM	Pulse Width Modulation
RTC	Real Time Computer
RTI	Real Time Interrupt
RAM	Random Access Memory
STS	Slow Tool Servo
VCM	Voice Coil Motor

Chapter 1 Introduction

1.1 Background

Ever since the onset of human civilization, manufacturing has been an integral part of the modernization. Starting with the invention of wheel to the current day sophisticated mission critical aero-space components, bio-medical implants and high performance computers, manufacturing technology improves with every single second to new heights, in terms of product capability, accuracy and precision levels meeting the market demands. Precision manufacture of components has become a necessity in the present day manufacturing sector. The ever-increasing demand for precision manufacturing in fields such as automobile (efficient fuel systems), energy (effective energy collector systems), computing (high data storage capabilities), bio-medical (implants and artificial organs) and space applications (optics and multitasking systems) have forced researchers to come up with more improved innovations.

Most of the current day components (Figure 1-1) require more than one single process to transform the raw material to the finished product. So every single machine tool in this process cycle needs to maintain the high degree of accuracy and precision in order to realize the end product with the desired surface quality. Building such an ultra-precision machine with absolutely no error tends to increase the cost of the machine which in return increases the cost of the components too.

Figure 1-1: High Precision components

So in conjunction with the above mentioned precision needs, the demand for developing ultra-precision machine tool to cater their manufacturing are rapidly expanding. Improved design methodologies and advanced materials technology has revolutionized machine tool industry which is striving hard to achieve the sub-nanometric regime as mentioned by Norio Taniguchi [1] who coined the term "Nano-technology" in late 1970s. He studied the historical progress of the manufacturing technology and predicted its future trends.

The machining accuracy was classified based on the accuracy needs/level into a) *normal machining*, b) *precision machining* and c) *ultra-precision machining*. As the years increment, the accuracy and repeatability needs of the product gets stringent and complex to achieve. The current trend in precision technology is defined by the trends in IC technology, information display and storage, MEMS, bio-medical engineering and customer product needs [2]. Currently sub-nanometric (<0.001µm) accuracy levels are required in all the precision manufacturing industries. In order to achieve such stringent levels of accuracy, a precise machine tool with closed-loop control system

needs to be incorporated into the machining stream through which an accurate position, acceleration and velocity control can be achieved between tool and work piece. Apart from closed loop control, the accuracy of the components used in the machining system such as guideway, bearings and measuring equipment should be as accurate as the target accuracy itself [1]. The graph (Figure 1-2) lists the machines, measuring instruments, processing equipment and achieved machining accuracy over the past 70 years (1910-1980) and the future development was predicted by extrapolating the graph.

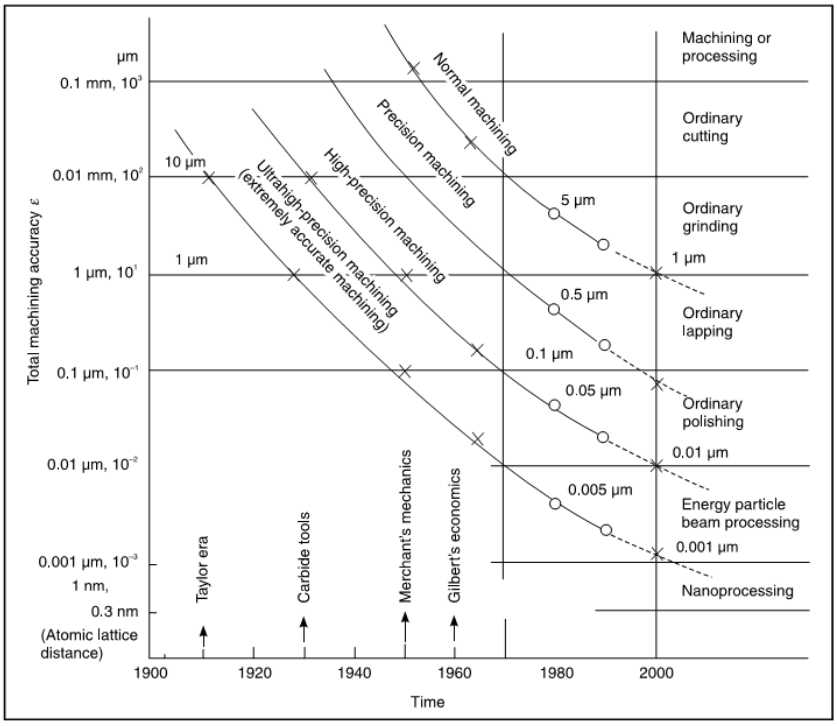

Figure 1-2: Trend of achievable machining accuracy over years [1]

The challenges faced by the machine tool industry to achieve the stringent accuracy and precision needs provide tremendous opportunities to researchers. In any mechanism, the ultimate objective of the designer is to provide maximum displacement in the desired direction – *Degree of Freedom (DOF)* and maximum constraint in all other directions – *Degree of Constraint (DOC)*. To explain DOF and DOC, an example of a linear slideway used in

machine tool is considered (Figure 1-3). The main objective of an ideal slideway is to provide friction-less, long range of motion in “X” direction (green coloured arrow) and no motion in rest of linear “Y” and “Z” direction (red coloured arrow) or rotation motion along X,Y and Z directions. So by the above definition, “X” is the direction of DOF since the slideway is intended to have motion only along “X” and all others represent the directions of DOC. And the motion along these directions leads to parasitic erroneous motion which deviates from the desired motion. But in practical scenario, ideal motion along direction of DOF is affected by factors such as friction, stiction and backlash. Also the constraint along the DOC is not only mechanical but also by process and environment based influences. Thus the performance characteristics of the slideway deteriorate along with the precision of the machine tool.

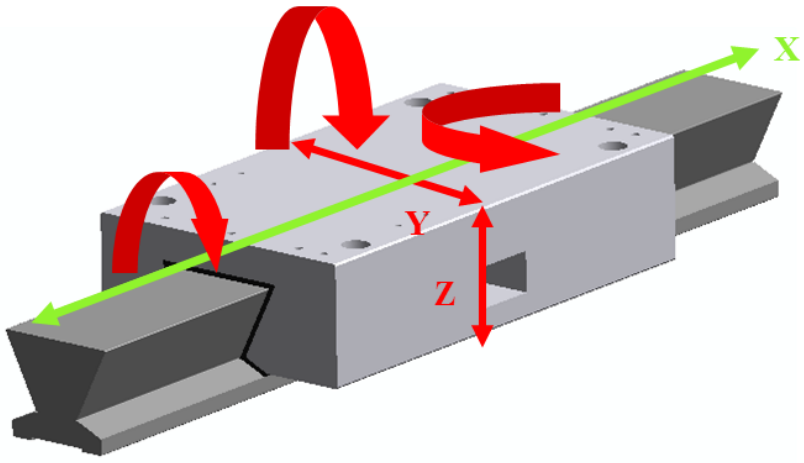

Figure 1-3: Conventional Guideways with DOC and DOF

Even in the linear guideway used in modern precision machines, the accuracy (that) can be achieved in terms of tens of nanometer. Still large portions of error co-exist with the system because of assemblies involved in every single component of a precision machine. For example, a high-precision linear ball-screw or guideway has components like recirculating balls, lead-screw, seals

etc. which need to comply with the target accuracy of the product. Assembly of these various components will lead to additional errors due to clearance, misalignment, wear along with heat generation because of friction between the components., Moreover the straightness error along the axis and perpendicularity between the axes further deteriorates the overall accuracy of the system and hence the final machined component. Though the improved design methodologies and advanced materials technology in this field has revolutionized machine tool industry, the inherent error in each of the design and components add upto a cumulative effect of error that is reflected on the finished product during the machining process. So in order to achieve the required accuracy and precision, the machine designer needs to consider the following points while designing any mechanism for machine tool:

1) Reducing the part count/assembly
2) Friction-free motion
3) Improving the accuracy of each components
4) Alternative design from existing series type mechanisms (parallel mechanisms)
5) Compliant mechanism design in contrast to conventional rigid body design

1.2 Machine Tool Errors

The accuracy of the machined components is influenced by various factors. Process, Environment and Machine tool based influences forms the main bottleneck in achieving the precision needs (Figure 1-4). Since the process and environment based influences on the surface accuracy is sporadic

and widely dependent on the location and the operating conditions, the accuracy enhancement methodologies become process/condition specific, thus they constitute a separate area of research focus. Furthermore, these factors are transmitted to the workpiece through the machine tool and workpiece interaction. Hence for effective improvement of workpiece accuracy, error elimination caused due to the influence of machine tool plays a vital role.

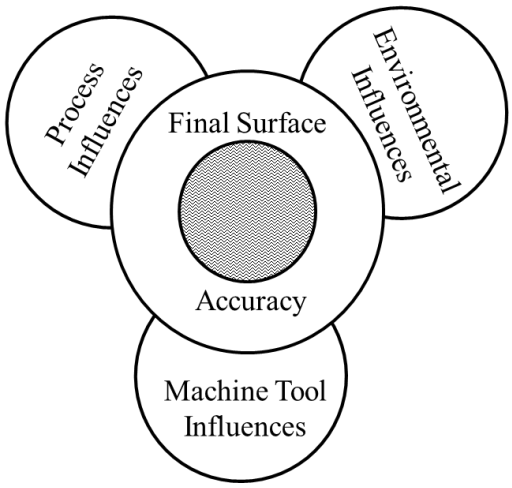

Figure 1-4: Factors influencing the workpiece surface accuracy

The final surface accuracy of the workpiece is defined at the machine and tool interface zone; hence the performance of the machine tool is the key to achieve the precision requirement

1.3 Classification of Machine tool errors

Machine tool errors are generally classified into two main categories a) systematic and b) random error[1]. The systematic error is the bias in the measurement due to an imperfect calibration, environmental change and imperfect method of observation of measurement *e.g.* zero setting error while tool positioning. Systematic errors can be measured and stored for effective compensatory actions [3]. The random error or the unpredictable error occurs

due to mechanical and dynamic servo errors of the close-loop system. The phenomenon such as stick-slip, friction, backlash, wear, vibration and servo error predicts the dynamic behavior of the system. Systematic error can be eliminated from the system by using a feed-back control system but the random errors are difficult to predict, measure and control. So the machine's accuracy level is limited based on the amount of random error present in it. The main cause for random error is the assembly of components such as bearing, guideways, lead-screw etc. in the machine tool. The tendency of the error in each of these components get stacked up, deteriorating the overall accuracy of the machine tool. Hence, to improve the workpiece surface integrity, one needs to reduce the random error of the machine tool close to the target accuracy itself.

1.4 Sources of Machine tool error

Though there are various sources of errors associated with the machine tool, the principal sources of error associated with the machine tools are as follows:

1) Geometric/Kinematic error such as positioning inaccuracy, following error, axes straightness etc.
2) Thermal error based structural deformation
3) Static behavior based error such as deflection between structural loop under the influence of cutting forces, slide weight etc.
4) Dynamic behavior based errors due to compliance, improper clamping force, internal vibration, servo errors etc.

The basic inaccuracy of the machine tool is due to the geometric error which is one form of quasi-static error and it accounts for 70% of the total error [4]. Due to the availability of sophisticated controlled environments such as temperature control using efficient cooling systems, passive and active vibration isolators, the influence of the thermal and environment based errors can be ignored. Also the machining force based errors are minimal since the high precision machined surfaces require sub-micron depth-of-cut which produces few tens of micro newton cutting force.

1.5 Machine tool accuracy enhancement approaches

Accuracy could be defined as the degree of agreement or conformance of a finished part with the required dimensional and geometrical accuracy [5]. Error in machine tool is the deviation in the position of the cutting edge from the theoretically required value to produce a workpiece of the specified tolerance. There is an exigency in the identification and elimination of all sources of imprecision in machine tools in order to achieve the required accuracy. There are various approaches which can be implemented to eliminate the imperfections. Error avoidance and error monitoring and compensation methodologies are the most commonly used approaches to achieve the accuracy needs.

1.5.1 Error Avoidance

Error avoidance is the technique applied during the design and manufacturing stage which focuses to minimize the sources of inaccuracy in the machine tool. A high degree of investment is incurred which rises exponentially with the level of accuracy involved. Such machines also tend to

be frequently overdesigned resulting in higher cost. From the previous discussion, the precision and accuracy of such highly designed machined does not only depend on its structural loop, but also on operating conditions and environmental factors on a long run. Errors like thermal deformation, cutting force deformation etc., cannot be completely accounted for by detailed design. In the most common practice of machine tool building, use of materials like ceramics, concrete and granite in machine tool components like spindles and machine tool beds attracts popularity. These changes are still incapable of catering to changes in the shop floor environment and continue to be a challenge. Moreover, the manufacturing costs involved in such an endeavor are also considerably large. No matter how well a machine is designed, these factors limit the accuracy that could be achieved. So maintaining such high precision at lower cost becomes difficult.

1.5.2 Error Monitoring and Compensation

Another option that is achieving greater success these days, both on account of effectiveness in workpiece surface integrity improvement as well as its cost is the Error compensation technique. Unlike the case of error avoidance, excessive effort to avoid the error is not attempted. Rather, error is allowed to occur and the same is measured and compensated for. The main advantage of error compensation in machine tools is its cost effectiveness compared to building of a perfect machine starting from the design stage. Another reason for the effectiveness of this method is its flexibility to achieve improved accuracy considering the error caused due to the machine tool, process and environmental conditions. It enables to achieve greater inroads in the manufacturing of more accurate machine tools as well as the production of

high precision components using even a moderately accurate machine tool. Eventually the lead-time for building such machines is drastically reduced. So error compensation could therefore be considered the primary method of error elimination. Error compensation technique could be further divided into two categories depending on the extent of the repeatability of the system: the inferring of machine tool errors through the inspection and manufacturing data analysis of components produced by a number of operations conducted on the machine tool and the condition monitoring of machine tools by using sensory data. The former is called Pre-calibrated or feed-forward strategy and later is called Active real-time or feed-back strategy.

1.5.2.1 Pre-calibrated or 'feed-forward' error compensation

In the pre-calibrated method, the error is measured either before or after a machining process and the data is used to alter or calibrate the process during subsequent operation. The main assumption in this method is that the entire process of machining and measurement is highly repeatable. So this compensation method is most effective in compensation of repeatable systematic errors of the machine tool. Figure 1-5 shows the Pre-calibrated error compensation scheme. Compensation data is computed by scanning the machined sample components and/or by error measurement using high resolution sensors such as laser interferometer, capacitance sensor etc. The error data is either stored in the controllers' memory (correction table) or compensated during the tool-path generation process (software compensation). Hence, a pre-computed move is made by the machine tool which overcomes the systematic error of the machine effectively. It would indeed be futile to incorporate the pre-compensation technique on machine tool whose precision

is defined by the real-time and random errors. Since the error measurement and compensation are therefore carried out at significantly different times (non-real-time error compensation) the effectiveness of this compensation technique is uncertain due to the real-time disturbances in the machine tool and as mentioned in section 1.2, the accuracy of the machine is defined by the magnitude of the random errors.

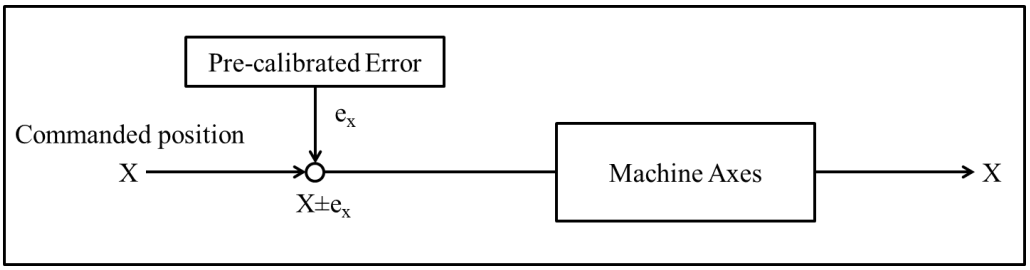

Figure 1-5: Pre-calibrated error compensation scheme

1.5.2.2 Real-time Active or 'feed-back strategy' error compensation

Real-time active error compensation is a closed-loop technique with the advantage of compensating both systematic and random errors[6]. In this method, the system monitors the condition of the machine continuously and any error that may be generated is compensated accordingly.

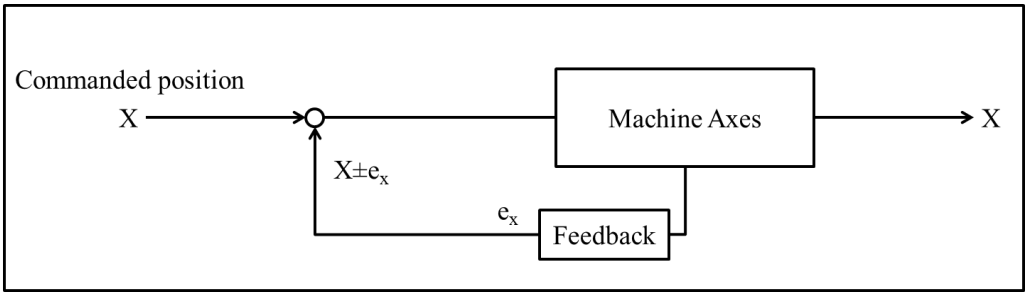

Figure 1-6: Real-time active error compensation scheme

The advantage of this process is that a higher grade of workpiece accuracy can be achieved on a relatively inaccurate machine tool through the use of real-time error compensation techniques. This is desirable in the industry today as it involves a combination of advantages: high accuracy, low

cost and high production rate. This technique can overcome the traditional barriers on achievable accuracy of machine tools.

From the above mentioned information on machine tool improvement, the major focus of this research is to study the errors in the machine tool and develop a compensation technique to compensate the existing error using novel complaint based mechanism. By focusing on machine tools' accuracy, the cost of the machine and hence the machined precision components can be reduced significantly.

1.6 Thesis Organization

The following list highlights the specific contributions of this thesis.

1) In chapter 2, a review of state-of-art real-time error compensation approaches and their effect in surface integrity improvement particularly in Diamond turning machine (DTM) is presented. Role of compliant mechanisms (Flexure based mechanism) such as Fast tool servo in such real-time active compensation is discussed in detail.
2) In chapter 3, flexure hinge parameters are studied with the development of a compliant monolithic microgripper mechanism. Effects of various flexure hinge parameters and their orientation in the design is compared between the FEM simulations and experiments. An analytical model for the microgripper is also developed. Conclusions are drawn based on the results and are implemented in further designs.
3) Chapter 4 presents an overview of ultra-precision lathe and the machines' performance characteristics. Geometric error such as the slide's positional accuracy, form and the kinematic error such as

following error of the axes are measured and the results are presented. Consequently, an attempt is made for an on-line compensation of the identified error by using the machines' servo system.

4) Chapter 5 presents a new *single axis flexure mechanism* design with the piezoelectric actuator and its performance characteristics. Followed by, the real-time compensation of the following error using the dual servo concept is verified (machines' servo and secondary flexure mechanisms' servo). The control system consists of two different position sensors - linear encoder and strain gauge sensor for machines' servo and flexure mechanisms' servo respectively. Both pre-compensation of the slide errors and active compensation of following error computed in real-time from the machines' servo are implemented. The proposed *single axis flexure mechanism* system is tested for its mechanical characteristics, waviness, and following error compensation performances using measurements and machining experiments.

5) Based on the results of chapter 5, in chapter 6, a *novel dual-axis parallel flexure guiding mechanism* is developed and tested. The new design comprising the piezoelectric actuator is verified for the cross-axis error as well as the actuator isolation based on the FEM simulation and experimental results. The proposed *novel dual-axis parallel flexure guiding mechanisms'* performance in active real-time error compensation of the two servo axes of the DTM is tested with contour machining experiment.

6) Chapter 7 provides the overall conclusion of this research and possible areas of effective implementation and extension of the current research are mentioned.

More rapid progress can be made by combining a readily available level of mechanical exactness with

** error compensation and*

** servo control,*

instead of striving for the ultimate in mechanical refinement.

G. R. Harrison 1973

Chapter 2 Literature Review

2.1 Chapter Overview

Various machine tool errors which deteriorate the surface integrity of the machined components have been discussed in the previous chapter. Real-time active error compensation provides a cost effective and reliable method to achieve high quality parts. For real-time error compensation, researchers have employed an additional auxiliary axis called the Fast tool Servo (FTS) which are predominantly used for nano/micro feature generation application. Since the features generated is of only few microns, the leverage for machine errors are limited to sub-nanometer scale. In this chapter a detailed review of the FTS and its components are discussed. Following this, application of FTS in machine tool enhancement is presented. Based on the discussions, few conclusions are drawn which leads to the motivation of this research.

2.2 Fast Tool Servo

A *fast tool servo* (FTS) is an auxiliary servo axis that is predominantly used in conjunction with diamond turning machine (DTM) to generate complex free-form textured surfaces with nanometer-scale resolution. As the name clearly emphasize, a FTS system provides a rapid displacement to tool-tip for every rotation of the workpiece. The complexity and the types of surfaces that can be machined depend greatly on the achievable acceleration, accuracy and bandwidth of FTS. Typically, the range of bandwidth varies from few hertz to tens of thousands hertz and amplitude from few microns to

millimeter range. FTS uses the benefits of single finishing operation of the DTM to generate micro-features with optical finish quality.

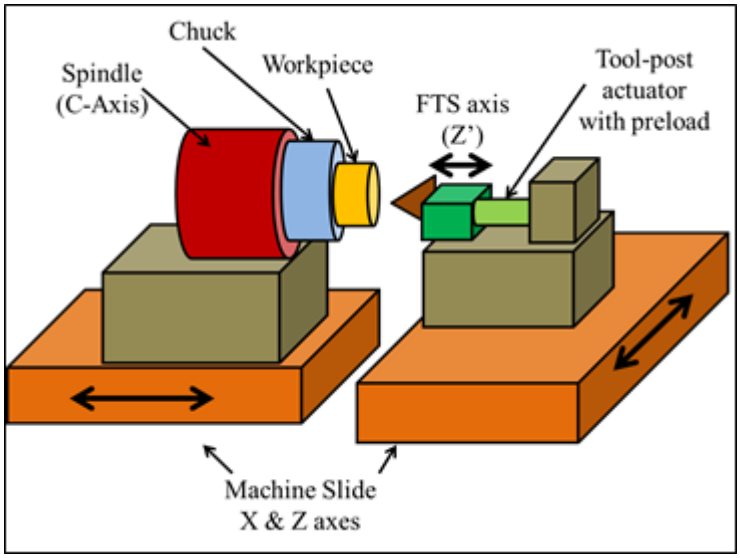

Figure 2-1: Schematic of a FTS system

The important factor which makes FTS stand out is its low mass characteristics, high bandwidth operation and extremely high positioning resolution. Due to its reduced mass inertia, it compliments generation of higher bandwidth features such as complex free-form surfaces with diamond tool to produce optical surface finishes. FTS provides the capability to rapidly machine rotational non-axis symmetric surfaces such as cam, toric, off-axis segment of a parabolic mirror, micro structures with sinusoidal grids, Micro-lens array (MLA), Micro pyramid array (MPA) *etc*., with sub-nanometer surface finish. Figure 2-1 shows a schematic of the FTS system mounted in a DTM.

The machine axes represent the slow tool servo (STS) which are conventionally used in machining both rotationally and non-rotationally symmetric continuous surfaces with low frequency and high amplitude. The tool path is generated by synchronizing the two machine slide axes with the

spindle axes (C-axis). This process is effectively used in machining continuous surfaces with a no inflection or steep surface slopes. But all the above mentioned micro structures, which have sudden change in their surface profile, cannot be realized using the STS system. Thus the need of FTS comes into existence due to afore mentioned performance characteristics. The FTS axis (Z') as mentioned in Figure 2-1, acts an individual servo axis which in conjunction with the machine axes and spindle axis (C-axis) facilitates realizing discontinuous micro structures with high surface quality.

FTS have seen a wide scope of application in the ultra-precision manufacturing regime. FTSs development has benefited a spectrum of fields such as optics, photonics, opto-mechanics-electronics, telecommunications, biomedical product, semiconductor, *etc*. [7] as micro-structured surfaces exhibiting excellent functionalities compared to a smooth surface. Micro pyramid structures of different heights acts as a micro-fin significantly improve cooling performance of a super-heated wall [8]. These micro-fins and micro-channels pose a greater potential to improve the efficiencies of semiconductors and microprocessors with their effective heat-exchange capabilities. Sinusoidal grids of micrometer wavelength are used as surface encoders for detecting multi-degree-of-freedom (MDOF) translational and tilt motions of precision stages [9]. Micro-structured surfaces created on the tool face lead to high cutting performance [10, 11]. Micro porosity and morphology patterned on crystalline silicon solar cells can reduce surface reflectance and improve the cells' efficiency [12]. Micro-lens array has been used in fiber coupling and optical switching, collimation of lasers diodes, imaging systems and sensors, beam homogenizers for lasers and illumination

systems, array optics featuring high precision, aspherical lenses for creating the best imaging characteristics, *etc*. [13].

So the need for an FTS system which actively changes the distance of the tool from the workpiece along z-axis of the lathe has increased many folds. Numerous research groups have dedicated their efforts towards research and development of FTS system, the most common application of FTS is in the direct fabrication of lenses, lens molds for bio-medical applications which correct astigmatism and in the field of optics where feature arrays such as MLA, MLP.

Some of the works on FTS were dated back as early as 1980's, *Meinel et al.*[14] has successfully produced phase corrector plates for wavefront correction and *Luttrell et al.*[15] was able to fabricate off-axis conic surfaces and tilted flats using the FTS. Some of the freeform optical surfaces manufactured by FTS diamond turning are illustrated in Figure 2-2.

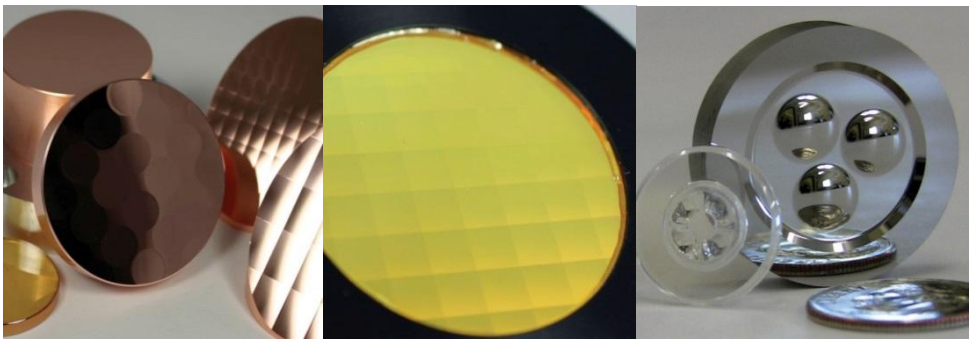

(a) Faceted mirrors (b) Faceted lenses (c) Aspheric lens array

Figure 2-2: Freeform optical surfaces by FTS process [16]

2.3 Components of FTS

The following are the main components of the FTS system: *Guiding mechanism, FTS actuator and corresponding control system depending on the type of actuator.*

2.3.1 Guiding mechanism

Mechanical guide plays an important role in the FTS system since it provides the necessary recti-linear path to the FTS. Most of the FTSs are placed normal to the workpiece either radially or axially. The important characteristic of the guiding mechanism is to provide the normal displacement with any parasitic erroneous motion to the tool at a hundreds of hertz higher than the machine axis. They provide the necessary preloading to the actuator in order to prevent any motion loss and backlash during their high frequency actuation. Also pre-loading helps in preventing the actuator damage due to impact loading during machining.

2.3.1.1 Flexures

Flexures are compliant elements which exist in engineering field long since 1950's. Jones [17], in 1950 designed an instrument which provides a parallel motion to itself. He used thin sheet (0.3 to 0.6 mm) of beryllium-copper and spring steel and tried various design patterns of simple and compound spring arrangement to achieve perfect parallel motion. In 1955, the same research group studied the parasitic error embodied in their design and came out with the possible causes for the same. This was the starting point for usage of flexures (though the name flexures were not coined at that time) in development of precision mechanisms. They are used to connect rigid bodies

and provide a relatively low level of rotation between the rigid links. The flexure hinges are analogous to a rigid pin joint with limitation of limited rotation angle (Figure 2-3).

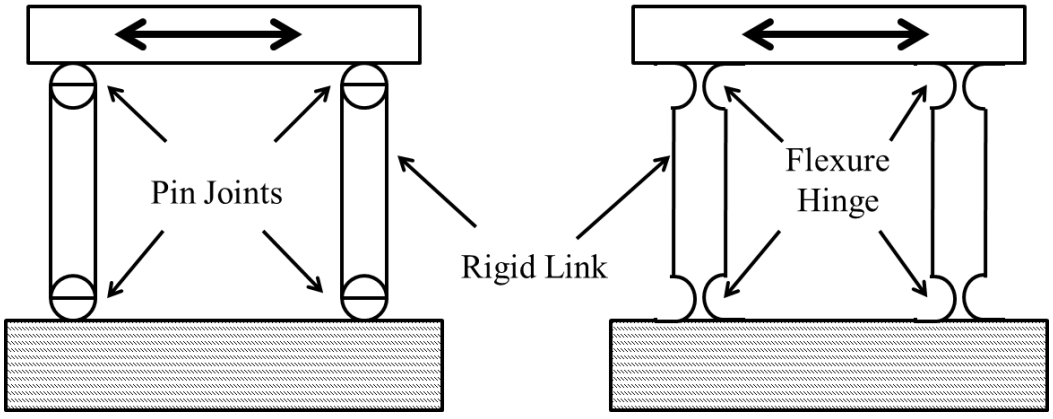

Figure 2-3: Conventional pin-joint and its flexure hinge counterpart

Flexures obtain all or most of its motion by elastic deformation about its slender cross-section and store energy in the form of strain energy. Once the input force is removed, the energy is released to bring back the mechanism to its initial position. They are the most commonly used element in the design of precision components such as nano-positioners and microgrippers for hi-tech applications including scanning probe microscopy, lithography, nano-metrology, beam steering for optical communication systems, fabrication and assembly of nanostructures, handling and manipulation of micro objects, microassembling, machining, and in manipulation of flexible and fragile biological micro-objects such as cells and bacteria in bio-technology [18-20]. Flexure based mechanisms are the most commonly used as a mechanical guiding mechanism in a FTS system. Flexure has various advantages which are discussed in detail in most of the literature [21-23]. The main reasons due to which flexure hinges are used in FTS as guiding mechanism are:

- friction-free motion and theoretically no wear
- reduced part count making the manufacturing process simpler and avoidance of assembly prone errors
- reduced cost but increased precision and reliability
- no hysteresis in the system for lower load and displacement as in micro/nano machining
- achieve higher off-axis stiffness to withstand tangential cutting forces

Though the flexure based mechanisms are delimited by their output displacement, they are extensively incorporated in applications such as FTSs, due to their high quality motion attributes which are otherwise impossible or difficult to achieve using conventional rigid-body mechanisms [21].

Flexure based design has been traditionally evolved on creative thinking and engineering intuitions which is considered a designer's delight [24]. In the design of guiding mechanism, systematic and symmetric arrangement of the flexure hinges provide constrained motion without any parasitic motion errors. Also symmetric arrangement of flexure hinges helps in avoidance of thermal expansion of the mechanism, thus maintaining the axis-normal assembly and actuation of the FTS system. Mathematical approach such as the elliptical integrals has been used to analyze end-loaded large deflection cantilever beams in order to obtain closed-form solutions [21]. However, this mathematical approach is difficult to use and provides only little insight about the motion or stiffness of the beam. Alternatively, a parametric approximation model called the Pseudo-Rigid-Body Model (PRBM) introduced by *Howell et al.* [25] becomes a bridge between classical rigid-body mechanism theory and compliant mechanism analysis. It acts as a visualization tool for designers to

analyze the deflection of flexure mechanisms which is more simplified and accurate. The abundant literature and the ease of design and manufacturing, makes the flexure hinges an inevitable choice for FTS system.

2.3.1.2 Classification of Flexures

A classification chart of flexures is presented in Figure 2-4 based on its compliance. Flexures are classified according to their *compliance type* and *compliance axis*. The type of compliance mainly depends on the geometry of the flexures. The two main category of compliance are *Lumped* and *Distributed* types (Figure 2-5(a) & (b)). As the name suggests, lumped and distributed compliance flexures refers to the concentrated and distributed compliance along the flexure geometry. In lumped compliance flexures, two ends of the flexure element are used to connect two rigid-bodies. The location of the axis of rotation of the flexure tends to be confined to the small thickness zone for a lumped type and varied for distributed type. The notch type flexures are the basic element of lumped type flexures. They are simple in geometry and can be easily manufactured by CNC drilling, wire-EDM and water-jet cutting technologies. For example, circular notch type hinges are manufactured by drilling two holes adjacent to each other, leaving a small area of material in-between. The minimum cross section region acts as an axis of rotation and this axis is called as *compliant* or *sensitive axis*.

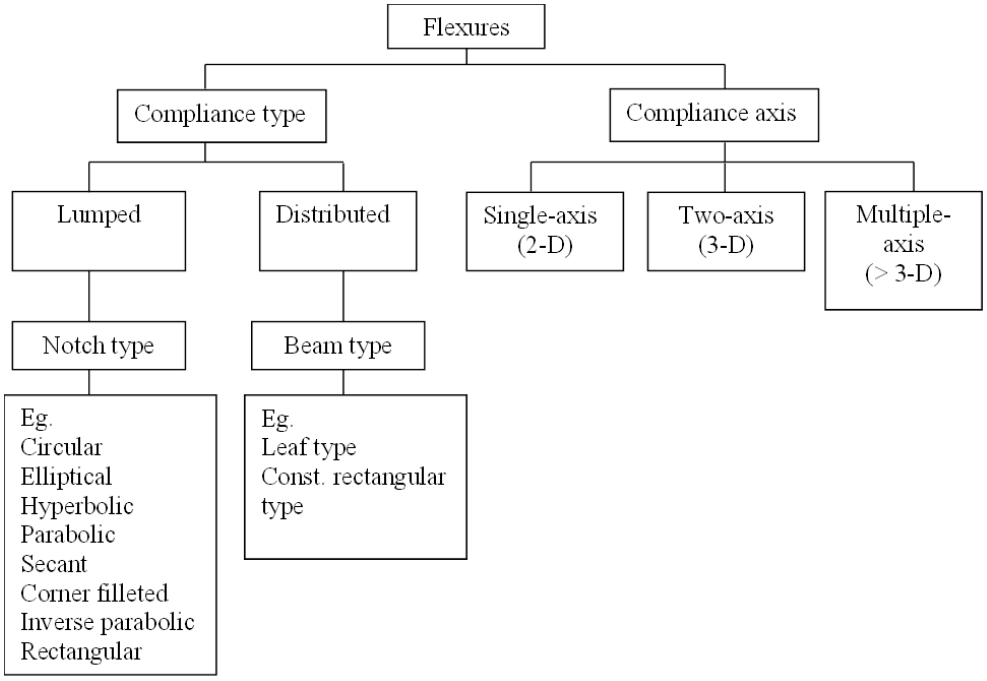

Figure 2-4: Classification chart of flexures

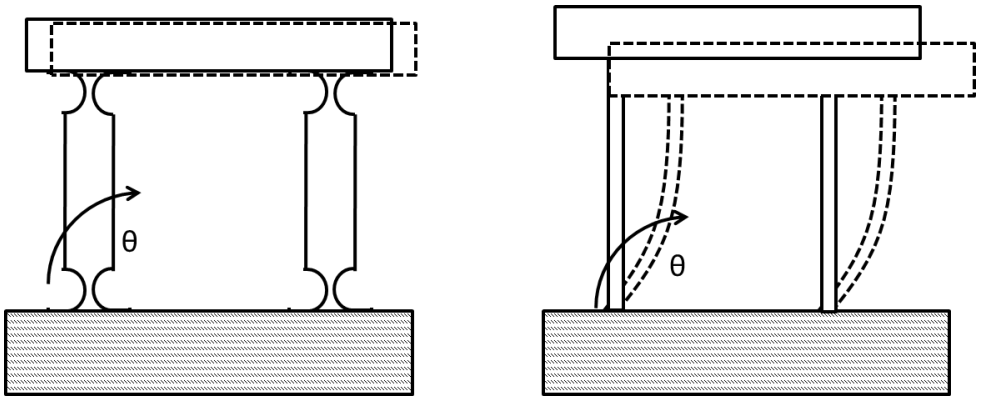

(a) Lumped compliance (b) Distributed compliance

Figure 2-5: Types of compliance

In 1965, Paros and Weisbord [26] came up with the first approximate compliance equations for circular flexure hinges (Figure 2-6) which are still used to this day. They formulated design equations, including both the full and simplified; to calculate compliances of flexure hinges. Equation 2-1 shows the bending stiffness of right circular flexure hinges. Many modifications have been done to this approximate equation to compute the near exact compliance value and various new types of flexure hinges are studies in late nineties by Smith [23] and Lobontiu [22]. One such variation of circular hinges is the

constant rectangular notch flexures which falls under the distributed compliance type flexures. They are more prone to off-axis error and the sensitive axis is distributed along its web length leading to non-linear performance. Figure 2-5(b) shows a distributed compliance type beam flexure. They are traditionally manufactured by clamping a thin strip (the leaf) at its end or by machining out a thin sheet from a single piece of material where the thickness permits this [23].

$$K_B = \frac{2Ebt^{\frac{5}{2}}}{9\pi r^{\frac{1}{2}}} \tag{2-1}$$

where, K_B is the bending stiffness of circular flexure hinge

E is the Young's Modulus of the material

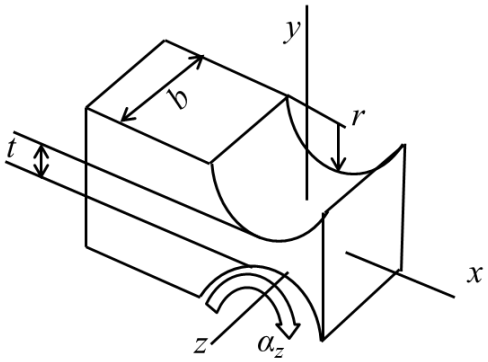

Figure 2-6: Right circular flexure hinge

The next major classification of flexures is based on the number of compliance axis. The sensitive axis defines the axis about which the flexure can provide the compliance and thus defines the flexure mechanism's DOF. The Figure 2-7 shows the different types of flexures based on its compliance axis. Single axis flexures are used on applications which are 2-D/Planar mechanisms. Two axis flexures are used in 3-D applications and multiple axis

flexures are used in Stewart platform which is now called as hexapod where each legs of the platform made up of flexures which can flex in all the 6 DOF.

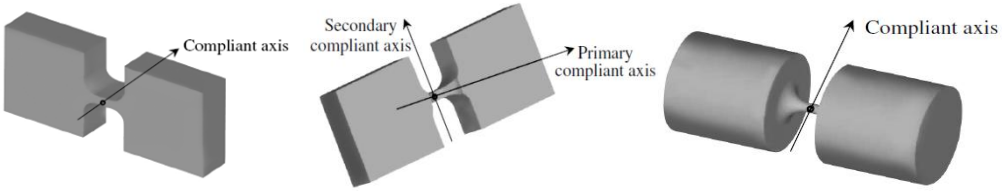

(a) Single-axis (b) Two-axis (c) Multiple-axis

Figure 2-7: Types of flexures based on compliance axis [22]

2.3.1.3 Flexure modules

Flexure modules are the basic building block of a flexure based mechanism design. A single module or more modules are systematically and symmetrically arranged in order to achieve a particular motion. The following are the basic flexure modules commonly used in the decreasing order of parasitic error (*e*):

a) Single module

b) Parallelogram module

c) Double/Compound parallelogram module

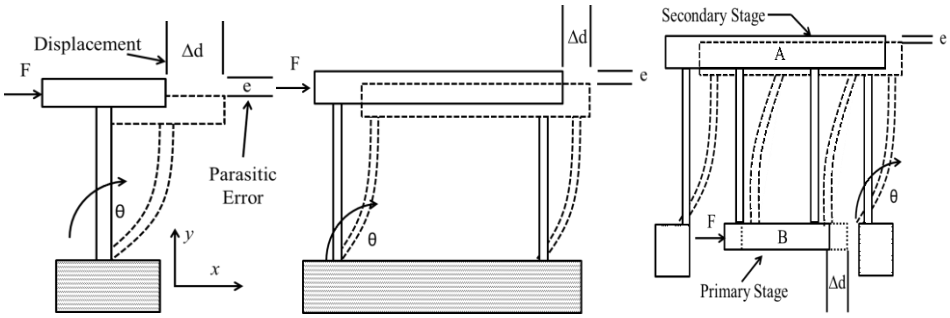

(a) Single Module (b) Parallelogram module (c) Double Parallelogram module

Figure 2-8: Flexure modules

2.3.1.3.1 Single Module

Figure 2-8 (a) shows a simplest flexure module called the single module to provide single axis motion. It is analogous to a cantilever beam where the deflection of the free end provides the necessary displacement. But it is seldom used because an arcuate locus is traced out by any point on the beam [23]. The flexure module provides 2 DOF, one along the axial direction *x* and a rotation θ along *z* axis. But there is also motion along the degree of constraint, *e i.e.* transverse motion along the *y* direction which leads to parasitic error in the system. So this flexure module can be used in application where accuracy can be compromised for the space.

2.3.1.3.2 Parallelogram module

The Parallelogram module as shown in Figure 2-8(b) uses two or more single modules to increase the rotational stiffness of the system. The rotation θ along *z* axis is reduced because the center of rotation of the system is shared between the single flexure modules. Thus the compliance for rotation is reduced. There is also a tradeoff in the axial motion along the *x* direction due to this cumulative stiffness. The other advantage of this module is that it provides more area for mounting the table or instrumentation [23]. Even though the stiffness along the rotational axis and axial *x* direction is improved, the parasitic error *e* along the transverse *y* direction is still accountable. So this module could be used in applications where a large displacement range is necessary.

2.3.1.3.3 Double/Compound parallelogram module

The double parallelogram module as shown in Figure 2-8(c) is made up of two parallelogram modules connected in series. The force F is applied to the inner

parallelogram B is converted to axial displacement along the *x* direction. The transverse displacement *e* along *y* and rotation θ along the *z* axis is transferred to the outer stage A. Thus the inner stage B which is used to mount the instrumentation is provided with a parasitic error free motion. The outer parallelogram acts as a secondary stage A which takes up all the parasitic motion which are present in parallelogram module. This phenomenon occurs due to equal and opposite flexing of the inner and outer stages B and A. Similarly the increase in the length of the inner stage B, will directly increase the length of the outer stage A, thus again compensating each other's deflection. Since the flexures are connected in series, equivalent to addition of their compliance, these modules have stiffness half that of the simple flexures from which they are made up of [23]. The motion range achieved by this flexure module is lesser compared to the other simple modules because of the added stiffness of the mechanism.

2.3.1.4 Flexure based mechanisms

The previous section discussed about flexures and various flexure modules which are used to as building blocks to design a mechanism. Beam based leaf type flexures were used in order explain the modules due to their simplistic design. These building blocks can be even designed using lumped compliance type hinges such as circular, elliptical *etc*. Most of the application where load will be acting on the stage should be designed using lumped type hinges since the beam region connecting two hinges will act as rigid body and help in load bearing. In applications like metrology and scanning where no or only minimal load is expected to act on the stage and comparatively a large range of displacement is required, distributed compliance type mechanism is useful.

The biggest advantage of flexure based mechanisms is the flexibility to design the mechanism either in series (analogous to conventional stacked rigid body design) or in parallel (monolithic, which is otherwise not feasible with rigid body counterpart). But there are few tradeoffs between the flexure based series and parallel mechanisms. Even though the flexure based series mechanism retain the advantages and overcome the disadvantages of conventional series design mechanisms, they are prone to inertial errors due to masses like weight of the stage, moving actuators and control elements acting on the base stage and detrimental in the mechanism's dynamic response similar to conventional rigid-body counterpart. On the other hand, flexure based parallel mechanisms are not affected by the above mentioned errors, but are prone to cross-axis coupling and limited travel range.

Further discussion is focused towards the flexure based planar mechanisms. The major classification of the planar mechanisms is serial, parallel and hybrid mechanisms. As described in the previous chapters the main objective of the mechanism is to provide the motion in the necessary direction and restraint in rest of the direction. The former is considered to the DOF and later as DOC. In a serial mechanism, all links (at least one being a flexure hinge) are connected serially in such a manner that the resulting configuration is an open chain consisting of at least one input port (where the incoming energy is fed into the system) and one output port (where the resulting motion is delivered outside the system). The input and output ports (or platforms) are generally rigid links that can be located anywhere within the serial mechanism. A parallel mechanism is formed of two or more flexure hinges that are connected in parallel to a rigid link, which plays the role of

output port/platform [22]. Thus both serial and parallel deign provide the necessary motion and restraints. The basic and important difference between the serial and parallel design is that in serial design the motion is achieved by either stacking up of single DOF stages one over the other (out-of-plane) or having a nested design where the stage is designed to be monolithic but each axis is independent of the other's motion (in-plane). The stacked serial design is analogous to any machine tool because each level of the design provides a single DOF and similar design is stacked on the base stage to provide one more DOF. Thus to achieve X-Y motion as in a milling table, a serial stack of two axes are required. In a nested design, X-Y motion can be achieved by monolithic design stage where the outer stage provides one DOF and the inner provides the other DOF. Thus an easier design with independent, comparatively larger displacement range is achieved using a serial design. But there are few disadvantages in the design; each stack work independently and without the knowledge of the other stack's position. The mass of one stage acts on the base stage which reduces the dynamic response and the control of the system difficult. Also the mass moment of inertia of the top stage creates non-symmetrical instability in the system. In the nested serial type design though the weight of one stage does not act on the other stage, the outer stage needs to displace the inner stage along with the actuators which again creates instability and each stage works without each other's position which makes the feed-back control of the each stage difficult.

On the other hand, parallel design is designed monolithically such that each axis has the information of the other axis's position. Parallel design overcomes all the drawbacks of both rigid body mechanisms and serial type

flexure mechanisms. Each DOF works hand-in-hand such that dynamic control of the stage is easier as each DOF has the information of the other DOF. The out-of-plane parasitic and rotational error is minimized and they can be controlled dynamically using additional sensors or by systematically and symmetrically placing the flexure modules [27]. In parallel mechanisms too there are few drawbacks such as the limited motion range compared to the serial design and rotation of the stage due to cross-axis coupling [27]. The force/displacement of one axis affects the stiffness characteristics of the other axis which makes the control algorithm complicated and force-displacement characteristics non-linear. In order to avoid such complications the motion range is limited such that each DOF's motion doesn't create any deterioration to the other DOF.

In a hybrid mechanism, several legs in the form of serial open chains (actually serial mechanisms, according to their recently introduced definition) are placed in a parallel fashion, and they all connect to a rigid link (the output platform) [22].

2.3.2 FTS Actuators

FTS are broadly classified based on their actuation type, achievable range of motion and frequency response and topology. Researchers have developed FTS with a wide range of actuators based on the requirements of a particular application. The following are the main categories of FTS actuators:

- *Piezoelectric*
- *Lorentz force*
- *Magnetostrictive*

- *Shear-stress electromagnetic*
- *Normal-stress electromagnetic*
- *Hydraulic*

2.3.2.1 Piezoelectric FTS

Piezoelectric based FTS are short-stroke FTSs which is similar to micro-positioning devices [28]. The advantage of piezoelectric materials is its high dynamic stiffness (greater than 50 N/μm), force generation and bandwidth in the order of kHz with nanometric positioning accuracy and compact size. However, piezoelectric FTSs exhibit the following demerits due to the piezoelectric ceramic's properties:

- Energy losses and heat generation in the material when undergoing deformation with applied voltage affects the tracking performance due to the nonlinear behavior and hysteresis. So need for liquid cooling of the piezoelectric ceramic becomes a mandate.
- The effective stroke reduces significantly during high frequency and acceleration operation.
- Care is needed while designing piezoelectric FTSs to provide proper pre-load and motion guidance in order to avoid tangential loads and compressive stresses, failing which could lead to cracking of the actuator ceramic.
- Advantage of achievable bandwidth of the standalone piezoelectric actuator is reduced to that of the lesser resonant frequency of the guiding structure depending on the movable mass of the FTS.

The above mentioned demerits can be eliminated with much ease with the availability of a range of commercially available piezoelectric actuators.

These piezoelectric actuators are pre-loaded and enveloped in water/dust proof casing. The availability of the high power amplifier and servo-controllers based on in-built strain gauge sensor provides a better closed loop performance with the applied voltage. Continuous development in the field piezoelectric ceramic and electronics eliminates the need for liquid cooling during high frequency actuation by proper selection of piezoelectric ceramic and the complimentary electronic circuitry. Proper care in design of the guiding mechanism, mostly based on flexure hinges, prevents the piezoelectric actuator from parasitic tangential forces and helps in improving the resonant frequency of the system along the direction of motion.

Though various actuators are in use, nevertheless, piezoelectric actuated FTSs have seen significant research contributions and are widely used. In summary, piezoelectric actuators have significant applicability in FTS for microstructure machining and machine tool error compensation in order to improve the accuracy. The discussion is limited to PZT actuator and further review of other actuators and their control methodologies are available in the literature [29-66].

2.3.3 Classification of FTS

Since a significant amount of research effort has been devoted to FTS design over 30 years, a general classification of the FTS is presented. FTS can be classified in to two major categories: *Application and Topology* as shown in Figure 2-9. Since the need for sub-nanometric surfaces are in demand, many researchers have developed error reduction system in order to provide a sub-nanometer surface accuracy to the components in which micro-features are produced. Due to the larger range of frequency response difference between

the machine slides and FTS, the latter effectively compensates the geometric error in both offline and real-time methodologies. This proves to be a cost effective way to machine precise components using any low precision conventional machine tools.

Hence, the FTS are applied in the following two error reduction mechanisms: *Tool-positioning* and *Error compensation mechanisms*. *Tool-positioning* deals with synchronized tool movement by utilizing the benefits of lesser moving mass and higher resolution and bandwidth FTS systems. They eliminate the machine tools' form error being copied from the axes to the machined components especially during the generation micro-structures which demands sub-nanometric surface integrity. Some researchers have incorporated a pre-compensated tool-path to the tool-positioning system to overcome the form error of the machine axes. *Machine tool error compensation*, utilizes the advantages of FTS to overcome the surface normal errors of the conventional slower machine slides. By error compensation mechanism using FTS, the machine tool accuracy can be enhanced to many folds since it can compensate both *static* and *dynamic errors* in real-time. Another important classification of FTS is based on the axis of FTS movement into Linear and Rotary FTS. Linear FTS follows the same Cartesian coordinate as that of the machine axes while the rotary FTS follows a polar coordinate and are generally have their rotation axis aligned to that of machine tool's rotary B-axis. In this second classification, the stroke length of FTS is mainly focused and further discussed on the topology based classification is ignored since it deviates from the research objective.

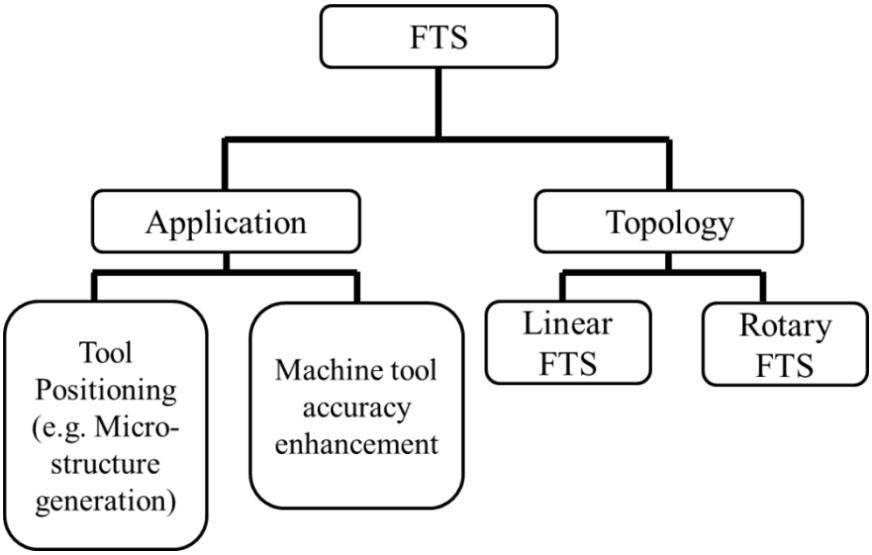

Figure 2-9: Classification of FTS

The following contributions from the literature have brought some light on the design consideration and application of FTSs in machine tool accuracy enhancement:

2.3.3.1 Tool positioning system

As mentioned above, Tool positioning system implies the incorporation of the FTS system to actuate the tool to the required position with utmost accuracy. This eliminates the need for sophisticated machine tool/components. An overview of the principles of precision design of micro-positioning systems was presented by *Schellekens et al.*[2].

Patterson and Magrab[67] designed a piezo based FTS for diamond turning at Lawrence Livermore National Laboratory. The main design consideration is to develop a tool positioning system high static and dynamic performance at frequencies beyond the bandwidth of the machine axes. FTS with a stack type PZT (6.3 mm diameter (approx.) and 12.7 mm length) provided ±1.27μm stroke at 100Hz bandwidth and dynamic repeatability of 1.3 nm. The stiffness was chosen to be sufficient to place the resonance above

1 kHz when supporting the maximum weight of the movable tool holder assembly is limited to 380 g. The two parallel and symmetric diaphragm (leaf) flexures fixed to a cylindrical support provided the rectilinear motion and greater reduction in mass of the moving unit. An integrated capacitance sensor provides position feedback with a closed-loop position bandwidth of 640 Hz. However, the existing large axes on LODTM are so accurate that the piezo servo was not used in its operation.

Another group of researchers from Precision Engineering Center at North Carolina State University has also been active in the area of asymmetric turning and FTS design since 1987. Falter *et al.* [68] have developed a FTS of 20 μm stroke and 2 kHz bandwidth (Figure 2-10). The heart of the servo was a hollow piezoelectric actuator (25 mm OD and 18 mm long) with resonance frequency of approximately 10 kHz. But at 1 kHz, the FTS has a maximum stroke was limited to 5 μm and heat generation in piezoelectric actuators interrupted continuous operation of the FTS. The developed FTS has been applied in several investigations such as compensation of inherent vibration during machining [69].

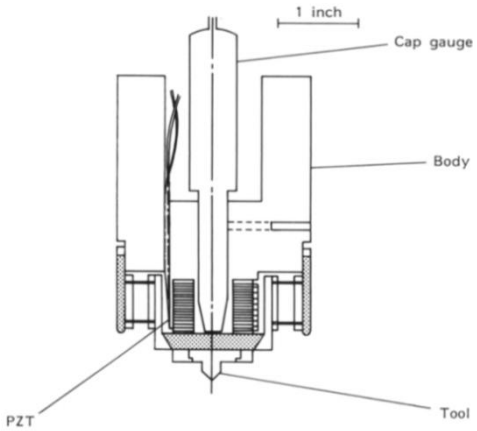

Figure 2-10: Designed FTS [69]

From the same group, Dow *et al*. [70] designed the piezoelectric FTS for machining of non-symmetrical surfaces. FTS has a maximum range of 10 μm and a usable bandwidth of nearly 2 kHz was achieved at a reduced effective operational stroke length. This device was attached to the tool arm of their Parallel Axis Ultra-precision Lathe (PAUL). The Doctoral thesis of Falter [71] describes in detail the tool arm which is similar to a phonograph stylus replaced by a diamond tool.

Cuttino *et al.* [72] reported a novel FTS by employing a long piezoelectric stack with 100 μm stroke and 100 Hz bandwidth. Generally, the long piezoelectric actuator has the severe hysteresis problem. This study has proposed that by adding a hysteresis module can successfully compensate the hysteresis by 43% for full-range travel and by 80% for a travel range of 70μm.

In 1990, Okazaki [73] proposed a piezo tool servo by employing a stacked ring piezoelectric actuator (25 mm OD, 14 mm ID and 19 mm long, 15 μm stroke). The piezoelectric actuator was fixed inside a steel block with N-shaped slit from its slide (Figure 2-11). The effective stroke of the FTS had reduced to 7 μm because of the stiffness of the flexure. *Hara et al.*[74] developed a micro-cutting device which consists of a parallel flexure based tool holder actuated using a pre-loaded piezoelectric actuator and a piezoelectric contact sensor for real-time measurement. The active stroke of the device is 3.7 μm with 80N/μm stiffness and is used in machining constant micrometer depth of cut groove. This study was mainly focused on the investigation of initial contact point and the capability to adjust depth of cut in real-time using the contact sensor output. The repeatability of the device is within ±1μm. No machining result was reported.

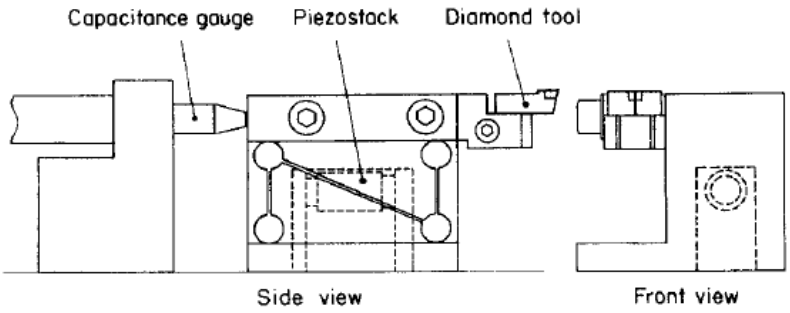

Figure 2-11: Schematic of FTS system with closed-loop feedback [73]

Rasmussen *et al.*[75, 76] developed a system for asymmetric turning which used a piezoelectric actuator to drive a tool through a lever assembly. A schematic drawing of this device is shown in Figure 2-12. The tool tip had a travel of 50 µm and a closed-loop position bandwidth of about 200 Hz. They turned steel and aluminum parts with rotational asymmetries of 21 µm at spindle speeds of up to 1200 RPM, with form errors of less than 5 µm. These larger form errors due to workpiece deflection could not be detected using strain gage attached to the piezoelectric actuator.

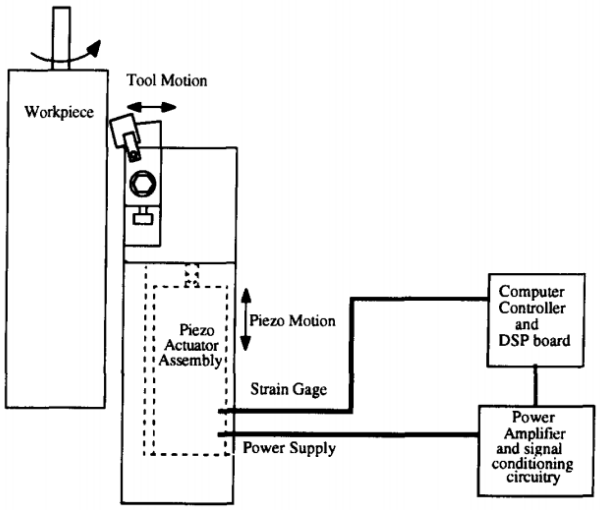

Figure 2-12: Schematic of FTS system for asymmetric turning [75]

Weck *et al.*[77] developed a hybrid long stroke fast tool servo, which integrated a finer piezoelectric system of 40 µm stroke at 1kHz bandwidth and a linear motor of 2 mm at 40 Hz. The piezoelectric translator had a maximum

force of 2400 N and peak thrust force of 900N with axial stiffness of 50 N/μm and a resonance frequency of around 2 kHz. The power loss of the linear motor and the piezoelectric translator was dissipated by a water-cooling system.

Kouno *et al.* [78] designed a piezoelectric actuated FTS system with 6.5 μm stroke length, 10 nm resolution at 70 Hz bandwidth and 300 N/μm stiffness. A linear variable differential transformer (LVDT) is integrated for close-loop position feedback. The device was proposed to be used in precision machine for nanometric precision tool actuation in order to overcome the inherent systematic errors of the machine tool. This reference gives an exceptionally well-written account of the design and testing of fast tool servo. However, neither error compensation techniques nor machining accuracy had been presented in these studies.

An active research group under Prof. Yusuf Altintas at University of British addressed the use of a piezoelectric FTS for precision shaft machining in conventional CNC turning machines. Zhu *et al.* [79] and Woronko *et al.* [80] employed an adaptive sliding-mode controller to compensate for cutting force based disturbances and hysteresis of the actuator.

Zhu *et al.* [79] performed both rough and semi-finish operations which were performed on a tool with a conventional CNC machine and the ultra-precision cutting were accomplished by the same machine using the developed FTS system (Figure 2-13). A significant improvement on the surface quality was obtained which could not be achieved with traditional CNC machine.

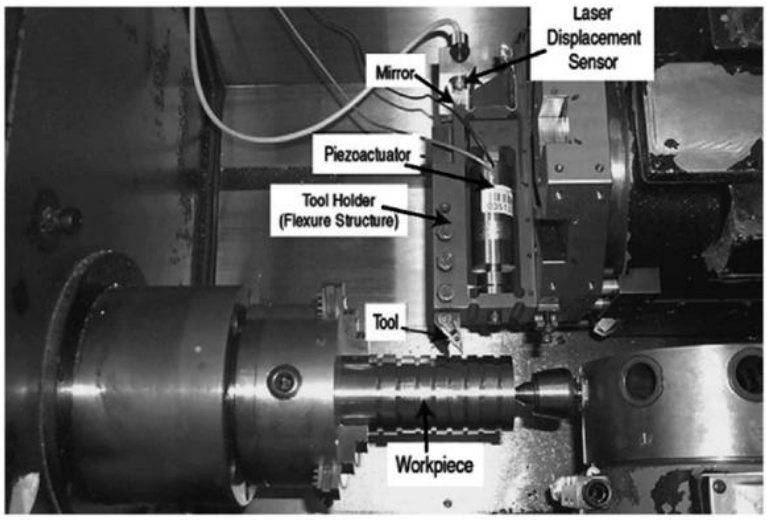

Figure 2-13: Piezo-based FTS attached to conventional CNC machine [79]

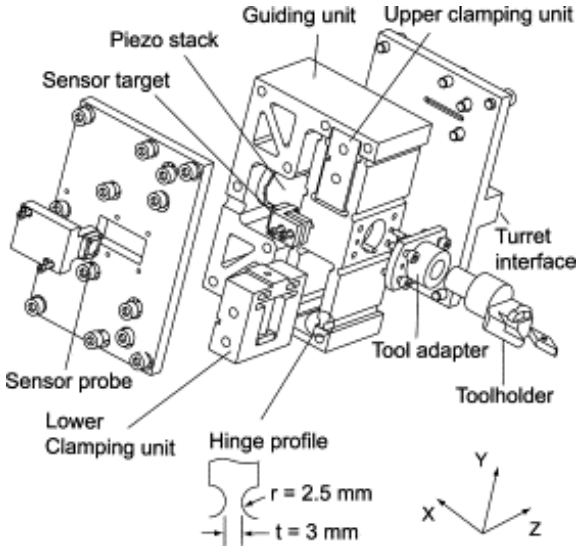

Figure 2-14: Schematic of improved FTS with clamping unit [80]

Woronko *et al.* [80] further improved the performance by developing a piezoelectric actuated FTS (Figure 2-14) with 38 micron stroke, 370 N/micron stiffness, 3200 Hz natural frequency, and 10 nm positioning during finish hard turning operation. The final finishing depth of cut is executed solely by the actuator within the actuator stroke with no change of the CNC radial position. Analytical and finite element models of the flexures are presented, and the design process is outlined. A sliding mode controller is implemented which provides 200 Hz bandwidth and 20 nm tool positioning resolution by rejecting cutting force disturbances (avg. radial cutting force of 6 N) and piezo-ceramic

nonlinearity during precision machining. Furthermore, in order to increase the stiffness FTS system to overcome the vibration during turning harder material, two piezo-actuated clamping units were incorporated in the design. Stepped, tapered, and convex micro profiles are machined to verify the control command is accurately reflected in the part form. The results demonstrate that the actuator is capable of precise and rapid tool positioning during shaft machining when mounted to a conventional machine tool. Maximum surface roughness of 2.0 μm was achieved in machining 4340 steel with 35–40 HRC hardness, and 0.85 μm for 4320 steel with 58–62 HRC hardness.

2.3.3.2 Error Compensation Mechanism - (Fine Tool Servo – FiTS)

The next major application of FTS is in the active compensation of the inherent machine tools' error using the advantages of the FTS system. During mid-1980s many researchers dedicated their effort in the improvement of the existing machine tools from the precision zone to the ultra-precision regime. Researcher from Hitachi Ltd., Japan had studied the effect of residual small vibration on the sophisticated ultra-precision DTM which inevitably deteriorates the surface roughness machined components. Takasu *et al.* [81] presented an analytical study and an experimental validation on the effect of small amplitude and low frequency vibration on the DTM. Based on these findings, Fawcett [82] developed a *Fast Low Amplitude Tool Servo* (FLATS) to compensate the inherent workpiece-tool surface normal vibration between the tool and the Z-axis in real-time. In situ measurement of the surface ahead of the tool, along the tool feed direction is measured using a capacitance sensor. Waviness was reduced significantly to achieve a P-V of 32nm and R_a of 3.8 nm. However, the system is prone to inherent noise due to the external

sensor and other quasi-static error, such as the axes straightness was not considered.

Similarly, Kim *et al.* [83] developed a micro cutting device with piezo-electric actuator (Figure 2-15) to control the tool to provide a precise depth of cut and simultaneously compensate the waviness on the surface of the workpiece. Eddy current type non-contact sensor with resolution of 0.5μm is used to measure the table waviness. The waviness profile of the machined Al workpiece is reduced from 1.3μm to 0.7μm. Description of the waviness measurement or real-time compensation was not mentioned in their paper. No insight about surface roughness studies or flexure mechanism modeling was presented.

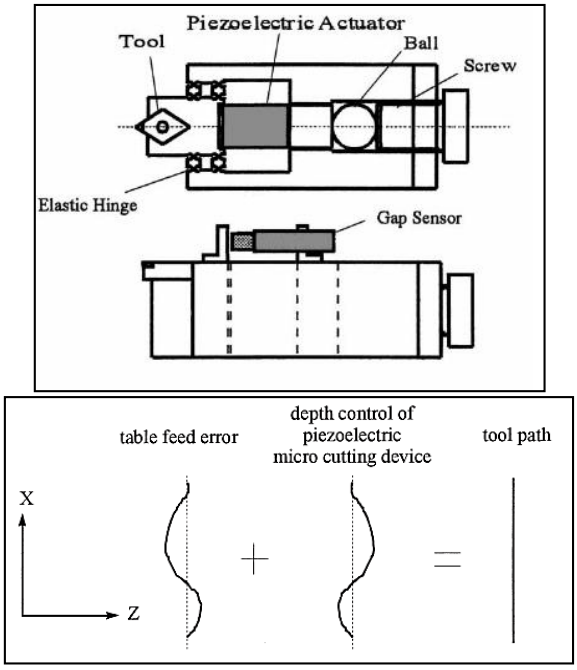

Figure 2-15: Developed micro-positioner and the error compensation mechanism [77]

In addition, they proposed the same concept by compensating the waviness that is found on the machined surface with the developed micro cutting device. The error was determined from the machined surface, and subsequently, set as

the compensation reference for the micro cutting device. Kim and Kim [84]developed a FTS with a piezoelectric actuator (45 mm length, 18 mm OD). Same mechanism design which was employing the parallel spring principle was reported. The results indicated that the FTS can successfully machine surface with 0.1 μm flatness after implementing feed forward and PID controller.

Horiuchi *et al.* [85] also used a piezoelectric-driven diamond tool to compensate for error motions in the work spindle and linear cross slide of a diamond turning machine. A pair of capacitance sensor was used as a feed-back unit to measure the error along the surface of a face-plate mounted on to the spindle. The characteristic of the developed device is not stated in this publication, but typical finish cuts on that particular machine are at a depth of 0.5 μm.

Kohno *et al.* [86] proposed an idea to improve the form accuracy by in-process measuring the relative movement between the tool and workpiece and compensating it with the FTS. Miller *et al.* [87] developed a piezo-actuated FTS and the necessary digital signal processor (DSP) based control interface to synchronize the slides servo and FTS servo. The slide servo forms the fundamental closed-loop for the axes error compensation and FTS servo for small perturbation Z axis motions synchronized to the rotation of the workpiece spindle (θ) and the radius (X) during machining non-rotationally symmetric surfaces. Straightness and the yaw error of X-slide are compensated using the Z-slide and vice-versa. X and Z slides straightness error is measured using laser interferometer and stored as a look-up table in the controller memory. A controller algorithm (Figure 2-16) is developed in

order to compute the next move of each slide based on the error table stored, thus actively compensating the slide error before the particular position is reached physically. A synchronized FTS and axes servo is incorporated while machining non-axis symmetric profile machining. FTS servo computes the current position of the axes from the laser interferometer feedback, spindle index and FTS's own position feedback from the high resolution capacitance sensor. This method of real-time error compensation is promising, but it is limited by the mechanical system's resolution and data transferring time between the two controllers. The slide error is compensated to 40nm in both X and Z axes and a PV value of 0.7μm while machining parabolic profile.

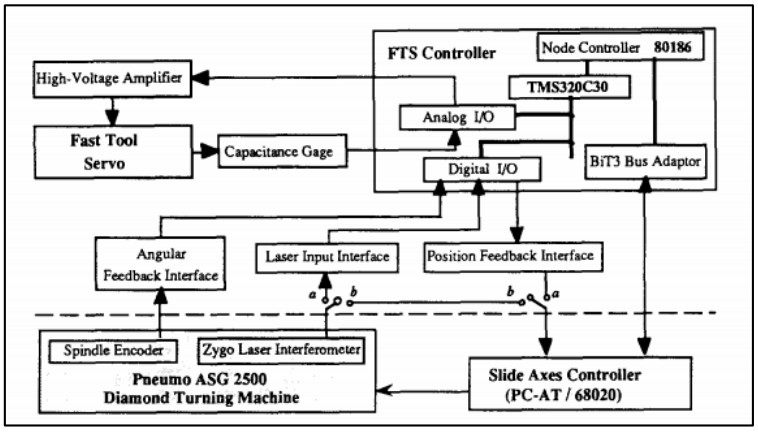

Figure 2-16: Integrated FTS controller configuration [87]

Pahk *et al.* [88] reported a real-time dual servo mechanism for positional accuracy improvement by employing a flexure based PZT actuated fine motion stage to improve the positioning accuracy of the coarser slide (global stage). A laser interferometer with 10 KHz transfer rate (maximum controller interrupt) is used to form a closed loop feedback system. The movement until 10 μm is achieved using the global stage and further movement is controlled by actuating the micro stage. Position accuracy of 10 nm is achieved with this dual servo mechanism due to the low inertia, higher

accuracy and response of the flexure based micro stage. Still the need to use bulk and expensive laser interferometer, this method will not be suitable for real-time machine tool error compensation at the cutting location. Also alignment of the optics will be of greater concern since it will lead to Abbé and Cosine error during measurement.

Howard K. McCue [89] proposed a dual servo mechanism for large optics diamond turning machine. The "slide" servos (X and Z axes) and Fast Tool Servo (FTS) provide the means to move the diamond tool. The '*following error*' which is one of the kinds of kinematic error is the deviation between the commanded and actual position of the axes. A real time following error compensation is implemented with a real-time computer (RTC) which commands the single axis FTS based on the difference in the commanded X and Z positions with that of the 13 feedback sensors output (7 laser interferometer position sensor and 5 differential capacitance sensor). Since a single axis FTS is used to compensate the two axes following error, the FTS is prone to provide a small erroneous motion (10^{-11} inches). Though the paper explains the parabolic part being machined, whether concave or convex surface is not described. The method mentioned is suitable for convex part machining but the erroneous motion due to FTS over travel will lead to undercut marks on the part surface during concave part machining. This paper provides a good insight on the need of a real-time compensation of the following error to improve the machine performance. Also the need for the dual axis FTS is indirectly implied due to inherent erroneous motion of the single axis FTS while machine contour surfaces.

Gao *et al.* [90] had presented a detailed study and compensation mechanism of the slide error of X-axis and the spindle errors along the axial Z-direction in a diamond turning machine. Though the design of the FTS was not mentioned in their work, they used a FTS unit with a bandwidth of 2.5 kHz and a stroke of 10 µm. The closed-loop schematic is shown Figure 2-17. The error along Z-axis at various X-slide locations was stored and a signal is sent to FTS for every pulse from the rotary encoder of the spindle. The error compensation signal to the FTS has three components i.e. the Z-directional out-of-straightness of the X-slide, angular and axial motion of the spindle. A PV value of 0.22µm is achieved with the compensation of the X-slide error along Z-axis alone. While the spindle axial and angular errors were compensated along with the X-slide waviness, a PV value of 0.12µm is achieved compared to the initial non-compensated surface PV of 0.27µm.

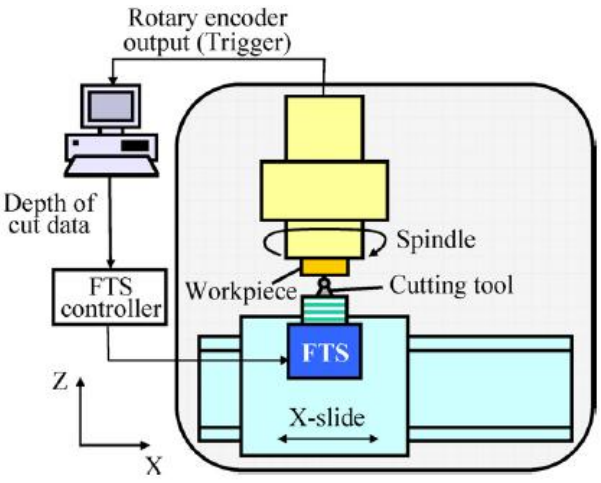

Figure 2-17: Schematic of the closed-loop control of FTS [90]

Xu *et al.* [91] had described their efforts to refine an existing cutting tool system for active error compensation with the aid of ultrasonic vibration cutting technique. They used two PEAs which were integrated in the cutting tool, one of which is for active error compensation and the other for ultrasonic

vibration cutting (Figure 2-18). The active compensation is achieved using two sets of differential capacitance sensors to measure the spindle run-out error in real-time, whose output actuates the compensator using their custom built stack type PEA. The profile (roundness) and the surface roughness were studied with and without compensation and ultrasonic vibration. The profile error is effectively compensated in their study with an improvement by 26.7% (12µm to 8.8µm) with no sign of surface roughness improvement. With both the error compensation and non-conventional ultrasonic vibrational cutting in place, the roundness profile is improved by 41.7% (to 7.0µm) and roughness is improved by 16.2% (1.36µm to 1.14µm). Though the active error compensation is employed in their study, both the profile and surface roughness values are in the micron range which is way away from the current industry needs. Also a detailed study on the existing machine tools' performance and slide-ways accuracy which plays a vital is not presented.

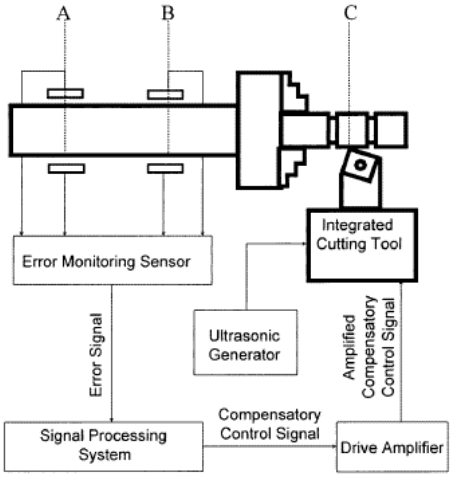

Figure 2-18: Schematic of experimental cutting system [91]

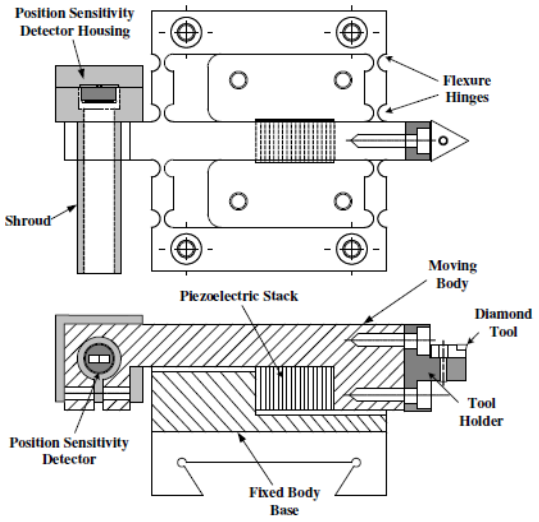

Figure 2-19: Schematic of the Flexure based FTS and sensor assembly [92]

Gan[92] developed a fine tool servo system for real-time error compensation in a miniature ultra-precision lathe. In this study, two piezoelectric actuated flexure based fine tool servo (FTS) systems had been developed. The objective of the work is to compensate for the X-axis slide error, due to which the profile accuracy of the machined components is affected. An external cost effective position sensitivity detector (PSD) of 0.1 µm resolution is used to measure the slide error in real-time and compensated using the developed closed-loop system comprising of piezo-actuated flexure based tool-post (Figure 2-19). The surface waviness is reduced from 277 nm to 31 nm for aluminum workpiece and from 123 nm to 64 nm for brass workpiece. The surface roughness value was 18 nm for both the workpiece material with and without the FTS implementation.

In the second design, a hybrid system was developed which had incorporated force and capacitance sensor to monitor the machining force and FTS displacement respectively, in real-time during machining (Figure 2-20). The surface roughness is found to be between 27 and 90 nm for various cutting conditions. At a particular cutting condition the surface roughness R_a is

found to be 164 nm and 35 nm without and with the compensation using AFM measurements. The surface waviness is found to be in the range of 0.12 µm to 0.2 µm for feed rate of 0.5-2.0 mm/rev at 500 and 1000 rpm respectively. But at higher feed rate around 5 mm/rev, the surface waviness is 0.1 µm for both 500 and 1000 rpm. This shows that the error compensation of the FTS is effective only at lower RPM and higher feed rates.

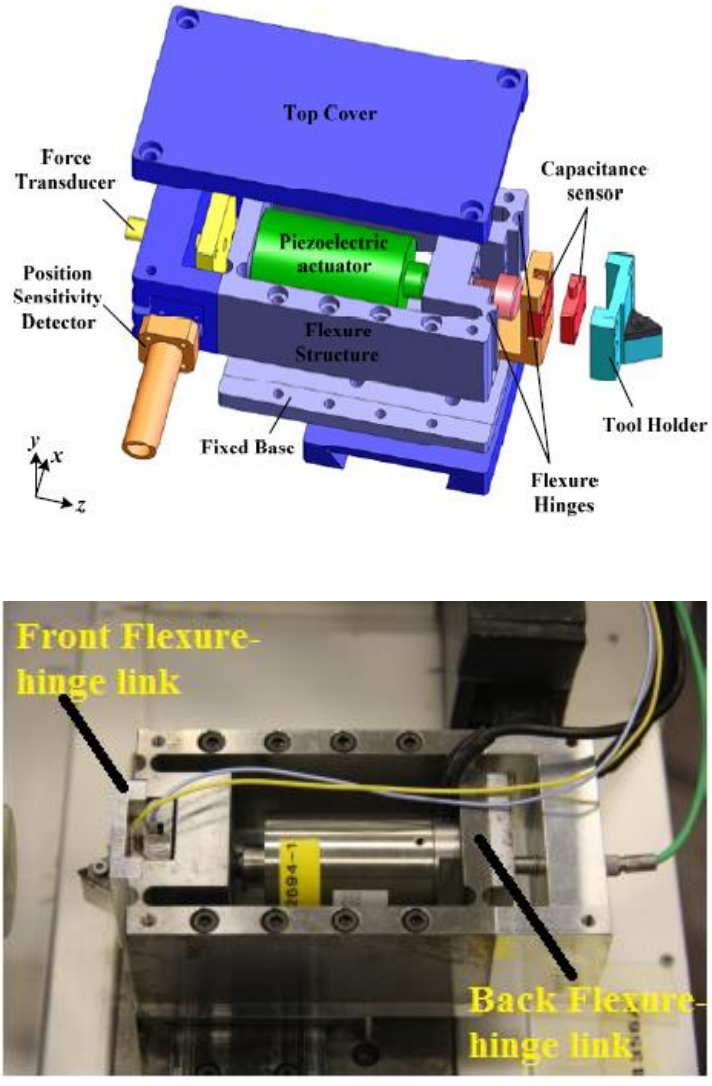

Figure 2-20: CAD and Photograph of the Hybrid FTS system [92]

2.4 Research Motivation

The performance enhancement of any conventional machine depends on various factors such as mass of the system, operational environment, maintenance, etc. All the above literature on compensation methods provides better accuracy to the machine tool and hence the improvement of surface integrity. The performance can be enhanced either by error avoidance or error compensation. Error avoidance deals with designing a machine in such a way that certain pre-estimated errors can be eliminated. But, by doing this, the machine is over designed. Moreover the lead time, maintenance cost, utilization of the resources increases. Error compensation is another methodology which eliminates the machine tool error by means of accurate error measurement, availability of high band-width controllers and sophisticated machine tool accessories such as linear encoders, guide ways etc., thereby enhancing the overall performance. The accuracy of such compensation technique depends on the resolution of the machine tool system (*combination of Mechanical, Control and Electrical units*).The resolution corresponds to the capability of the system and how closely it could perform to the given user commands. A closed-loop real-time feedback strategy is highly commendable in compensating both systematic and random errors, but they can never be more accurate than the resolution of the system because, there will be no further feedback to improve the accuracy. Also, the dynamic performance of the machine tool is limited by the mass of the axes, friction and stiction effects and importantly the cumulative effect of the error in each component on the machine tool assembly. Due to these factors, even after providing the high resolution feedback encoders, the final achievable machine

error is in manyfolds (50-100 times >encoder resolution) Clearly, a need for an auxiliary servo axis which is independent and devoid of inherent error provides an avenue to achieve surface accuracies better than the machine tools resolution. Hence a real-time compensation using Fine Tool Servo (FiTS) mechanism is to be used as suggested in literatures (Table 2-1). By using a FiTS mechanism the limitations due to mass, friction, stiction, etc. is reduced. Also the FiTS mechanism can be of monolithic design, the overall error due to components and their assembly is reduced. When a single servo is used to compensate the error in the system, it reaches saturation after a reaching the systems' resolution. Though real-time active compensation is effectively implemented in machine tool error compensation, few drawbacks of this method still exist. In real-time error compensation, the error is allowed to occur and compensated subsequently. Though the FiTS based auxiliary servo have higher dynamic response and resolution, the delay from the feed-back sensor to the FiTS is inevitable. So the effectiveness of the compensation is deteriorated. Also, the magnitude of following error depends on how tight the servo PID tuning of the axes is and the capability of the motor-amplifier. Since the servo control cannot work without a feed-back, to and fro vibration (kinematic following error) of the axes always exist at the desired position. This erroneous motion at the desired position replicates itself in the finished component as the surface normal error.

To overcome all the above mentioned shortfalls, a clear need for dual servo system which can compensate for the geometric and kinematic errors of the existing machine servo axes is profound.

2.5 Problem Statement

Hence, the overall aim of this research is to develop a two dimensional compliant mechanism for real-time active accuracy enhancement by implementing a dual servo principle. Thus the aim of this research is as follows:

i. *Development of compliant flexure based mechanism*

To facilitate the design and development of effective FiTS mechanism, the study of flexure hinges geometric parameters and orientation proves to be important. A monolithic flexure based micro-gripper will be developed and tested for various geometric parameters and orientation configurations. The outcome of the study will be incorporated in the development of the FiTS system.

ii. *Study of Machine characteristics for Real Time Error Compensation*

To understand the performance characteristics of the machine tool in which the real-time error compensation to be implemented plays a vital role in this research. A diamond turning machine (DTM) is selected to implement the dual servo system since DTM can achieve the final finished component without the need for any further processing. So the accuracy of the DTM machine defines the final components' accuracy. By understanding the machine's behavior such as the axes form error, waviness and the following error, an effective compensation schema can be developed.

iii. *Development of Single axis FiTS and the Control System*

Development of a single axis auxiliary servo (FiTS) with utmost positioning accuracy, load-bearing capacity to withstand the micro-

cutting forces and response bandwidth plays a major role in real-time compensation of the geometric and following error. The developed dual servo FiTS system will be used to compensate geometric and following error with effective real-time commanding using a priority PLC in the machines' control system. The performance of the developed system will be evaluated using machining of flat and contour profiles.

iv. *Development of Dual Axis FiTS*

For a real-time compensation, a single axis FiTS is sufficient when the surface normal error (Geometric/Kinematic) components are along either the tool/spindle axis as in a flat face machining. A need for a dual axis system occurs while machining a contour surface in DTM. The surface normal error consists of two components, one along the tool/spindle axis and another along the tool-feed direction. So to compensate this error in real-time, a two axis FiTS is required. Hence, a two axis FiTS will be developed using planar flexure mechanism to compensate the geometric and following error of two axes of the DTM during contour machining operation. Simulation and the experimental findings of the performance of single and dual axis FTS based compensation will be presented.

2.6 Concluding Remarks

In this chapter, various literatures on the Fast and Fine tool servo are presented. From the literature, it is evident that various real-time tool positioning and compensation methods have been implemented. A dual servo

based compensation method proves to be an effective approach to compensate for static and dynamic error in real-time. Compliant mechanisms are predominantly used as the mechanical guiding unit in the FiTS systems for real-time compensation due to their inherent advantage of precise repeatable motion with reduced mass characteristics. Combination of pre-calibrated and real-time compensation schema can compensate the systematic errors and random errors. By this method, the need for a precise machine is reduced to a greater extent by use of the active error compensation system. In the following chapter, a systematic study on flexure hinge profile parameters and their effect on the performance of the mechanism are presented.

Table 2-1: Comparison of Real-time error compensation and components of errors considered

Author	Year	Error Compensation		Enhancement			
		Offline	Real-time	Surface Roughness (R_a)	Waviness (W_a)	Form error (P-V)	Following error (F.E.)
McCue, H [89]	1983		✓				✓
Kohno *et al.*[86]	1989		✓	✓	✓		
Fawcett *et al.*[82]	1990		✓	✓			✓
Miller *et al.*[87]	1994		✓			✓	
J.D.Kim *et al.*[83]	1998	✓			✓		
Xu *et al.*[91]	1999		✓	✓		✓	
Pahk *et al.* [88]	2001		✓				✓
Kim and Kim [84]	2003	✓			✓		
Wei Gao *et al.*[90]	2007	✓			✓	✓	
Gan *et al.* [92]	2009		✓	✓		✓	

Chapter 3 Fundamental Study On Flexure - Hinge Parameters

3.1 Overview

In this chapter, a new one dimensional, compliant, monolithic piezo-actuated micro-gripper mechanism is designed using different flexure hinge types and configuration are reported. The study is conducted in order to understand characteristics of various types of flexure hinges, a comparision of its parameters and effect of their configuration on the performance of the mechanism. A micro-gripper is designed and a comparison study on stress and output displacement characteristics of the microgripper by changing the hinge parameters –Thickness of the full circular hinge (*b*), web-thickness(*t*), radius of the hinge (*r*), location of the hinge, angle of inclination of the microgripper's input arm and comparison between the circular and the elliptical hinges for the same input is performed. Kinematics of the micro-gripper is analyzed based on input/output displacement for all the design variations using FEM and a kinematic model is arrived to emphasise the effect of hinges location. Using these results, an effective flexure based FiTS system for the real-time machine tool error compensation can be designed.

3.2 System Description

3.2.1 Design Stage

To manipulate small and delicate objects, precise and accurate manipulators are required. For such precise and a very small range of motion, conventional rigid body joints such as pin-joints, cannot be used due to their precision limitation of wear, backlash, misalignment due to the large number of component assembly etc. Flexure hinges are commonly used building blocks in precision components and in particular, microgrippers, in order to achieve an efficient and cost-effective device for micro-manipulation. A complete microgripper can be designed to be monolithic in structure by using flexure hinges, which overcome most of the drawbacks of conventional joints. Monolithic and symmetric structure is good for reducing mechanical noise, such as thermal and compliant errors [93]. Except for the limitation of motion and load bearing capacity, flexures hinges are used for their high level of accuracy and precision in microgrippers.

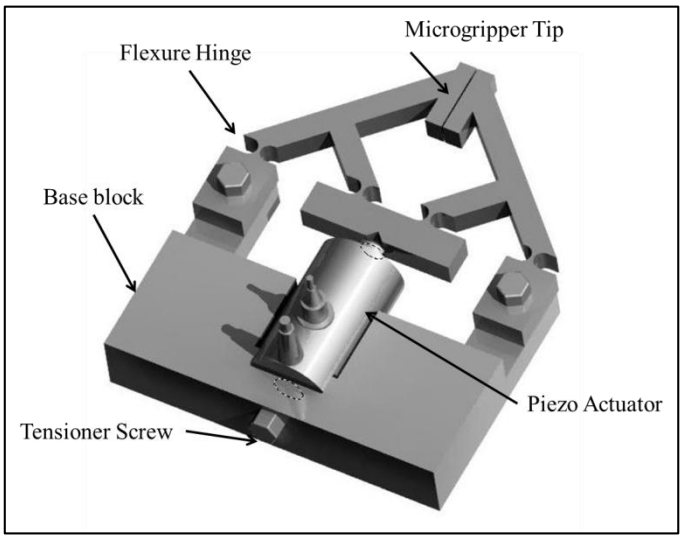

Figure 3-1: Designed Microgripper and PEA Assembly

The micro-gripper is designed to be planar using a single, monolithic piece of metal as shown in Figure 3-1. The flexure hinges provide the desired one-dimensional motion of the gripper arms and are stiffer in the other axes and its motion is achieved using the elastic deformation of the flexure hinge. The tip of the gripper designed in such a way that there is an initial gap (few microns) in order to make the microgripper to be of the "normally closed type". The main advantage of this setup is that the actuation is required only for opening the microgripper tip as the grasping action is obtained by the stored strain energy of the flexure hinges. This helps to grasp the object even in case of any system failure. The microgripper actuation provides a parallel motion to its tip, thus preventing the rolling of the micro objects while grasping. The small input to the microgripper is amplified at its tips by means of "class 2" mechanical leverage gripper arm. At the piezo actuation region of the microgripper a "V" groove is provided to prevent rotation of the actuator tip from rolling and slipping during high frequency actuation. The microgripper is designed to be modular in order to facilitate easier assembly and disassembly from the base plate unit. Solidworks software is used to model the microgripper. Totally 16 variants are modeled by maintaining the same basic structure except for the change in flexure hinge parameters as mentioned above.

3.2.2 Geometric modeling

In the geometric modeling, a generalized model is obtained based on the geometry and the hinge location in the microgripper. The Figure 3-2shows the initial and the displaced position of the gripper. In order to study the effect of the dimensions of the microgripper for given input displacement "*h*" and

orthogonal amplified output displacement of "*x*" (see Figure 3-2(b)). Hinges are shown as "*o*" at point A and C. Link AB and DC are designed to be orthogonal to each other at all conditions. α and β are the arm's angle with the horizontal. α' is the angle increment for a given input displacement of "*h*" as shown in Figure 3-2(b)).

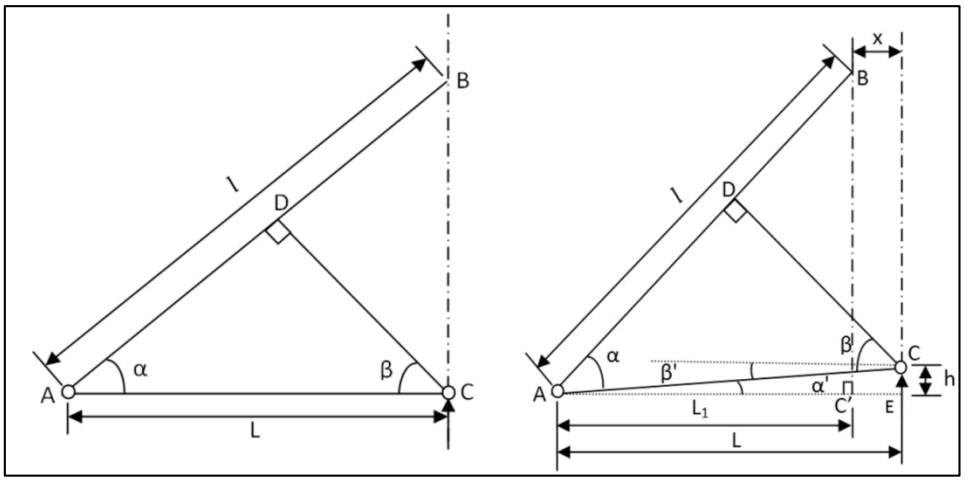

(a) (b)

Figure 3-2: Kinematic model of the gripper (a) before actuation (b) after actuation

$$x = L - L_1 \tag{3-1}$$

From triangle ABC' in figure 4,

$$\cos(\alpha + \alpha') = {}^{L_1}\!/_{l} \tag{3-2}$$

From triangle ADC in figure 3,

$$\alpha = \sin^{-1}({}^{CD}\!/_{L}) \tag{3-3}$$

From triangle ACE in figure 4,

$$\alpha' = \tan^{-1}({}^{h}\!/_{L}) \tag{3-4}$$

$\alpha' = \beta'$<< small for all configurations

Substituting in equation 3-1, displacement

$$x = L - l \times \cos(\alpha + \alpha') \tag{3-5}$$

Following findings were arrived at from the geometric modeling study:

a) To increase the "*x*" either increase "*L*" or decrease "L_1" based on eqn. 3-1.

b) The effect of decreasing the "*L*" value is lesser in eqn. 3-4 (α') as the input displacement (*h*) by PEA is in the range of few micrometers while "*L*" is in mm.

c) When "*L*" is increased, α and α' decreases based on equation 3-3 and 3-4. Therefore the cosine term in the eqn. 3-5 increases and hence the output displacement decreases.

d) Also by increasing "*L*" the arm length, "*l*" also increases which increases the overall dimension of the microgripper.

e) Alternatively, the output displacement is increased by reducing the hinge distance "*L*". By decreasing "*L*", the arm length "*l*" is reduced and arm angle α increases from eqn. 3-3.

f) The cosine term of eqn. 3-5 is reduced and the output displacement is increased. Also the overall size of the microgripper is reduced.

3.2.3 Finite Element Analysis

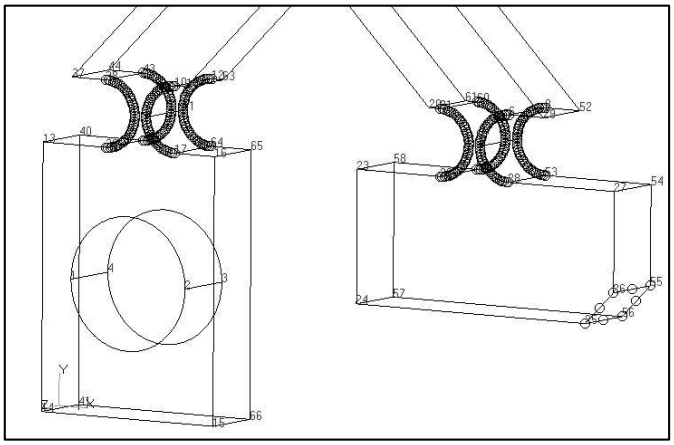

Figure 3-3: Mesh seeds created at the hinge regions before meshing

The models are saved as a STEP AP203 format in Solidworks and imported back into Patran for the analysis. Mapped meshing is used in the high stress concentration area mainly the flexural hinges since mapped meshing provide better control of the distribution and size of elements in a given area [94]. Therefore, before meshing the elements, the shorter edges and the flexure hinges are provided with special attention by "Mesh Seed" option (Figure 3-3). Through this method better control of meshing over the stress concentrated area is obtained. All the shorter edges are divided into 2 elements making sure that atleast 3 nodes are present on them and for the hinge curvature region the chordal tolerance is set to 0.001 and quadratic element order is selected. Equal element lengths are maintained in the hinge region to reduce the computational error.

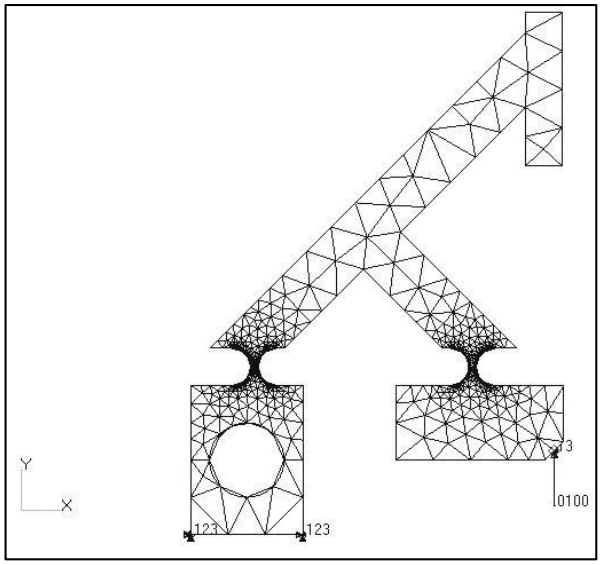

Figure 3-4: Half-symmetric configuration with the mesh and constraints

In order to reduce the computation time for analysis, the half-symmetric model of the microgripper is used. The microgripper is constrained at the base and a point input is applied at the center of the microgripper as shown in Figure 3-4. The material used for the analysis is steel with material properties as shown in Table 3-1.

Table 3-1: Average strength characteristics of steel

Property	Value	Units
Elastic Modulus	205,000	MPa
Poisson's Ratio	0.33	---------
Mass Density	7850	Kg/m3

3.3 Theoretical analysis

In the simulation, different configurations of microgripper are analyzed based on the following variations:

a) Flexure hinge parameters

1) Thickness (*b*) of the microgripper – 3mm, 5mm and 6mm plates

2) Radius of the flexure hinge (*r*)

3) Web-thickness (*t*) of the flexure hinge

4) Comparison of elliptical hinge and the right circular hinge with same web-thickness *(t*)

b) *Orientation*

1) Angle of input and actuation arms - 45°, 50° and 55°

2) Position of the flexure hinges

In FEA all the factors including the displacement, induced stress and the forces were considered.

3.3.1 Flexure hinge parameters

3.3.1.1 Effect of flexure hinge thickness (b) variation

The microgripper is designed using a monolithic block and hence the thickness of the microgripper corresponds to the hinge thickness (*b*). Analysis of the half-symmetric gripper is done for the thickness of 3mm, 5mm and 6mm. Both input displacement and force are plotted against the output tip displacement. As the thickness of the hinge increases, the output tip displacement for a given input displacement remains constant but the stress induced in the hinges increases with the increment of hinge thickness. However, for the same magnitude of input force, the displacement obtained at the tip decreases (Figure 3-5). This is due to the increased stiffness of the flexure hinge with increase in its thickness. Since the output displacement decreases, the stress values decrease correspondingly.

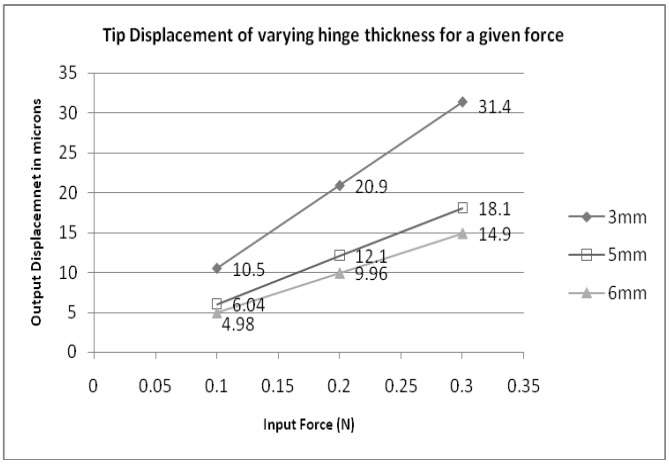

Figure 3-5: Tip displacement of varying hinge width for a given force

3.3.1.2 Effect of flexure hinge radius (r)/height variation

The radius of the flexure hinge is varied (2.5mm, 3mm and 3.5mm) which in turn increases the height of the hinge. With an increase in radius (See Figure 2-6 from Literature review chapter), the tip displacement remains constant and the stress value decreases for a given input displacement. This is mainly due to the same amount of input motion and considerable decrease in the angular stiffness. In addition, the change in the cross-section of the hinge is more gradual with the increase in radius. For a given input force, the output displacement and stress value increases with an increase in the radius (See Figure 3-6). This is again due to the decrease in the bending stiffness of the hinge with the increase in the height of the flexure hinge. For an increase of height by 1mm, there is an increase in output displacement by16% and a 40% reduction in the stress values.

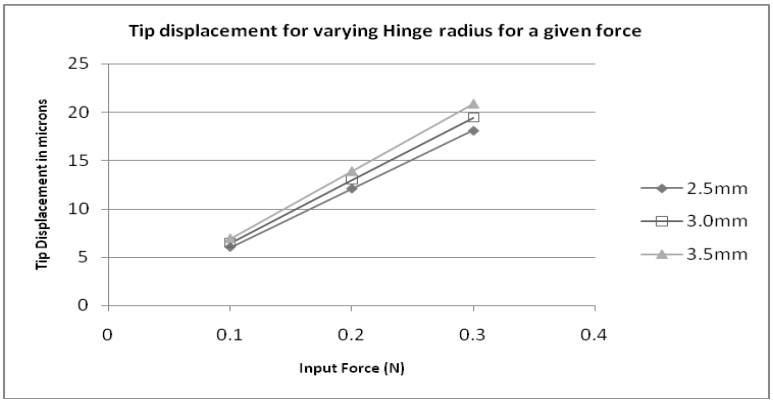

Figure 3-6: Tip displacement of varying hinge radius for a given input force

3.3.1.3 Effect of flexure hinge web-thickness (t) variation

The effect of variation of web-thickness of the hinge (*t*) is studied. The web-thickness is maintained as 0.75mm, 1mm, 1.5mm, and 2mm. As the thickness increases the output displacement decreases for a given input force/displacement. As the web-thickness increases, the bending stiffness of the hinge increases and decreases the hinge motion. The stress value decreases due to increase in the cross-sectional area and reduced output motion of the hinges. In order to study the effect of the manufacturing error, the hinges are modeled in SolidWorks^{TM} with web-thickness of 1.02 mm and 0.98 mm. The FEA results revealed that the manufacturing tolerance plays a major role in the stress induced in the hinges. For an increase in the thickness by 0.02mm, there is a decrease of 5% of stress value.

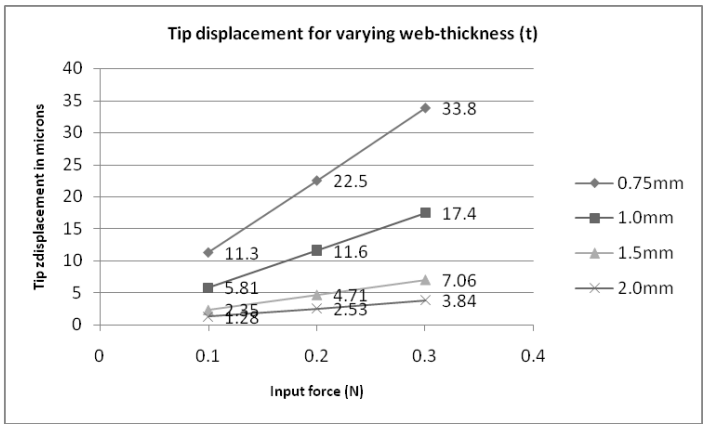

Figure 3-7: Tip displacement for varying web-thickness for a given input force

For a given input force, the output tip displacement reduces by around 50% for an increase in web-thickness by 0.25mm (Figure 3-7). The value of displacement for an input of 0.1N reduces from 11.3 micrometer to 5.81 micrometer for t = 0.75mm and t = 1.0mm. Similarly, for another 0.50mm increase in web-thickness, the tip displacement decreases by 68%. This shows that the output is in accordance with eqn. 2-1 since the bending stiffness K_B increases by a value web-thickness raised to the power of 2.5 times.

3.3.1.4 Comparison of elliptical hinge and the right circular hinge with same web-thickness (t)

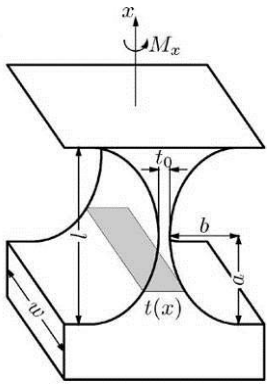

Figure 3-8: Elliptical Hinge [95]

The results for the case presented above are compared with the new set of flexure hinges with elliptical profile. The same web-thickness (t_0) of 0.75mm, 1mm, 1.5mm, 2mm are maintained but with the radius "*r*" replaced by "*b*" and height of the hinge "*h*" is replaced by "*2a*" (See Figure 3-8). The output of the elliptical hinges is more in terms of displacement and lesser in terms of stress value when compared with circular hinge of same web-thickness for a given input displacement. There is an increase in the value of tip displacement by about 4.25% for a web-thickness of 0.75mm and about 2.5% for a web-thickness of 2.0mm. There is also a decrease in the bending

stress value (by 9-10%) because of gradual change in the cross-section in comparison to the right circular hinge. The compliance equation for the elliptical hinge [23] is provided by the following equation:

$$K_B = \frac{\left(2Eba^2\right)}{3\varepsilon^3 f(\varepsilon\beta_x)} \tag{3-6}$$

Where, $\varepsilon = \frac{a}{b}$, Ratio of major axis to the minor axis

$$\beta_x = \frac{t_0}{2a}$$

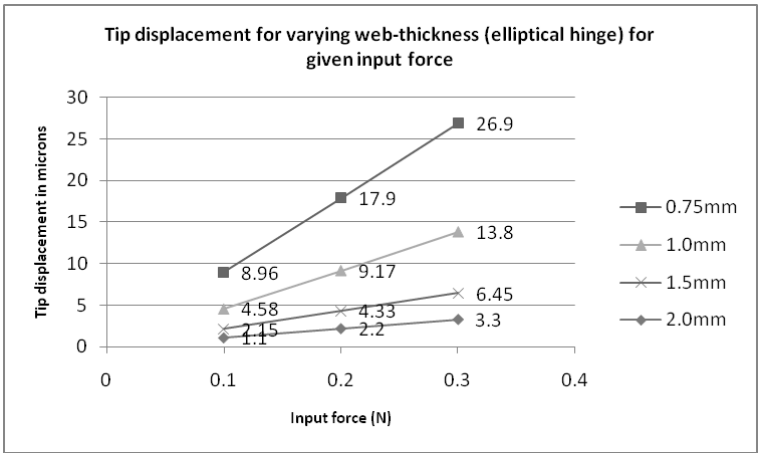

Figure 3-9: Tip displacement for varying web- thickness of elliptical hinge for a given force

The bending stiffness of the elliptical hinge is given by equation 3-6. However, for the case of application of input force, the results are in contrast when in comparison to input displacement. This can be attributed to the fact that since the change in cross section of elliptical hinges is gradual, the bending stiffness and the strain energy stored in the hinges are higher as in comparison to a right circular hinge of same web-thickness. Hence the output displacement reduces by about 21% (Figure 3-7&Figure 3-9) and there is a corresponding decrease in the stress values developed in the hinge.

3.4 Actuation arm orientation

3.4.1 Effect of input arm angle variation

As the angle of the input arm angle "*A*" (Figure 3-10) increase there is a tendency of minor decrease in the tip displacement (but remains nearly same). In addition, the Von-mises stress value decreases as shown inTable 3-2.

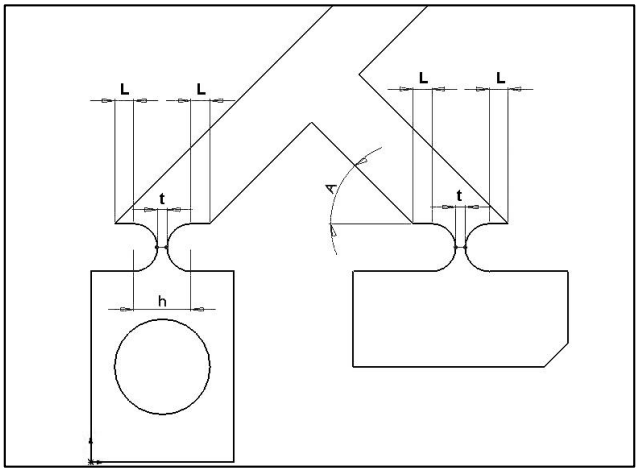

Figure 3-10: Symmetrical hinge position with various hinge and Input arm parameters

Table 3-2: Tip displacement and maximum stress values for varying input arm angle (*A*)

Input Displacement (μm)	Input Arm Angle (A)	Output Displacement (μm)	Stress (MPa)
10	45	19.8	17.5
10	50	19.8	17.3
10	55	19.7	17.1
20	45	39.7	35
20	50	39.5	34.6
20	55	39.3	34.2
30	45	59.5	52.5
30	50	59.2	51.9
30	55	59	51.6

This tendency of decrease in both output tip displacement and stress

value is due to the upward movement of the intersection between the input arm and gripper arm. This in turn reduces the amount of moment transmitted to the flexure hinge of the output arm.

3.4.2 Effect of position of flexure hinges variation

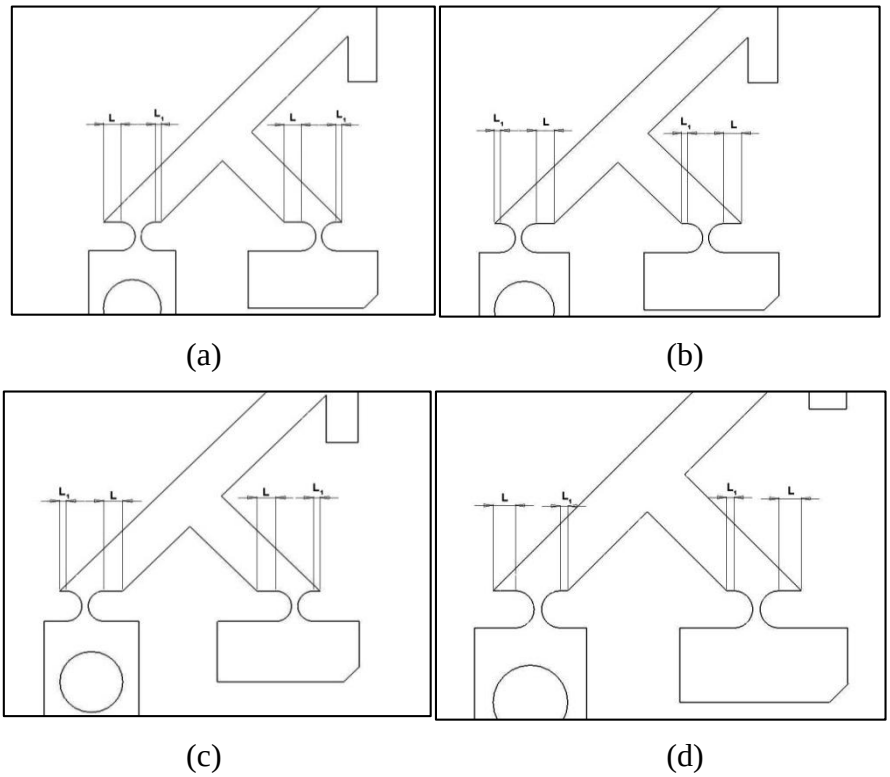

Figure 3-11: Variations of Hinge location (a) Right Offset (b) Left Offset (c) Left-Right Offset (d) Right-Left Offset

In the study, the position of the two hinges changed with respect to each other. From the results, it was found that the location of the hinge with respect to the position of force input plays a major role in the output tip displacement. The symmetrical structure (Figure 3-10) and either right offset (Figure 3-11(a)) or the left offset (Figure 3-11(b)) combination has the same output displacement for a given input displacement ("*L*" is maintained constant). The left-right combination (Figure 3-11(c)) produces a lesser output displacement for the same input displacement as distance between the hinges "*L*"

(SeeFigure 3-2) is more). For the right-left combination (Figure 3-11(d)) the output displacement is considerably more in comparison to the other configurations ("*L*" is lesser). The output displacement is about 17% higher than the left-right combination and about 10% higher than the rest of the configurations. The input versus output displacement is shown in Figure 3-12. Since the output displacement for the right-left combination is more, the induced bending stress of flexure hinges is more for right-left combination in comparison to all the other combinations. Similar results were obtained for a given input force, but the ratio of output displacements of the right-left combination to the right-right combination is lesser as in comparison to the ratios of output displacement for an input displacement scenario.

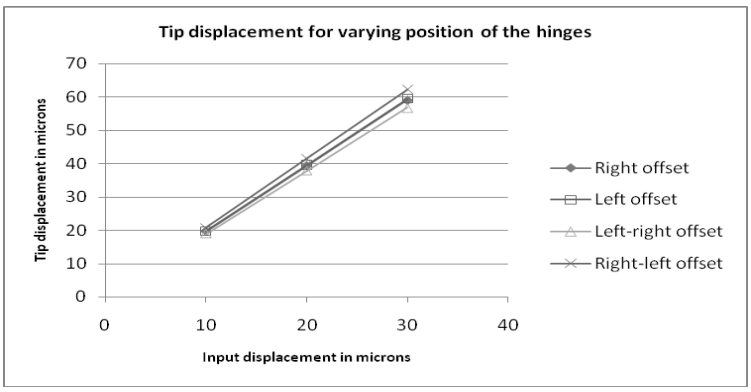

Figure 3-12: Plot between Input and Output displacement for all above combinations

Figure 3-13 shows the schematic concept of the location of the flexure hinges, the extreme positions and the force actuation point. The right-right and right-left combinations have the least distance between the hinges in comparison to all other combinations. Between the right-left and right-right combination, the former has more leverage between the right extreme position of hinge and the force actuation point. This produces increased moment for right-left combination which in turn is translated as output tip displacement.

Similarly least output is obtained for the left-left and left-right combination due to the larger distance between the hinges.

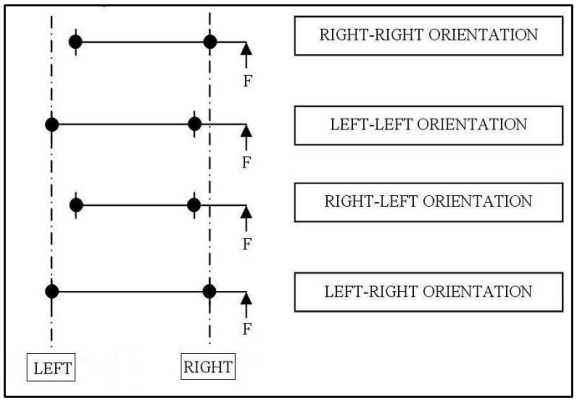

Figure 3-13: Schematic diagram of the various combinations with the hinge location

3.5 Performance testing of the microgripper

3.5.1 Experimental Setup

The analytical results reveal that flexure hinge parameters and the location of the flexure hinges play an important role in the performance of the microgripper. All the variants that were analytically modelled are fabricated and an experimental setup is created based on the following schematic diagram (Figure 3-14). The experimental set up consist of the PEA, microgripper, control unit to operate the PEA and the digital microscope to measure the displacement of the microgripper input and output. The function generator produces the pulse, which serves as an input to the amplifier unit. The amplifier produces the input pulse for the PEA. The output of the function generator is monitored using an oscilloscope in order to provide a measured amount of voltage to the PEA. The PEA with a maximum displacement of PZT is 20μm is used in the experiment. The PEA is provided with a built-in

strain gauge feedback, which provides closed loop control for the PZT's displacement.

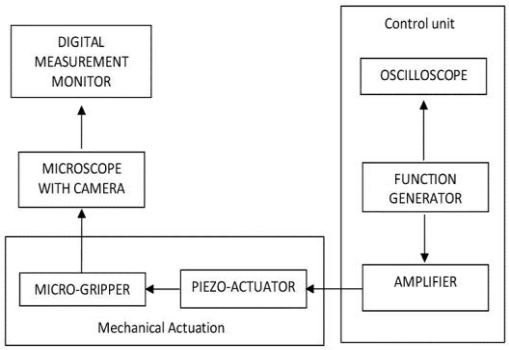

Figure 3-14: Schematic representation of the experimental set-up

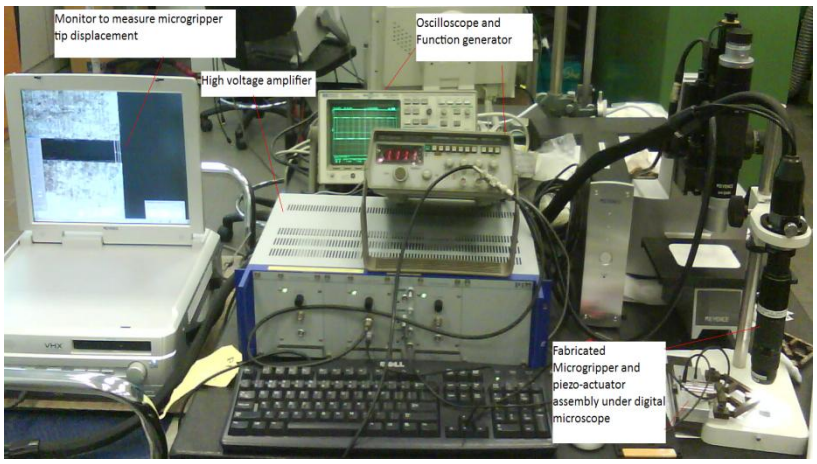

Figure 3-15: Photograph of experimental setup

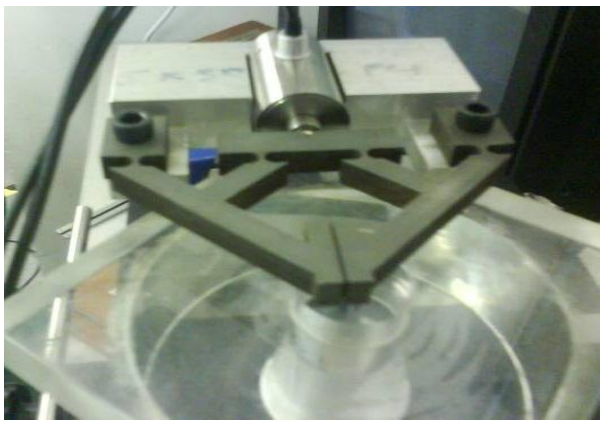

Figure 3-16: "Close-up" of fabricated microgripper and PEA assembly

The fabricated microgripper and PEA are mounted on to the base block. Figure 3-15 and Figure 3-16 displays the photograph of the experimental set-up and the fabricated microgripper mounted on to a base block, respectively.

The microscope has the resolution of 450 times and for the experiment, 175 times magnification was used to visualize the amplified tip displacement of the microgripper.

3.5.2 Experimental study of position of Flexure hinges

Experiments were conducted to find the output tip displacement for various input displacement values. The input/output displacement study was performed. Figure 3-17 shows the various displacement values of the PEA for a given input voltage. Since the FEA results for the gripper arm orientation and thickness variation studies showed similar output tip displacement for a given input displacement, they were not fabricated. All the other variants have been tested and the results are compared with the FEA values. Both the FEA and the experimental results of flexure hinge location (4 variants) has been compared and plotted in the graph below (Figure 3-18).

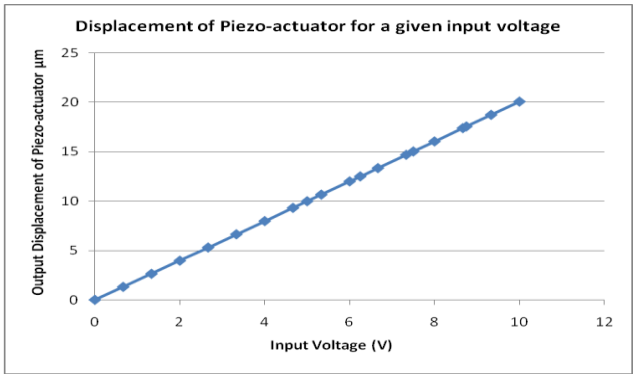

Figure 3-17: PEA calibration for a given input voltage

The experimental output displacement was found to follow the same pattern as that of the FEA results. The Right-Left combination provides the maximum output displacement for a given input displacement. Similarly, the elliptical hinges perform better than their right circular counterpart does, which is due to the inherent difference in their bending stiffness provided by

equation 3-6. However, the experimental results of the output tip displacement are found to be lower than the computed FEA results for all the combinations. This is due to the "lost motion" situation pursuant to hinge stretching due to axial force. Furthermore, due to manufacturing error it is possible that both the levers do not provide the same movement and hence there is a probability of un-symmetrical motion, which accounts for lost motion.

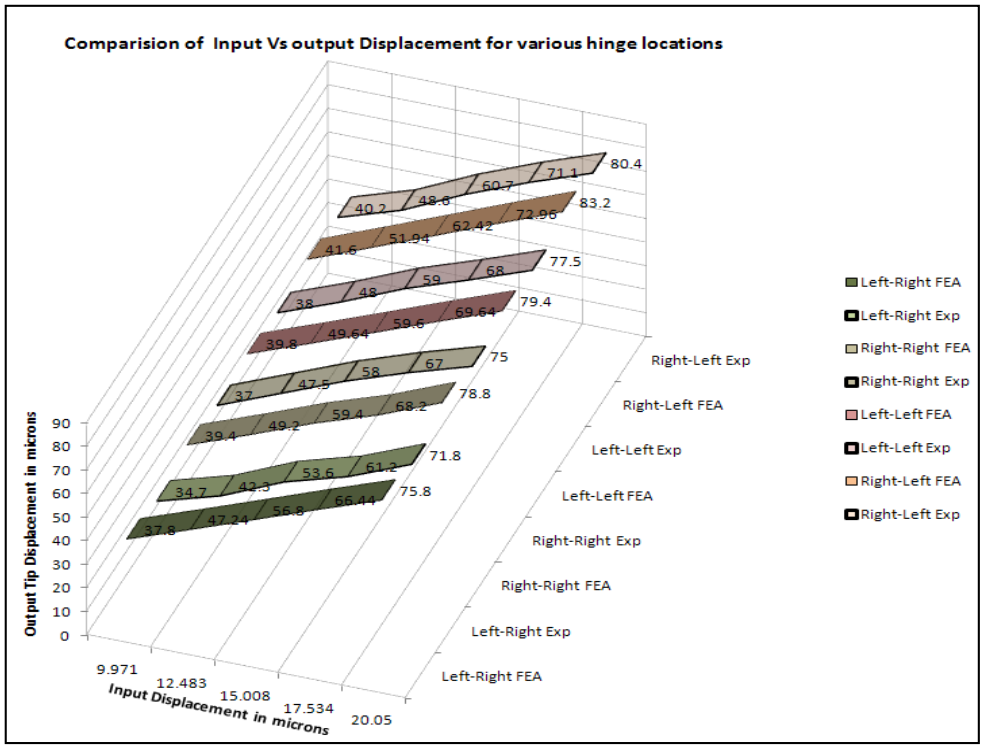

Figure 3-18: Comparison of Theoretical and Experimental values for various hinge locations

As mentioned above in the geometric modeling section, even though the location of the flexure hinges plays an important role in the ouput performance of the microgripper, they are also dependent on the flexure hinge parameters. The FEA results show more gripper tip displacement for right-left orientation in terms of given input displacement but for a given input force similar tip displacement was achieved by both right-left and right-right combination. This is because the flexure hinge parameters and their

corresponding angular stiffness are responsible for the complex rotation which in turn affects the output tip displacement performance of the microgripper. In the input displacement scenario, the microgripper is forced to move to a particular value and the stress developed is not considered. However, for an input force, the Right-Left combination has lesser stress induced in comparison to the Right-Right combination, which can be seen from the FEA results. Both FEA and experimental output of the gripper tip displacement for varying hinge radius "*r*" (See to be added from intro chapter) also showed a similar trend for all the variations of the microgripper.

3.5.3 Comparison of performance of Elliptical and Right circular hinges

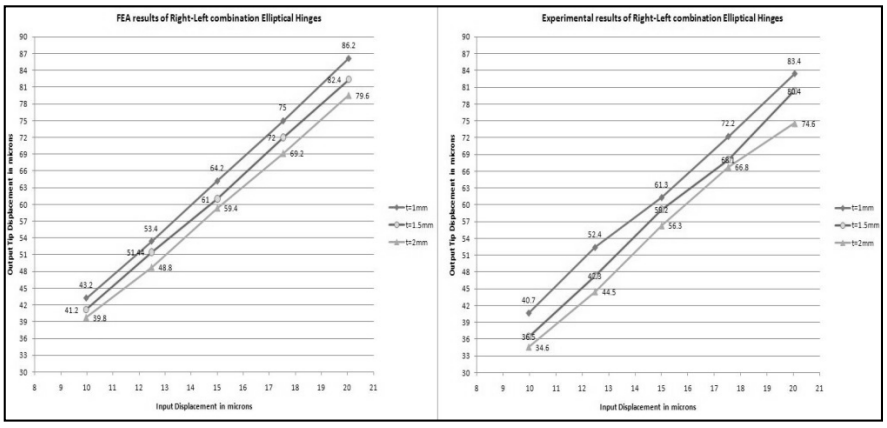

Figure 3-19: Plot results of Input and Output displacement of elliptical hinges (a) FEA and (b) Experimental

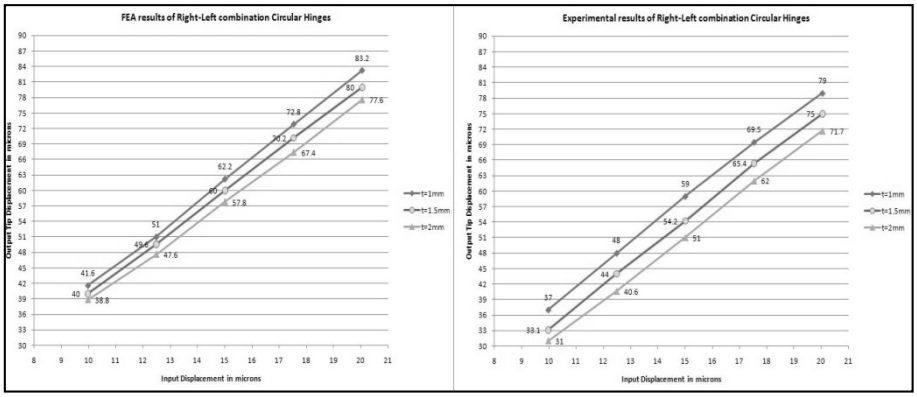

Figure 3-20: Plot results of Input and Output displacement of circular hinges (a) FEA and (b) Experimental

Similarly the experimental validation of right circular and elliptical hinges with varying web-thickness is performed and results of both FEA and experiment are plotted in Figure 3-19(a) & (b) and Figure 3-20(a) & (b) respectively.

3.6 Results and Discussion

A two-dimensional compliant monolithic piezo-actuated microgripper was designed and a validation of geometric modelling is performed using FEM. All the different hinge configurations were analyzed and results are recorded and listed below:

- The main finding after the analysis is that the location of the flexure hinges (*L*) is more critical. The right-left combination of flexure hinge position provides comparatively more output displacement for a given input displacement as compared to other combinations. For a given input force right-right combination produces slightly higher displacement (about 0.01% more), but the stress induced in the flexure hinges is also higher (about 0.03% more).
- The analysis also shows that the thickness (*b*) and the web-thickness (*t*) determine the bending stiffness of the flexure hinge. The increase of these parameters increases the bending stiffness and hence reduces the output displacement.
- The radius of the flexure hinge (*r*) is inversely proportional to the bending stiffness of flexure hinge. The stiffness reduces and displacement increases with the increase in radius.

- As the angle of input arm (*A*) is increased there is only a minor decrease in the output displacement and corresponding stress values. This variation is found due to the change in the input arm position. However as the flexure hinge parameters are not altered, there is not much effect on output displacement.
- Comparison between web-thickness of circular and elliptical flexure hinges showed that the output displacement is higher for elliptical hinges with reduced stress values because of the gradual change in the cross-sectional area of the flexural hinge. But for a given input force, the results were vice-versa. This is due to the increase in bending stiffness values for an elliptical hinge as compared to a circular hinge with the same web-thickness.
- Experimental results also confirm the above findings and follow the same pattern as that of the FEA results, even though the experimental results were found to be lesser due to "lost motion" by around 5%
- Right circular hinges provide better output displacement (around 25%) for given input force in comparison to the elliptical hinges.

3.7 Chapter Conclusion

The results from the monolithic microgripper design using complaint mechanism proves that the flexure hinges location and profile of the hinge parameters are important to attain the required displacement amplification and load bearing capacity. Using the findings of the one dimensional displacement, further studies are carried out to develop the compliant FiTS system to enhance the machine tool accuracy. A diamond turning machine (DTM) is

chosen for the current research, due to its capability to produce the final finished components without any further finishing process. Hence, before implementing the real-time FiTS based compensation, the performance characteristics of the DTM is studied in the following chapter.

"Perhaps the most important difference between abrasive processing and diamond turning is that, with abrasive processing, the size, shape, arid surface-finish requirements are not easy to satisfy simultaneously.... In diamond turning, the part is sized, shaped, and finished in one relatively quick operation. The result is often large savings in manufacturing costs." – McClure [96]

Chapter 4 Study of Performance Characteristics of Diamond Turning Machine Tool

4.1 Chapter Overview

In this chapter, the configuration of the diamond turning machine (DTM) is presented. An insight on the individual components of the DTM and their role on the machine tools performance are highlighted. Various machine tool errors in conjunction to the DTM are explained. Since the understanding of the DTM's performance is important, prior to the implementation of the compensation methodologies, the basic metrology, calibration and machining tests are conducted. Followed by, a discussion on the outcome is presented.

4.2 Diamond Turning Machine

In order to test the proposed FiTS system for the machine tool error compensation we had selected a diamond turning machine (DTM) as shown in Figure 4-1. Basically non-ferrous based materials such as copper, aluminum and brass are diamond turned to achieve a surface roughness of a few nanometers and form/contour accuracy in the sub-micrometer range. McClure [96] mentioned that a DTM can produce the final finished component with the required ultra-precision, in one single set-up without the need for a secondary process. The main reason for selecting a DTM is that, by the diamond turning process we could achieve the ultra-precision finish for optics and lens mould

components without the need for any further finishing process. The finished surface can be used for identification of the machine tool errors which can be eliminated by the proposed real-time compensation technique. Also the improvement in the accuracy of the DTM machine will directly reflect on to the workpiece surface integrity enhancement. Also, in addition to the finishing operation, FTS based micro feature generation such as MLA and free-form surfaces can be achieved in a single set-up in the DTM. For micro features, the precision needs of the DTM become stringent and errors have to be limited to nano/sub-nanometric level. Hence by implementing the real-time active compensation on DTM, the effectiveness of the FiTS system can be realized.

Figure 4-1: Ultra-precision DTM

Basic setup of the ultra-precision lathe consists of mechanical components, electrical motors along with their drivers and a machine tool control system. A host personal computer is used to communicate the machine tool using a custom developed graphical user interface (GUI). The basic mechanical components consist of a T-shape configuration of the *X*- and *Z*-

axis with two V- slide ways with high precision pin roller guides. An air-bearing spindle mounted on the *Z*-axis slide, while the tool post is mounted on to the *X*-axis slide.

A monolithic granite base is used to mount the T-shape configuration of the X- and Z-axis in order to reduce the machine tool vibration during machining. In addition, the base of the granite rests on four heavy duty passive dampers to reduce the transmission of vibration from the ground. The X- and Z-axis translational slides are driven by high performance ironless linear motor system with full-closed feedback control. The position feedback of *X*- and *Z*-axis slides is measured using linear scale (one for each axis) with grating size of 20μm and an interpolated resolution of 5 nm. The overall travel range of *X* and *Z*-axis is 40 mm, respectively. For the air bearing spindle (*C*-axis), a double sphere spindle is used to rotate the workpiece with the rotational speed of 100 to 5,000 rpm. The photograph of the DTM working space with the mechanical components is shown in Figure 4-2.

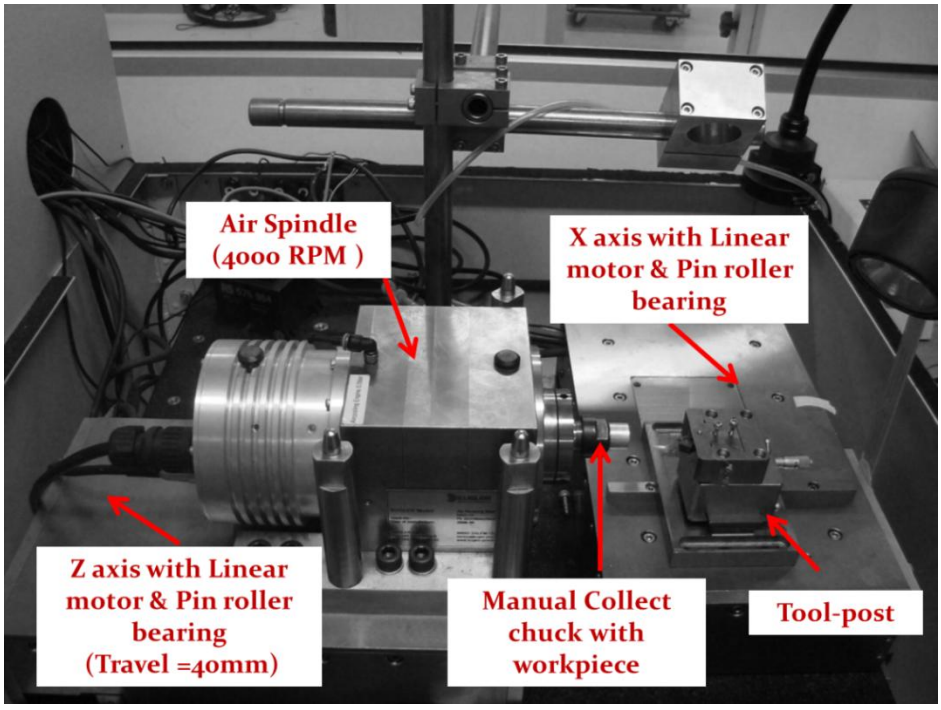

Figure 4-2: Working area of Ultra-precision Diamond turning lathe

4.2.1 Machine Controller

The developed ultra-precision lathe is being controlled by a motion controller consisting of 80MHz CPU with battery backed RAM to provide back up to the stored machine parameters. A single controller system can control up to eight axes (four servo motor and four stepper motors) and 24-digital I/O points with a great level of accuracy and simplicity of operation [97]. The controller CPU unit consists of a 480 Mbit/sec USB 2.0 communications interface to communicate with the host computer. The machines' controller is configured to interface with amplifiers, servo motors, and linear encoders by an axis expansion board. I/O card can accommodate upto 24 I/O in order to read the machine hard limits during its motion and to actuate and sense other auxiliary and safety components to ensure proper working of the machine tool motion.

4.2.1.1 PLC Programming

A Real-time interrupt (RTI) controls how often certain time-critical tasks are performed. They occur immediate after the servo update tasks at a rate controlled by parameter *"I8"*. Machine controller consists of 32 PLCs which are numbered 0 through 31. PLC program 0 is a special program that operates at the end of the servo interrupt cycle with a frequency specified by the controller parameter *"I8"* (every I8+1 servo cycles).

4.2.2 Human-Machine Interface (HMI)

A manual pulse generator (MPG) is used in order to manually set the tool-workpiece interface using a high resolution camera monitor. The machine tool motion is commanded by the custom GUI developed using C/C++ and the

dynamic link library files (.dll) provided by controller manufacturer. The customization software is used to configure and interface with the machine tool axes and the controller. The initial conditions such as the PID values and the machine related data such as the compensation tables from the Laser interferometer reading for smooth and precise motion of the motors are also stored into controllers' memory using the customization software. The developed GUI helps in providing a gateway for the user to perform all the basic machine tool commands such as homing, MDI mode commands and to input the NC program in order to perform the machining operation.

4.2.3 Machining environment

To achieve good machining finishes, a good machining environment with thermal stability is required. The machine was put into a clean room to keep the stable temperature of 21°C. The temperature fluctuation in the clean room is maintained to be ±0.5°C.

The comprehensive DTM specification is listed in the Appendix A.

4.3 Error identification

The surface integrity of the machined parts is mainly influenced by cutting conditions, environmental conditions and machine tool characteristics. By considering the ultra-precision machine within a temperature controlled environment and cutting force is only a fraction of the axes/spindle axial stiffness for micro/nano depth of cut, the accuracy of the surface is greatly affected by the geometric and dynamic behaviour of the machine tool. Figure 4-3 shows the schematic of the error in the DTM during a facing operation. The major geometric errors which are transferred from the axes to the machine

workpiece are the form and waviness of the tool axis and the dynamic following error of the workpiece axis. The performance of the DTM is studied and the geometric and kinematic errors in the DTM are measured and their effect on the machined surface is explained with respect to facing operation. Since the surface integrity during a facing operation depends mainly on the surface-normal errors along the Z-axis, the error with respect to the spindles' axial directions are studied. From the Figure 4-3, it can be understood both the form and waviness along the X-axis gets reflected in the workpiece during a facing operation. In addition to these error motions, the following error along the Z-axis plays a major role in the achievable surface roughness.

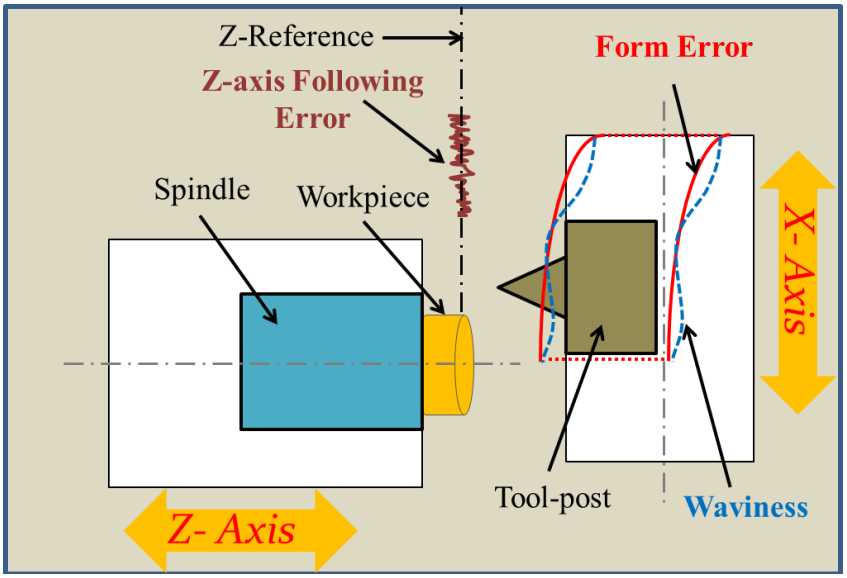

Figure 4-3: Schematic of Geometric and Kinematic error components in DTM

In the following section,

- The positional accuracy of the machine which defines the achievable controlled positioning of the axes is studied.
- Form of the axes is measured along the spindle face since the machined surface which is parallel to the spindle face and any form error between the axes will be directly reflected on the machined

surface. Also it will provide an effective way to understand the compare the machines' performance and surface integrity of the machined surface.

- The following error which is the real-time difference between the actual and the commanded position of the axes are measured to showcase its effects on the surface roughness of the machined workpiece.

From these measured data, one could understand the state of the DTM and strategies can be developed to implement a real-time compensation to improve the surface profile without allowing the error from being translated to the machined workpiece.

4.3.1 Geometric Error

4.3.1.1 Positional Accuracy of X and Z axis

The positional accuracy of the axes is the exactness between the actual and the commanded positions. Since the DTM is equipped with a high resolution (5 nm) encoder, a higher capability system is required to calibrate it. Hence a laser interferometer with 1 nm resolution was employed to measure the accuracy of the translational slide. The measurement was set to be 5 mm interval for 40 mm measured length. The *X*-axis translational slide was controlled to move in back and forth for multiple times in order to measure the positional accuracy and the repeatability of the machine slides. The results indicate the horizontal profile error of the *X*-axis translational slide with the error of 2.022 μm, while the waviness error with peak-to-valley of 1 μm is observed from the result. It is believed to be caused by the mechanical error

from the pin roller bearing of the guideways. Therefore, it is expected that this error will be reflected on the machine surface. Since these positional error are repeatable (Repeatability < 1 μm) and the values are few hundred microns, the machines' controller is used to compensate for the positioning error along each axis. A compensation table is computed by converting the error values to encoder counts and stored in the controllers' RAM. This data acts a look-ahead for the controller and the machine was able to perform with sub-micron accuracy after pre-compensation.

4.3.1.2 X axis form error measurement

The straightness of the axes with respect to the other axes is important in any machine tool. In the DTM, the main focus is to improve machine accuracy during flat face machining operation and the discussion will be focused towards the errors pertaining to the facing process. Therefore, in the following section, the geometric error of the DTM is studied. The machines' performance based on its profile accuracy is studied. The form of the finished workpiece depends on the perpendicularity between the X-axis (tool-axis) and the workpiece face as the perpendicularity between the two axes are important than the straightness of the X axis alone. Since the workpiece is mounted on to the spindle-face, the perpendicularity of the X-axis is measured directly along the spindle-face. The experimental set-up is as shown in Figure 4-4. To analyze the form of the DTM machine, a high resolution non-contact type capacitance sensor (CAP sensor) is used. The specification of the CAP sensor used in the study is given in the Table 4-1.

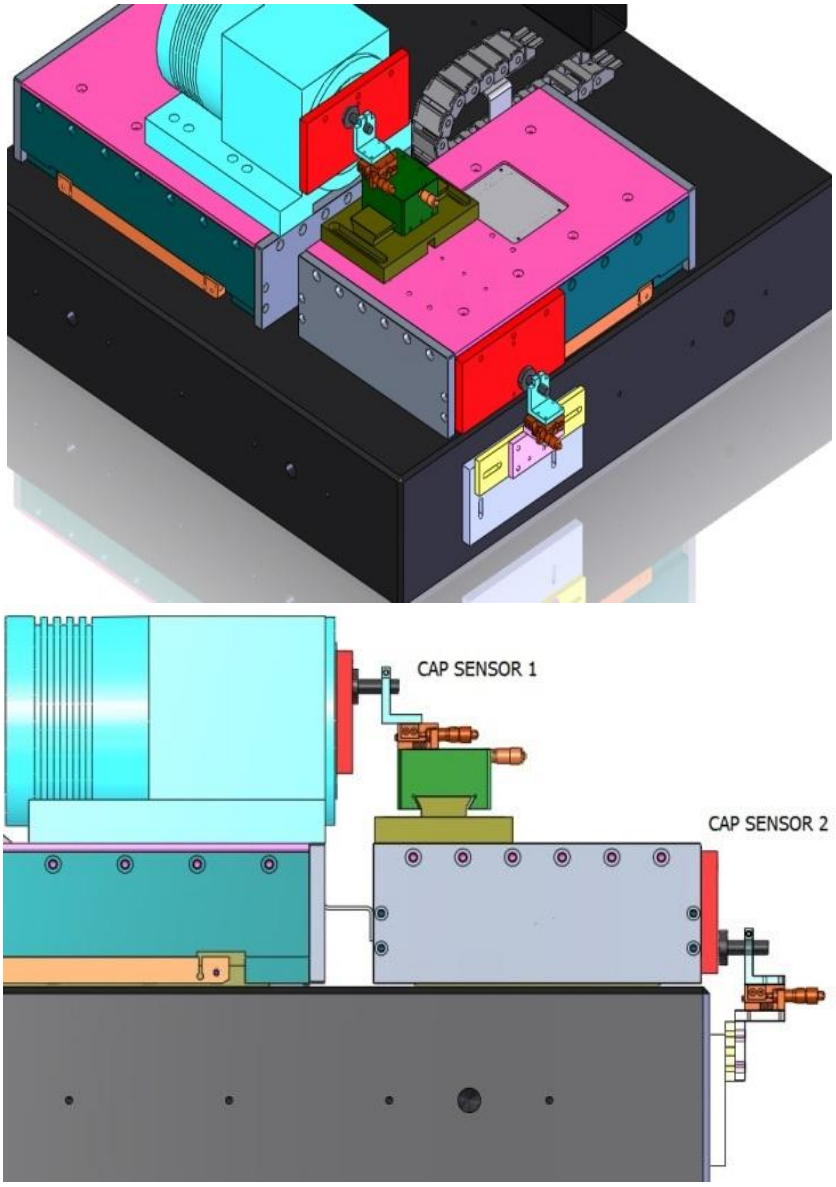

Figure 4-4: Capacitance sensor assembly for X axis form measurement

Table 4-1: Specification of capacitance sensor

Sensor type	Single-electrode capacitive module
Nominal measurement range	100 µm
Static resolution	10 nm
Dynamic resolution	10-20 nm
Sensor diameter	20 mm

Since the parallelism between the CAP sensor and measuring surface is very much critical, proper care has been taken in parallel alignment of the

sensor face and target measurement face during the measurement. In the initial experimental setup, the CAP sensor 2 was used to measure the deviation of the X axis along its travel (0-40mm) with respect to the machine's granite base which is considered as the reference while mounting the axes. Proper precautions are taken in order to align the capacitance sensor face to be orthogonal to the target measuring plate. The straightness error of the X stage with respect to spindle face is measured to be around 12µm for the whole travel length of 40mm (Figure 4-5).

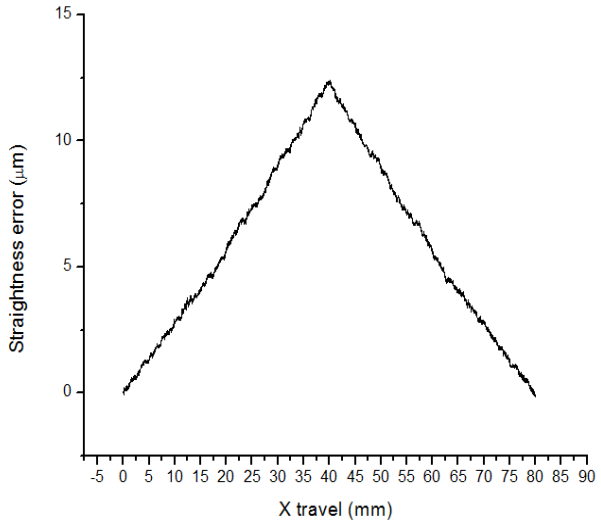

Figure 4-5: X axis form with respect machine table using CAP sensor 2

The profile is linear and with lesser noise disturbances from the machine servo since the measurement is made on the side-plate of the X-axis which is stiffer than the travel direction and due to damping effect of the large granite base. In order to capture the more realistic situation it is important to mount the straightedge flat plate on the spindle face and the sensor probe on the X-slide so that the measurement position can be identical with the cutting point [98]. The form error which is transmitted from the tool axis to workpiece is based on the perpendicularity between the X axis and the spindle face. CAP sensor 1 used to measure this error is as shown in Figure 4-4. The

perpendicularity between the tool face and the spindle face (Figure 4-6) appears to be different compared to the error measured using the CAP sensor 2. The error value obtained by the CAP sensor 1 is around 10µm and has a parabolic profile. Since the measurement is directly obtained with respect to the spindle face, this data consists of the form error along with other error components such as following error of Z axis and also the X-axis waviness. The accuracy of the machined workpiece depends on this form error as it will be translated to the workpiece during machining. The experiment has been repeated for few times in order to find the repeatability of the measurement value.

The influence of the form error with respect to the machine's table is lesser on the workpiece profile and hence this data (Figure 4-5) is not considered in the compensation procedure.

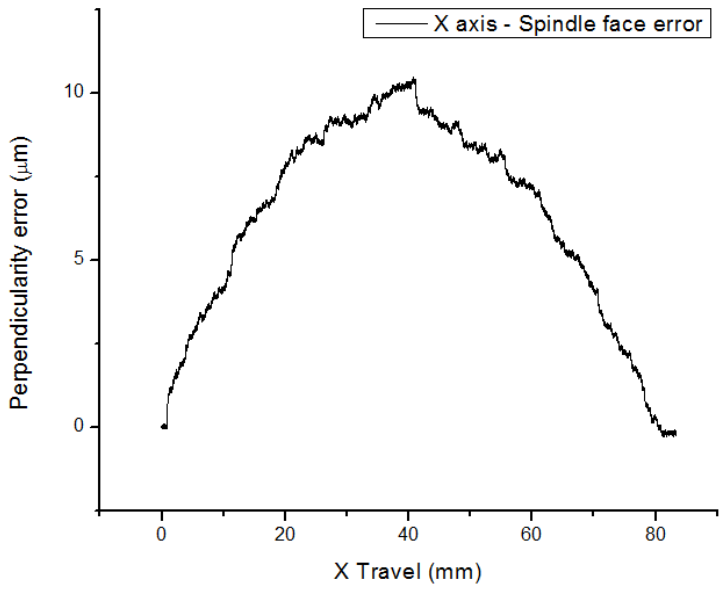

Figure 4-6: X axis form error with respect spindle face using CAP sensor 1

4.3.2 Kinematic Error

The other major contributor for the surface integrity deterioration is the kinematic error of the machine. The following error is one of the major kinematic errors in a machine tool. They have a direct impact on the achievable surface roughness value. Very less researchers have contributed in the study and compensation of the following error in real-time. So in the following section, a description and the possible causes of the following error are presented. Followed by, the measurement of the following error using an external sensor for initial study is conducted and the results are presented.

4.3.2.1 Following Error

The following error of machine tool is a type of kinematic error which is the inability of the machine axes to reach the commanded position by the controller. For the controller to work and apply the PID gain values effectively there needs to be a difference between the actual and the commanded positions (feedback servo error). Always there exists an erroneous motion in the axes which provides the controller its task i.e. to correct the error motion and maintain the desired output. The magnitude of this error plays a key role in determining the machines' performance and it depends on various factors:

- The tuning of the PID gain values imparts a definite amount of following error to the machine tool axes. For example, if the proportional gain K_p is set too high, the system gets much stiffer with lesser settling time but with a small amplitude, high frequency vibration of the axes. Also by feed forward *i.e.* feeding the position command into the velocity loop in the machine controller, provides

position loop gain control while moving. Apparently, feed forward increases the gain after a valid command to move. But it does not affect stability at standstill since no motion is commanded and the resulting following error is due to the vibration of the machine axes along the reference position. Also the sudden change in the federate, acceleration and direction at sharper corner machining provides a shock to the axes. Increasing feed forward (velocity and acceleration) reduces the following error, but is limited very much by the machines' response. The Figure 4-7 shows the typical following error of the DTM Z-axis during a to and fro ramp motion. The following error is computed by the machines' controller itself, based on the actual and the commanded positional data. The major peaks in the following error plot occur at the starting of the motion and again at the point where the axis changes its direction. This plot is similar to the explanation above. In addition to all these enhancements, the transmission delays due to longer cable distance and electrical disturbances due to unshielded cables leads to the vibration of the axes along the reference point.

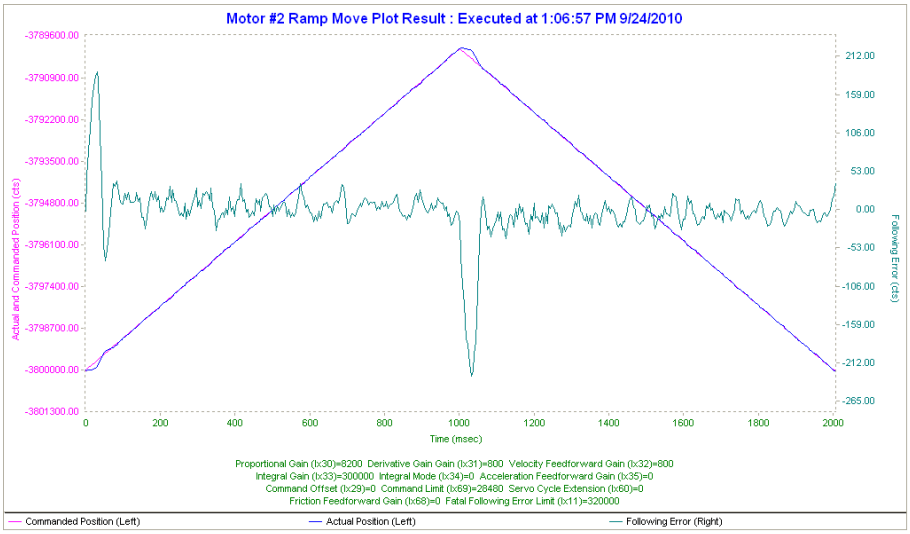

Figure 4-7: Following error of the X-axis during ramp motion tuning

- The performance of the machine tool depends not only on the efficient computation at the controller, but also on the amplifier of the motor which converts the commanded position from the controller to corresponding voltage based on the motor parameters. So the ability of the amplifier to work at the frequency of the controller with a resolution higher or at least equivalent to the encoders' resolution. Hence, to achieve higher surface finishes, a higher resolution encoder and amplifier-motor pair is required. Most commonly used amplifiers are PWM (Pulse-Width Modulation) type amplifiers which provide an output voltage in terms of steps. The resolution of such amplifiers is defined by the step value of the output pulse. Another type of amplifiers are the Linear direct drive type which does a straight forward conversion of input voltage from the controller to the output voltage to the axes motors as a linear function. In most of the sophisticated precision machines, linear drives are in use to achieve high precision.

- Though the machine tool is equipped with such high electronics, there exists a lag due to the mechanical system as mentioned in the previous chapters. Though the magnitude of these errors can be reduced, they are inevitable and will be present in the system. The mass of the axes which provides the necessary stiffness and damping capabilities to overcome the vibrational disturbances due to various machining forces, they reduce the response characteristics. Due to this, though the electronic controller and amplifier work at a very high frequency of few KHz, the response frequency of the mechanical system is still only few hundred Hz. This huge difference in the mechanical and controller frequency leads to following error of the axes which are of small amplitude and high frequency. Hence, to compensate this small magnitude error, by the machine axes in a lesser response time will make the axes unstable and vibrate along the reference position.

The following error is one of the causes for the surface roughness deterioration of the machined surface and the final machined surface finish is much higher than the one achievable by the ideal roughness equation

$$R_t = \frac{f^2}{8r}$$

where, R_t is the peak-to-valley roughness, f is the feed per tooth, and r is the tool nose radius. However, for most of the face turning processes the Z direction is considerably sensitive. Therefore, positioning errors in Z-direction are most significant because they directly affect the depth of cut. Thus, it is clear that horizontal straightness errors of the X-axis translational slide create form errors on a faced workpiece surface.

4.3.2.2 Static Following error measurement

In the following error measurement, the same non-contact type CAP sensor is used. Instead of measurement on the spindle face, the measure was conducted on a flat-plate mounted directly on the Z-axis. This method was implemented in order to capture the actual following error motion of the Z-axis and not to lose any data by measuring on the spindle face. The experimental set-up is shown in the Figure 4-8.

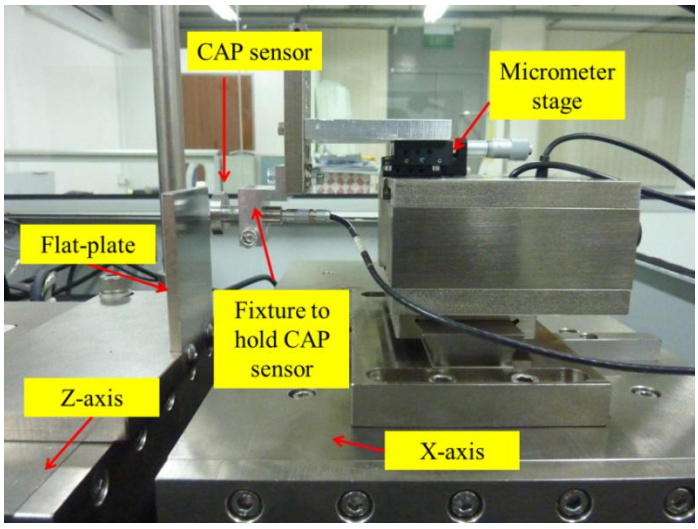

Figure 4-8: Photograph of static following error measurement set-up

From the experimental results (Figure 4-9), it is evident that the Z-axis displays a vibrational motion of around ± 100 nm (20 cts). The value measured agrees closely with the following error computed by the machines' controller during the ramp motion test (Figure 4-7). Since the CAP sensor is of non-contact type, they do not tamper the reading by providing any additional damping to the Z-axis.

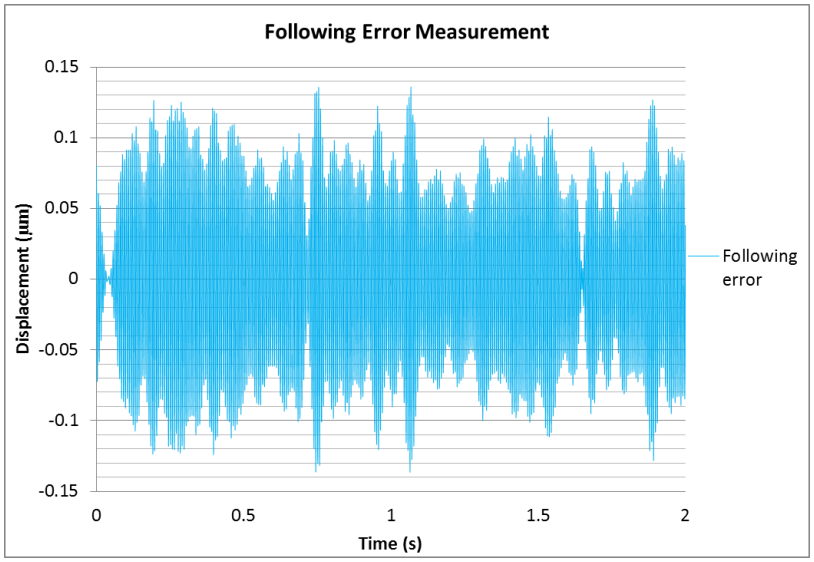

Figure 4-9: Z-axis following error data

From the above discussions, it is clear that the measured error information will have a considerable impact on the machined worpiece. Particularly, since the DTM are used in ultra-precision machining to produce mirror surfaces, these errors will reflect as a magnified surface irregularity in the nano-metric regime.

Since the waviness error is axes federate dependent, they are discussed in the next chapter, in which the waviness is identified from the machined flat workpieces and corresponding compensation mechanisms are implemented.

In the following section, an explanation on the workpiece surface integrity during a flat machining process in the DTM is presented.

4.4 Components of error

Various errors and their causes have been discussed in the previous sections. In order to understand the errors and their implications on the workpiece is discussed in this section. The requirement of a flat machined workpiece is to provide the necessary surface integrity such as roughness and profile. Due to the above mentioned inherent errors of the machine tool, there

exists a deviation from the expected value whose magnitude depends on the magnitude of the error. The Figure 4-10shows the exaggerated views of the various error components in the machined using a CAD model. Figure 4-10(a) shows the machined workpiece with the flat surface remaining after the removing the portion of the error components. Figure 4-10(b) shows the separated error component. Figure 4-10(c) shows the cut section view of the errors within the separated surface. Figure 4-10(d) shows the 2D sketch of the error components. The waviness (red curve) and the fitted form of the error surface (green curve) can be identified in this view. A further magnification of the section view reveals the small amplitude, high frequency surface undulations which are predominant in deteriorating the surface roughness of the final workpiece. The surface appears to be smooth under normal vision and high magnification system is required to visualize this error in the actual workpiece. The error surface shows a clear difference from the lay mark due to tool feed since the former appears in a random fashion with varying magnitude while the latter is more periodic with concentric ring formation. So to achieve a good surface integrity, elimination of these error components is a mandate.

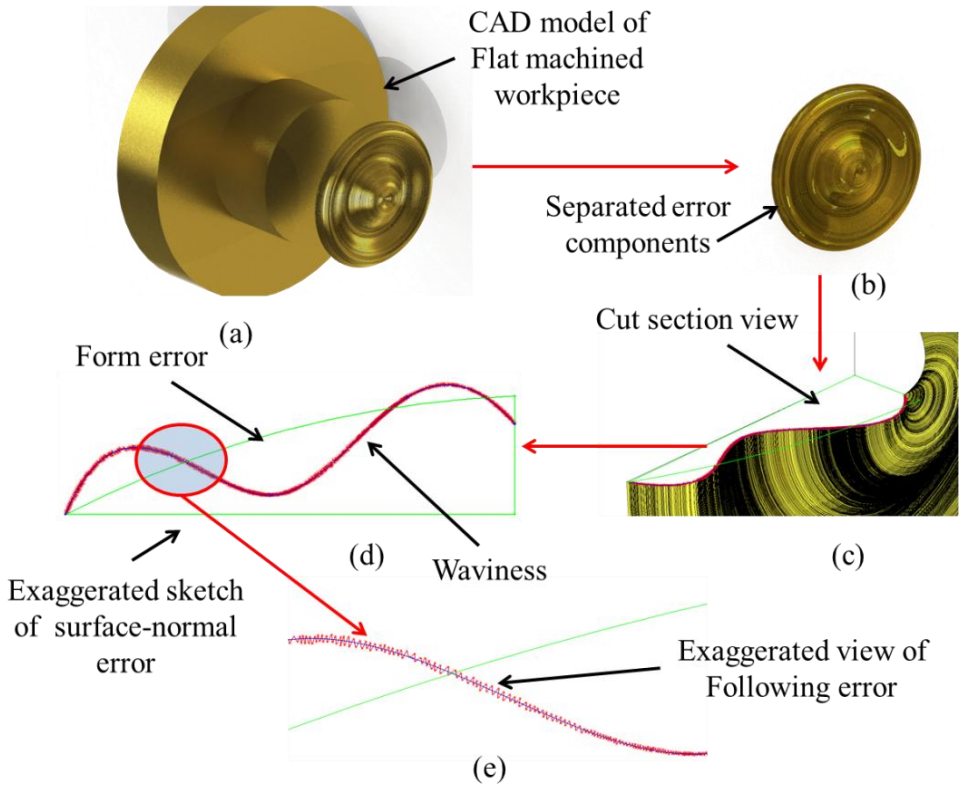

Figure 4-10: Components of errors during a Flat facing operation in a DTM

4.5 Chapter Summary

In this chapter, the description of the DTM was presented. The overall machine and its components of the ultra-precision machine such as mechanical design aspects, electrical components, feedback sensors, machine controller, and corresponding software have been explained. The machines' performance is studied based on the metrological experiments were conducted and the results are presented. The geometric and kinematic following error are explained with their possible causes. An explanation on the various components of surface-normal errors during a facing process in DTM is presented with a detailed schematic. The measurement data provides an

insight that effect of surface-normal error on the surface integrity of the machined workpiece. Since the error components are uni-directional (along Z-axis axial direction) during facing operation, in the subsequent chapter, the development of single axis Fine tool servo (FiTS) system to compensate the systematic and the random errors of DTM in real-time. The further focus of the thesis will be in the development of the FiTS system and their implementation in a dual-servo error compensation mechanism.

Chapter 5 Design and Implementation of Single Axis Dual Servo Mechanism

5.1 Introduction

In this chapter, the development of single axis FiTS system is presented. The mechanical structure, analytical analysis and the performance of the system is studied prior to the implementation in the real-time error compensation. The dual servo concept and integration of the FiTS system control with the machine controller is explained in detail. The effectiveness of the FiTS system is validated by measurement and machining experiments.

5.2 Design objectives and constraints

The purpose of the single axis FiTS is to provide precise tool positioning along the tool cutting direction and high mechanical stiffness along all other directions so as to reduce static deflection during machining. The design is meant to withstand the cutting forces and have a natural frequency higher than the operating frequency during machining, so that the cutting forces do not excite the modes of the system. The design must satisfy several constraints such as, perfect rectilinear motion and high positioning resolution of the tool to compensate the small amplitude errors, the design envelope to withstand the harsh industrial environment, the mechanical properties and system operation with minimal interface requirement to achieve the active real-time error compensation. Also, the total stroke must be large enough to compensate the machines' error components, thus a value of 20

microns high-voltage PEA (HVPZT) is chosen. Ideally the design should be symmetric to avoid moments within the structure and thermal expansion of the system. The actuator must allow for easy exchange of standard tools depending on the process (facing, contouring, turning, etc.). Also, the tool tip should be adjustable to allow for alignment along the spindle centre axis to avoid undesirable tool-offset effects.

5.3 Single axis FiTS Mechanism

The single axis flexure mechanism is developed to compensate the geometric and the kinematic error of the DTM. The FiTS mechanism consists of three major components a) Mechanical guiding unit with tool-holder assembly, b) PEA, and c) corresponding controller unit. The design of the FiTS mechanism plays a vital role in order to achieve the design objectives. Though the actuator and its corresponding control unit are bought-out, the selection of the right actuator-controller system is equally vital to achieve the necessary performance characteristics of the FiTS system.

5.3.1 FiTS Guiding Mechanism

From the literature review, it is found that the double parallelogram flexure mechanisms are conventionally used for the perfect rectilinear mechanisms. Since one of the design criteria is to provide perfect rectilinear motion, the development of the FiTS systems is carried out using double-parallelogram as the building block. A new double parallelogram building block called “Inverted double parallelogram” module is introduced in this study and it is compared with the conventional design.

5.3.2 Inverted Double Parallelogram Module

An inverted parallelogram is originated from the double parallelogram. Figure 5-1(a) and (b) shows a double parallelogram and inverted double parallelogram, respectively.

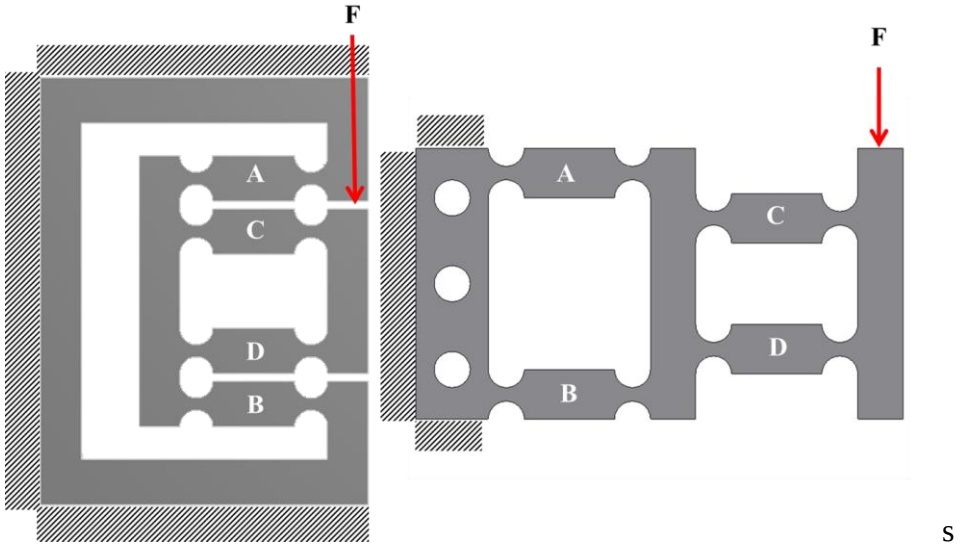

s

Figure 5-1: (a) Double Parallelogram (b) Inverted Double Parallelogram

The flexure hinge pairs connected by a rigid member are marked as A-D where A-B represents the outer parallelogram and C-D constitutes the inner parallelogram which is identical in size and location to A-B. The overall dimension of the module is compact. In the inverted double parallelogram, instead of the inner pair C-D identical to the A-B's location, they are inverted outwards as shown in Figure 5-1 (b) and hence the overall length of the module increases. A FEM analysis study was conducted on the two modules and it is found that the displacement and stress characteristics are similar to each other. Parasitic error motion, which is considered to be negligible in double parallelogram module, has to be considered in our application since its effect could play a role in final performance of the FiTS system. From the FEM results it is found that the inverted double parallelogram design shows a

drastically reduced error compared to the conventional double parallelogram design. For a maximum output displacement of 145 µm, an error value of 65 nm has been evaluated. This error is only 0.04 times the error value (1.54 µm) attained by the conventional double parallelogram design for the same output displacement. And for lesser displacements, as in the case of the nanometer level displacements required by the FiTS systems, the error value is around 0.005 times obtained by the conventional design.

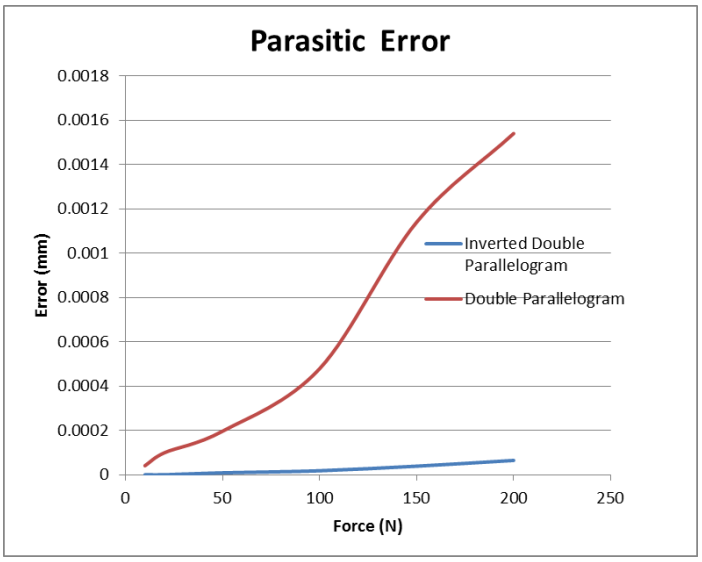

Figure 5-2: FEM data plot for parasitic error between conventional and inverted parallelogram design for given input force

The increase in the parasitic error between the two designs is caused due to the change in the moments between the inner and outer pairs of parallelogram. In the conventional design, the directions of motion of the two pairs are opposite (as seen in the Figure 5-2 (a)). Due to this opposite moment of different magnitude, the primary stage experiences a motion along X direction. But on the contrary, the new inverted double parallelogram design provides a displacement in which all the 4 pairs displace in the same direction leading to a stiffer motion along x direction (Figure 5-2 (b)). Since the length of the design is increased, though the system is stiffer, the end output

displacement is not compromised. So the inverted double parallelogram module is used in the design of FiTS system.

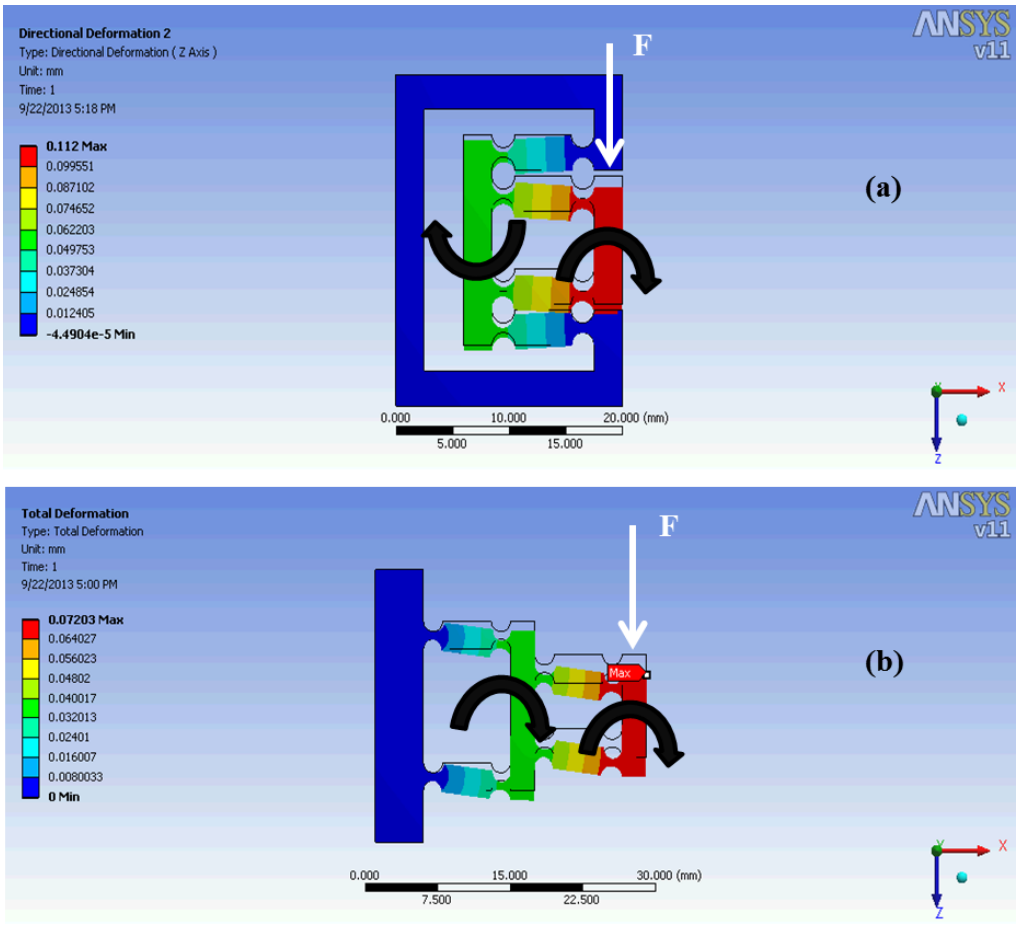

Figure 5-3: FEM screenshot of conventional double parallelogram and inverted double parallelogram

5.3.3 Mechanical Design Description

The design of single axis FiTS system is realized based on the outcome of the various flexure hinge parameters studies conducted in Chapter 3. The design consists of systematically and symmetrically placed circular notch flexure hinge building blocks (inverted double parallelogram) in order to provide the desired one dimensional motion. The circular notch hinges are used in the design due to their immunity to parasitic forces because of its relatively high off-axis stiffness. Figure 5-1 shows the CAD model of the

designed FiTS assembly. The detail drawing of the FTS design can be obtained in Appendix B.

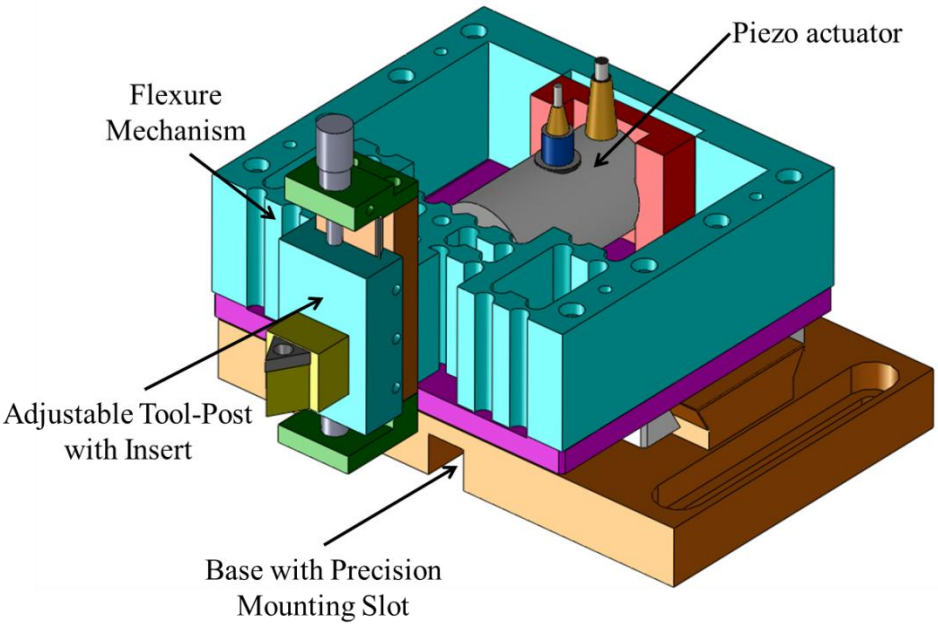

Figure 5-4: Flexure mechanism with PZT actuator and Tool-post assembly

The FiTS system consists of the flexure guiding mechanism with provision to assemble the PEA, adjustable tool holder to align the tool-tip with the spindle center and a base plate to mount the FiTS system on to the machine axis. The flexure guiding unit is designed in such a way that the notch hinges act as a spring system. The accuracy of the FiTS depends primarily on the accuracy of the hinge location. This flexibility makes the manufacturing of flexure mechanism easier and thus reducing its overall cost. The new design of the flexure mechanism has sixteen notch hinges as shown in Figure 5-5. The appropriate stiffness of the system is dependent on the summation of the notch hinge's stiffness. Since the contact between the PEA and the guiding unit is devoid of any mechanical fastening, the forward and reverse actuation of the FiTS is of concern for realizing the necessary motion profile. The main advantage of flexure hinges are their ability to work on the

principle of strain energy. So proper pre-loading of the actuator and the guiding system plays a critical role in the performance of the FiTS. With the proper pre-loading, the constant contact between the actuator and the guiding unit can be realized during the operation of the FiTS. This helps to prevent any lost-motion between the actuator and the guiding unit. Also the pre-loading increases the stiffness in the actuator due to which there is a loss in the travel range of the actuator for the given voltage input.

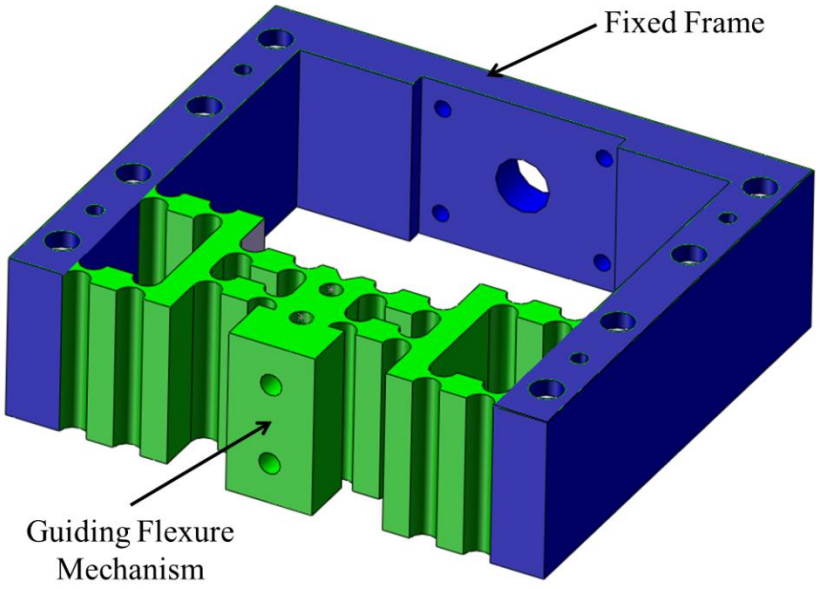

Figure 5-5: Guiding unit with indication of moving and fixed section

5.3.3.1 Pre-loading Mechanism

In the mechanism assembly care has been taken to provide the necessary preloading to the actuator and maintain perpendicularity between the actuator and the guiding unit. The preload assembly consists of a guiding block, lock screw, preload screw and 4 guiding screws as shown in Figure 5-6. The PEA is pre-assembled to a guiding block surface using the lock screw and aligned with its back and side locating surfaces. The pre-assembly is mounted on to the guiding slot fabricated as an integral part in the flexure mechanism to provide locating exactness. The 4 guiding screws provide the required holding

force to retain the guiding block into the guiding slot and the main preloading screw provides the necessary load in order to provide a constant contact between the PEA and the flexure mechanism at all times. The V-groove provided in the moving flexure region retains the PEA tip from slipping during the pre-loading and avoids rotation of the actuator during operation. After providing the necessary preload, the 4 guiding screws are fastened to keep the Piezo-guiding block assembly intact as shown in Figure 5-7.

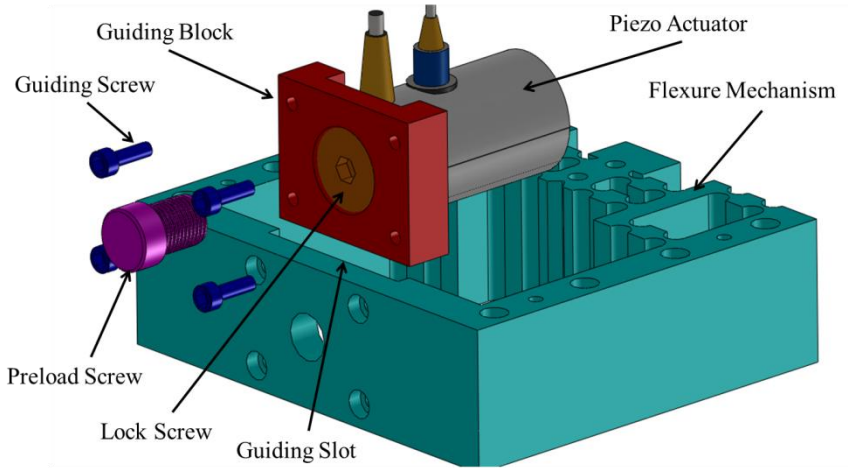

Figure 5-6: Exploded view of the preload mechanism assembly components

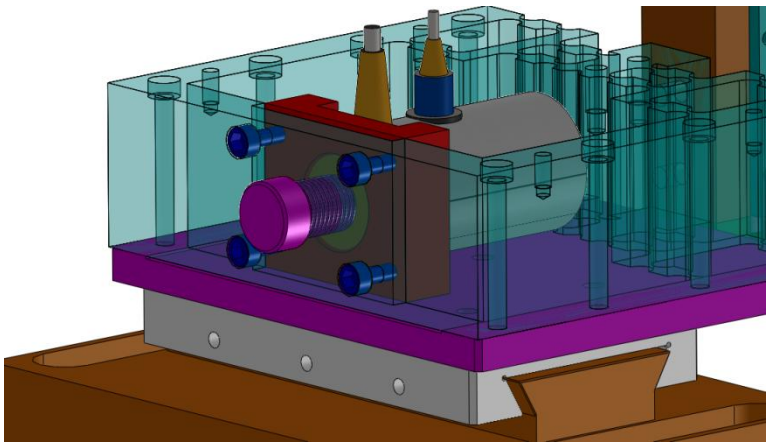

Figure 5-7: Preload mechanism assembly

5.3.4 Piezo actuator and controller selection

PEA with a travel of 20 µm is selected for the current research. The high voltage PEA provides a high mechanical stiffness to with stand the any

impact force and the corresponding amplifier is selected to provide the necessary 0-1000V amplified input to the PZT actuator. The actuator is equipped with an integrated strain gauge sensor which form the feedback to the servo controller module provided along with the amplifier chassis. They provide sub-millisecond response and sub-nanometer resolution which are crucial factors in deciding the performance of the FiTS system. The optional ball tip in the actuator is intended to decouple torque and off-center forces from the translator.

The amplifier has 3-channels to actuate 3 PEA with closed-loop servo control. The PEAs are calibrated with each channel and closed-loop performance of the PEA is tuned with proper gain before dispatching from the factory. The frequency of operation of the PEA with the selected amplifier is around 150 Hz for full range operation of the PEA (20 µm). Table 5-1 shows the specification of the PEA.

Table 5-1: Specification of PEA used in this study

Type	Stack type piezo-ceramic with stainless steel case
Sensor type	Integrated Strain Gauge Sensor (SGS)
Travel Range	20 µm
Stiffness	250 N/µm
Push Force	4500 N
Size	Ø 25 x 48.6mm

5.4 Analytical Modelling of the guiding unit

An analytical model of the guiding unit was developed to predict the static stiffness of the flexure hinges in the radial direction for a range of hinge

parameters (radius and thickness). Figure 5-8 (a)presents the approximated model of the guiding unit considering the flexibilities of the circular hinges, (b) the linear spring model where each flexure is modeled as an equivalent linear spring K_x^i and (c) the equivalent radial stiffness K_x of the FiTS, which is the sum of the equivalent linear stiffness for each flexure acting in parallel. The system is considered rigid except for the flexure hinge rotational (K_B) and axial (K_A) flexibilities which are given by Equations 2-1 and 5-6. The equivalent radial stiffness for a single flexure is determined by adding the effective linear stiffness due to hinge bending in the direction of the motion of FiTS, $K_{x,B}$, and stretching in the axial direction of motion, $K_{x,A}$, as shown in Figure 5-9. The values $K_{x,B}$, and $K_{x,A}$ are determined by equating the potential energy of the displaced system to the external work done by a force F , acting at the center-line of the structure in the radial direction, deforming the guiding unit by a distance x . The motion is restricted to radial direction and hence it can be modeled as system with roller support which helps in single degree motion and constrained in the axial direction.

Flexure mechanisms incorporated in the FTS/FiTS systems are generally built using rigid flexure hinges made out of monolithic metal blocks to with stand the machining and actuation forces. They operate well within their linear elastic limit. So the nonlinearity is insignificant for transverse displacements lesser than 0.1L [99-101]. Typically in any material non-linearity can be neglected if the motion range insignificantly low compared to the length of the displacement arm [2].

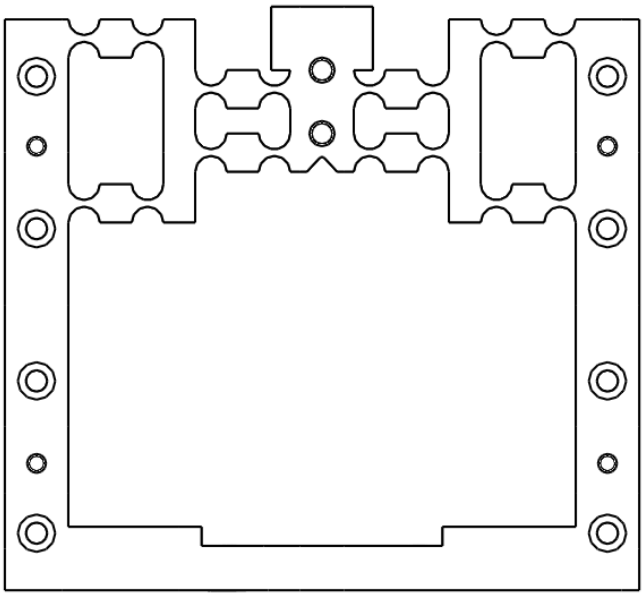

Figure 5-8: Schematic of One dimensional Flexure mechanism

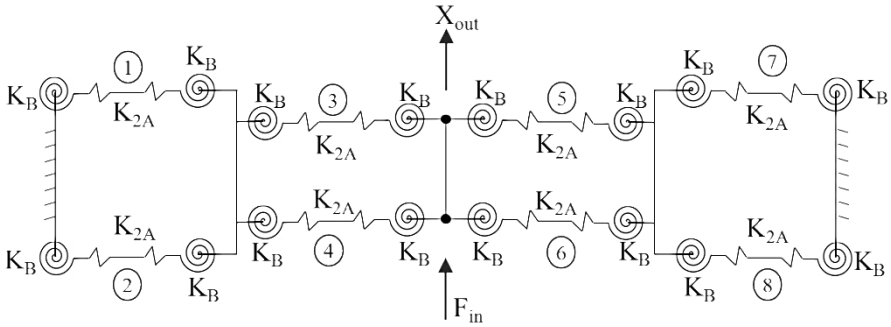

Figure 5-9: Approximate spring model of the guiding mechanism

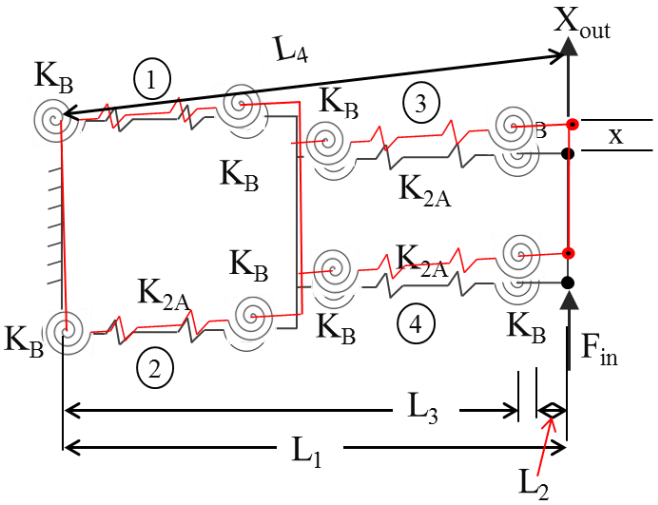

Figure 5-10: Deformed and Undeformed position of the symmetric half of the developed FiTS model

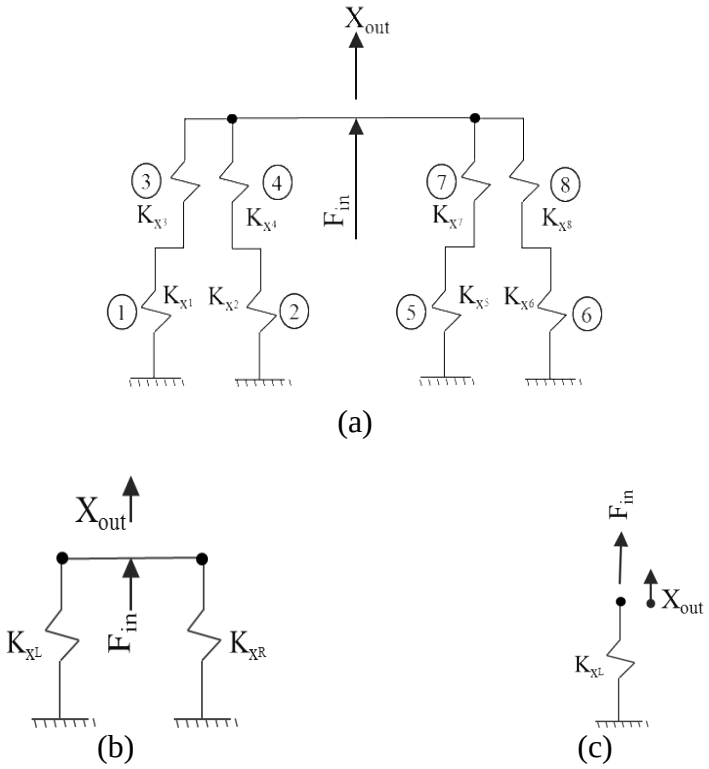

Figure 5-11: Resultant stiffness of the single axis FiTS mechanism

Figure 5-10 shows the actual and the deformed position of the guiding unit. The length L_1 to L_4 represents the length of the flexure hinge location before and after the deformation. Considering the PEA and flexure assembly to be connected in serial, the effective stroke achieved by the flexure mechanism is a tradeoff between the combined stiffness of the flexure mechanism and the PEA. The minimum stroke length of the PEA is given by,

$$\Delta x = \Delta L_0 \left(\frac{K_{pzt}}{K_{pzt} + K_x} \right) \tag{5-1}$$

where, Δx is the effective stroke length of the FiTS (µm) considering the total stiffness of the guiding unit and the PEA, ΔL_o is the nominal stroke length of the PEA is 16 µm in closed loop operation, K_{pzt} is the PEA stiffness (250 N/micron), and K_x is the stiffness of guiding unit.

So to compute the stiffness K_x, consider the Figure 5-11 (a) which is equivalent spring stiffness combining the radial and axial components. Since the hinges 1-2 and 3-4 are connected in parallel and hinges 1-3 and 2-4 are connected in series, so the axial $K_{x,FA}$ and bending stiffness $K_{x,FB}$ of one half of the FiTS mechanism is given by,

$$K_{x,FB} = \frac{2K_B}{(L_1 - L_2)^2} \tag{5-2}$$

$$K_{x,FA} = K_A\left(1 - \frac{L_3}{\sqrt{x^2 + {L_3}^2}}\right) \tag{5-3}$$

The K_x^i, total stiffness of the i^{th} hinge pair of the guiding unit is given by,

$$K_x^i = K_{x,FB} + K_{x,FA} = \frac{2K_B}{(L_1 - L_2)^2} + K_A\left(1 - \frac{L_3}{\sqrt{x^2 + {L_3}^2}}\right) \tag{5-4}$$

Hence the total stiffness of the single axis FiTS is given by the equation 5-5.

$$K_x = \frac{16\,K_B}{(L_1 - L_2)^2} + 8\,K_A\left(1 - \frac{L^*}{\sqrt{x^2 + L^{*2}}}\right) \tag{5-5}$$

where, $L^* = L_3$, K_B is the bending stiffness given by eqn. 2-1, and K_A is the axial stiffness given by,

$$K_A = \frac{Eb}{\left(\pi\left(\frac{r}{t}\right)^{\frac{1}{2}} - 2.57\right)} \tag{5-6}$$

From the graph Figure 5-12 based on the equation 5-4, the effective stiffness of the FiTS unit is 4.943 N/µm. Hence the effective stroke, Δx of the FiTS unit based on equation 5-1 is 15.68 µm.

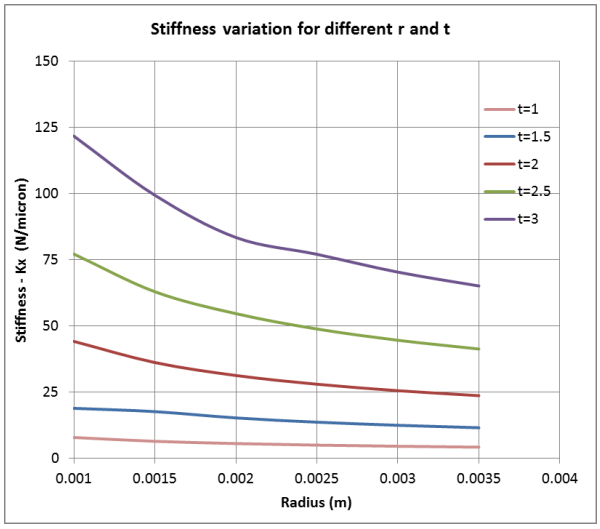

Figure 5-12: Stiffness K_x variation based on analytical model for various hinge *"r"* and thickness *"t"*

5.4.1 Mobility analysis

Another analysis to identify the degree of freedom of the complaint mechanism is to use the mobility analysis in which the compliant mechanism is considered as its rigid body counterpart. Expression for planar mobility of a planar mechanism with only three degree of freedom [102] is as follows:

$$M_3 = 3(n-1) - \sum_{i=1}^{j} c_i \tag{5-7}$$

Where n is the number of links, j is the number of joints, f_i is the number of freedom of the joint i, c_i is the corresponding constraints (3-f_i)

$$M_3 = 3(n-j-1) + \sum_{i=1}^{j} f_i \tag{5-8}$$

Grubler's equation for a single degree of freedom joints (notch hinge) is simplified to,

$$M = 3(n-1) - 2j \tag{5-9}$$

For the designed flexure mechanism with single D.O.F. notch flexure hinge the mobility is found to be 1 which satisfies the condition for single D.O.F motion of the mechanism with the number of links n = 12, number of joints j = 16. The links and joints also satisfies the condition for single D.O.F (**M=1**)

$$j = \frac{3n}{2} - 2$$

5.4.2 Finite Element Analysis of the guiding mechanism

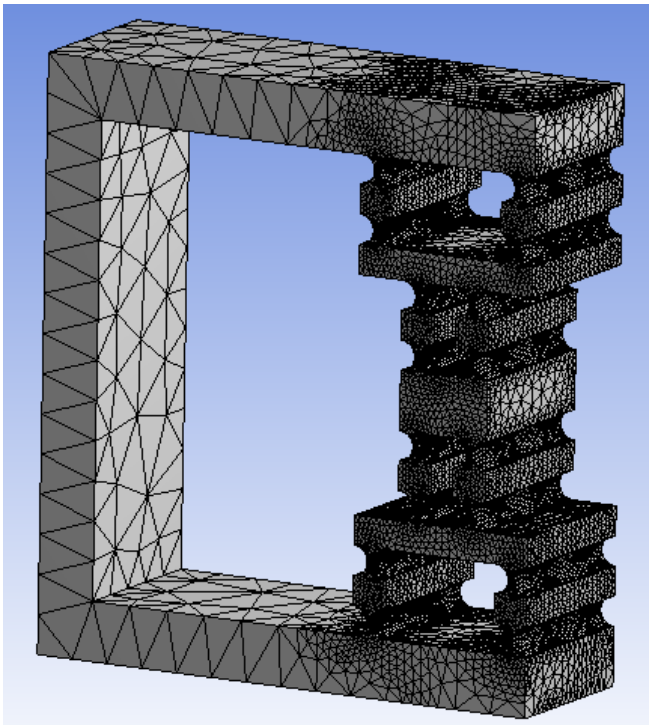

Figure 5-13: Finite element model with refinement to hinge region

In order to find the modes of operation of the guiding mechanism, commercial FEM software was used. The flexure hinges, where the stress concentration is higher is given special attention in the FEM. All the 16 hinge regions are refined to 3 levels with the proximity and curvature option using the contact sizing method to generate equal and finer mesh along the hinge region (Figure 5-13). The following Table 5-1shows the six modes and their corresponding frequency. The first mode frequency is 1.58 KHz which is well away from the operating frequency of the FiTS system which is around 150 Hz. The Figure 5-14 shows the different modes and their corresponding displacement characteristics.

Table 5-1: Modal Analysis frequencies

Mode	Frequency (Hz)
1	1579.3
2	2966
3	4216.1
4	7891.4
5	8880.8
6	9427.8

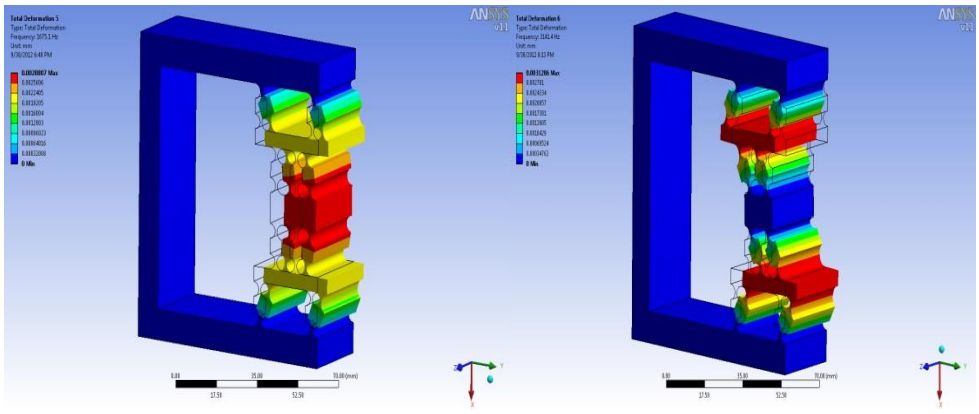

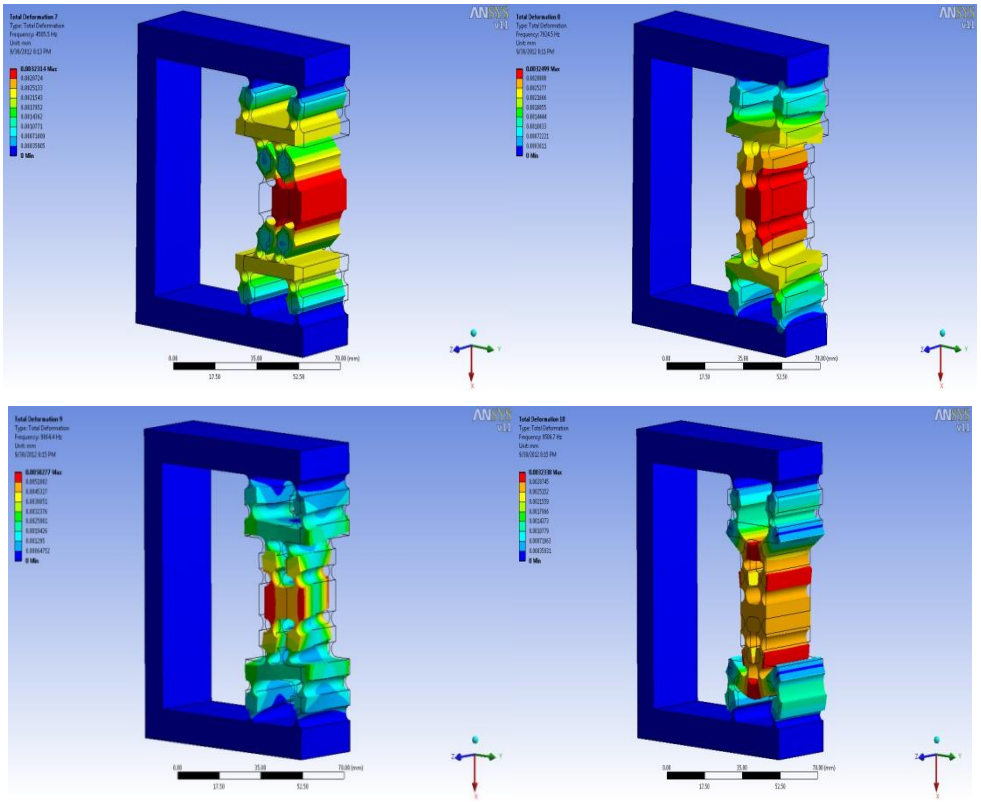

Figure 5-14: Modal analysis of single axis FiTS guiding unit (6-Mode)

5.5 Fabrication

The overall mechanism is fabricated as a monolithic structure using the wire-cut electrical-discharge machining (EDM) technique. The advantage of wire-cut is its higher dimensional accuracy and the feasibility to fabricate intricate designs in a single set-up which improves the dimensional tolerance. Since flexure hinges can be fabricated by drilling holes with small spacing, it is common practice to use the wire-cut EDM. Considering shape changes and residual stresses caused by the machining process, wire EDM is often used to obtain an accurate hinge profile [86]. The reference region where the pre-loading block will be located is also integrated in the monolithic design, which helps in aligning the guiding unit and the PEA axis which otherwise is a critical task and would give way to tangential shear force acting on to the actuator tip.

5.6 Mechanical Calibration

In this section, the actual testing and study on the performance of the developed FiTS system is presented. The static displacement, force characteristics and the open and closed loop performance of the system are presented. The development of software to automate the calibration process is also presented.

5.6.1 Flexure Stage Calibration

The developed FiTS system is calibrated by varying the input voltage to the PZT actuator and measuring the output tool-holder end displacement using the high resolution capacitance sensor. In order to apply the input voltage and record the output displacement as a function of sensors' output voltage, a DAQ unit with 16/4 I/O was used. Labview code (Appendix C) was written to generate the time dependent waveforms and store the output data from the corresponding sensor (CAP/Force sensor). The schematic of the calibration system is shown in Figure 5-15 and the photograph of the actual set-up is shown in Figure 5-16. The voltage versus displacement for both loading and unloading conditions is plotted in the Figure 5-17. From the results it is evident that the inherent hysteresis effect of the PEA is eliminated by using the auxiliary PEA servo controller. The maximum displacement achieved for an input of 10V to the PEA is 14.1µm. The performance of the flexure stage with auxiliary PZT servo controller is studied using the step motion pattern (section 5.6.3) to identify the accuracy and the repeatability of the system.

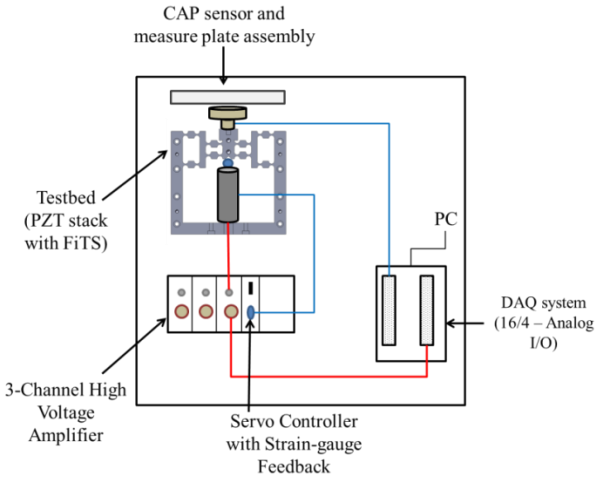

Figure 5-15: Schematics of developed FiTS system calibration

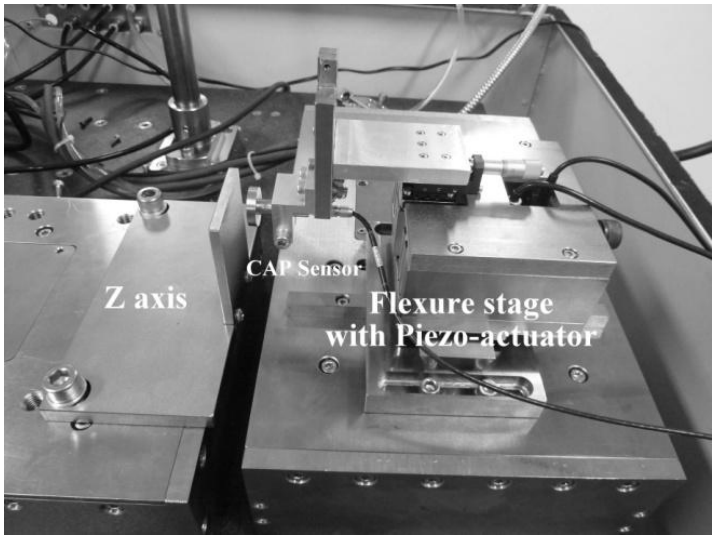

Figure 5-16: Developed single axis FiTS with CAP sensor assembly

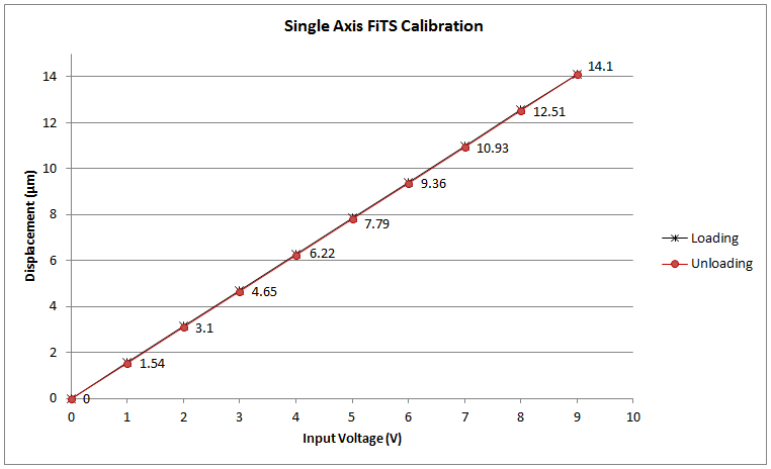

Figure 5-17: Displacement Characteristics of single axis FiTS system for input voltage

5.6.2 Static testing

Generally, the force generated from a spring-model can be expressed as a function of constant multiplied by the displacement of the stretched spring, F = *k z*, where *z* is the displacement of the spring for the FTS. Hence, the static testing was carried out by loading and unloading guiding structure. Then, the displacement for loading and unloading was detected by the capacitance gauge and recorded. The value of K_{FiTS} is theoretically defined from the gradient of the plotted graph, and the governing equations are shown as:

$$K_{FiTS} = \frac{K_{loading} + K_{Unloading}}{2}$$

From the graph (Figure 5-18), the resultant stiffness of the developed FiTS is the average of the stiffness while loading and unloading. The slope of the curve represents the stiffness of the system and it is found to be 3.758 N/μm (K_{FiTS}). This measured force value matches closely with the analytical study after considering for deviation of sensitivity of the force sensor (±15%) of the total output and the manufacturing errors which are critical in the performance characterization of flexure hinges.

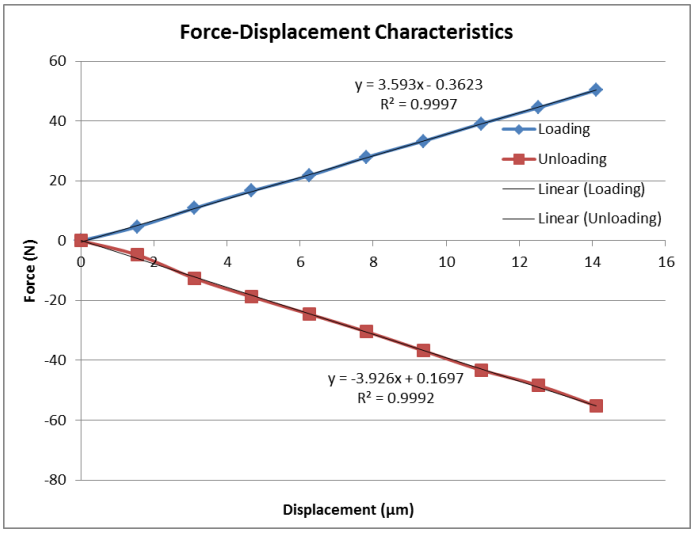

Figure 5-18: Force-Displacement characteristics of single axis FiTS system

5.6.3 Performance Characteristics

5.6.3.1 Open-loop Performance Study

The open-loop performance of the developed FiTS system with the PEA's servo controller not activated. The measured and simulation result of the open loop response of the FiTS is presented Figure 5-19. The response is the result of a unit step voltage input of 1 volt. The desired response is not achieved and the system took around 800 ms to settle. These characteristics of the system performance will not suffice the need to compensate the high frequency following error. Also the main issue faced with the open loop system is that inherent hysteresis of the PEA, which in turn deteriorates the performance of the FiTS system. So the lag in the response of the FiTS system due to the PEA clearly depicts an auxiliary servo is necessary to achieve the required performance characteristics.

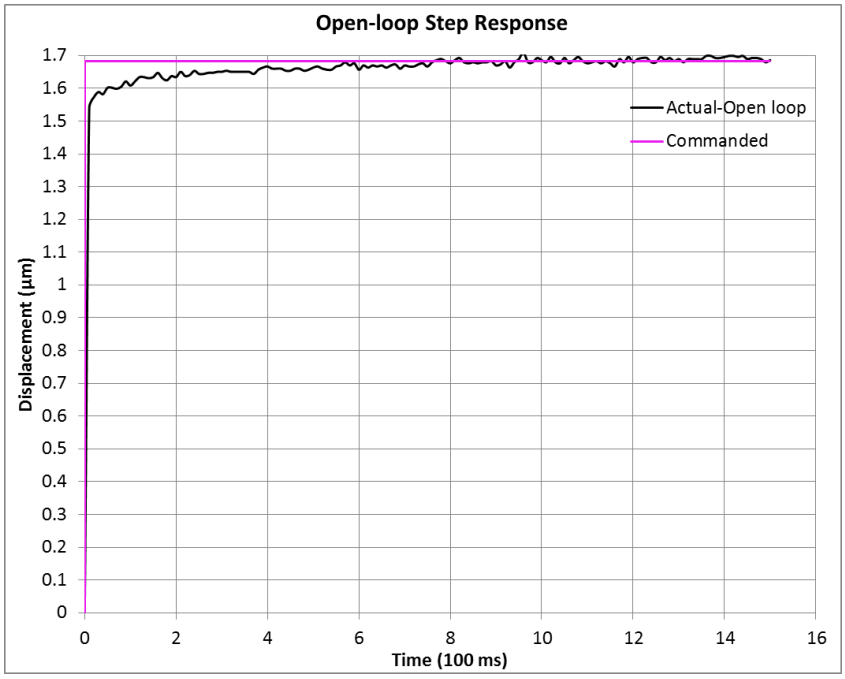

Figure 5-19: Single step-response of open-loop FiTS system

5.6.3.2 Closed-Loop Performance Study

The measured and simulation result of the closed loop response of the stair-case step input to the FiTS is presented Figure 5-20. The response is the result of a unit step voltage input of 1 volt. Clearly, the desired response is achieved, as the final value is 14.1 µm and the oscillations and hysteresis associated with the uncontrolled PEA are eliminated. The actuator rise time (60% of commanded value) is 6 ms, and the overshoot is 11.24nm (Figure 5-21) which is less than 0.7095% of the output. The steady state error is 10 nm, which is predominantly due to sensor dynamic noise level and dynamic response of the PEA. The actual closed-loop response shows excellent agreement with the simulated response with a clear demarcation from the open-loop performance. The rise time of the controlled system is twenty five times that of the open loop system. The overshoot of system is limited to 11.24 nm and the settling time 0.02 s. Hence the use of the close-loop system in the

developed FiTS system will yield promising results with actual step following the commanded value during the dual servo compensation

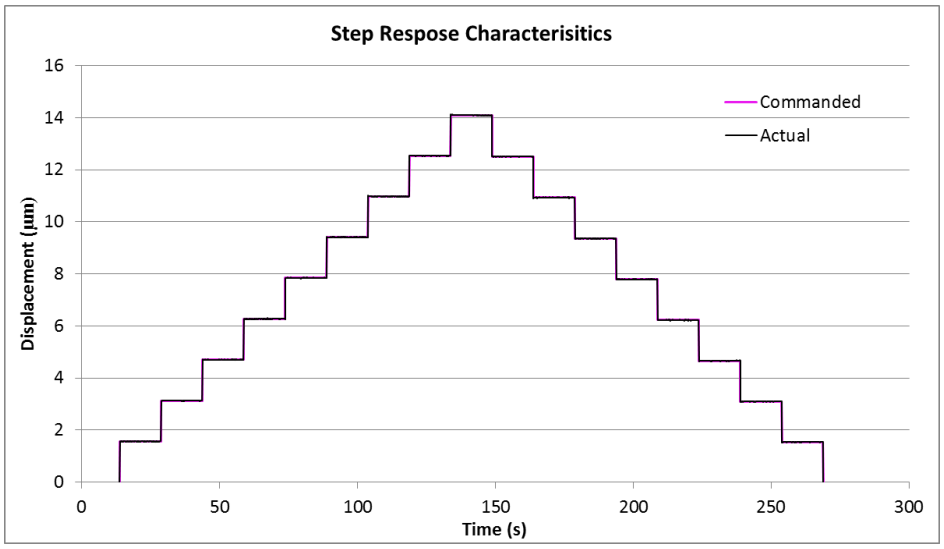

Figure 5-20: Closed-loop stair-case input step response graph for 1 V input

Figure 5-21: Single step-response of Closed-loop FiTS system

5.7 Dual Servo Principle

From the literature review, it is clear that the real-time compensation facilitates in the compensation of both systematic and random errors. In most of the previous works, a secondary sensor is used apart from the machines'

feedback sensor. This method is difficult to implement on to an existing machine tool since the machine is designed with its own feedback and control units and mounting of additional feedback units will be difficult. Alignment of the secondary sensor, measurement location and integration of the sensor feedback with the controller for compensation increases the complexity of the machine. Also importantly, the error measurement by the secondary sensor will cause a definite delay in the controller before it could compensate for the errors. Even after implementation of the secondary sensor, the machine controller and mechanical components have their own limitation and thus a major improvement in the machines' accuracy cannot be realized using the increased number of sensors and the utilizing the same mechanical unit.

In this section, the implementation of single axis FiTS system for the real-time error compensation in the DTM using dual servo principle is presented. Figure 5-22 shows the schematic representation of the dual-servo concept. The dual servo consists of a machine servo and an auxiliary servo. The auxiliary servo works in synchronize with the machine servo, to achieve finer compensation of the residual error in the machines' servo. The main advantage of this concept is that the need for the secondary sensor is eliminated and the auxiliary servo operates with the residual error of the machine servo as its input. The green connection in the Figure 5-22 forms the bridge between the machine controller and the auxiliary servo. The computed residual following error of the machine is sent as the input to the auxiliary servo. The input is further amplified by the high-voltage PZT amplifier and applied to the single axis FiTS mechanism.

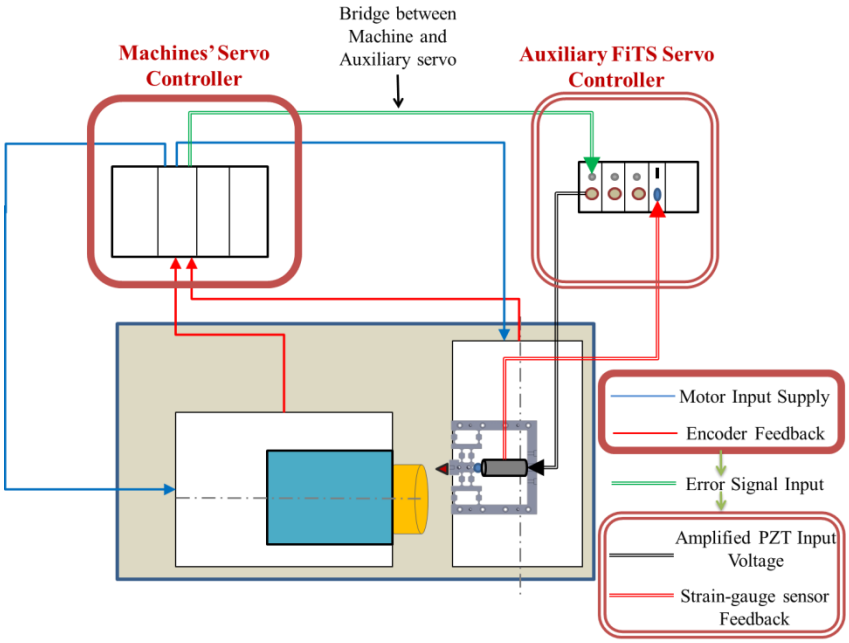

Figure 5-22: Schematic of Dual-servo concept

Figure 5-23 shows the complete control-loop of the dual servo mechanism with geometric and kinematic error compensation. The input (G-code) to the controller is converted as encoder counts (1cts = 5nm) and the feedback is read in real-time. A comparison between the actual and commanded position is computed and sent to the motor amplifier to correct the axis position to the desired position. Both the pre-calibrated compensation data such as the linear axis positional compensation table from the laser interferometer experiments and the real-time positional data from feedback sensor are compensated by the machines' controller.

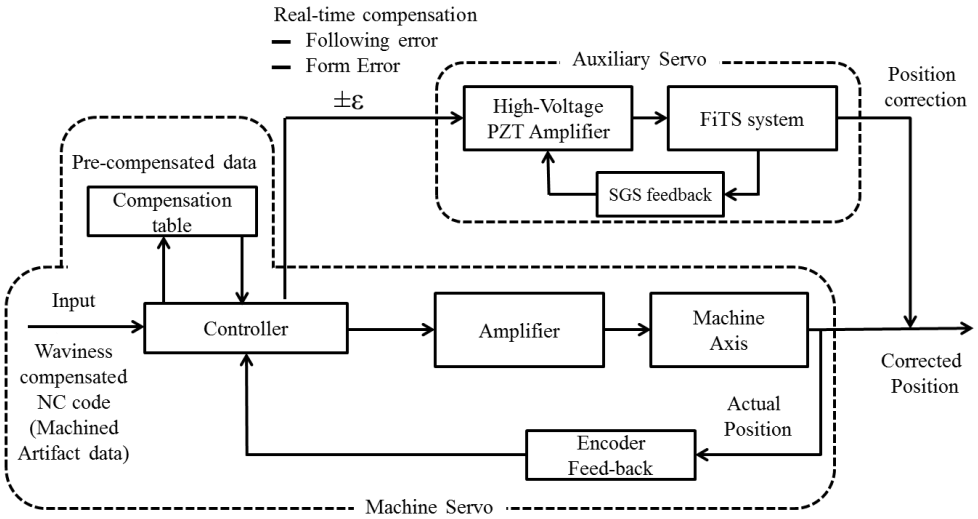

Figure 5-23: Schematic of control-loop of dual-servo concept

Using the auxiliary servo, the real-time error data from the machines' controller such as the following error and the axis form error measured previously is sent as the input to the auxiliary servo as corresponding voltage based on the FiTS system calibration data. The high-voltageamplifier amplifies the voltage as required by the PEA. This auxiliary servo is closed by the PEAs' in-built strain gauge sensor whose voltage corresponds to the actual extension of the piezo crystal. Since proper pre-loading is provided by both mechanically and by the PEA servo controller, there is no evidence of loss-motion and stress-stiffening effects in the FiTS mechanism. By this method of real-time error compensation, an effective enhancement of the machine tools accuracy can be achieved.

5.7.1 Synchronization of the dual-servo

For the effective operation of the dual-servo concept, a strategy was applied in the actuation of the FiTS system. The Figure 5-24 shows the flowchart of the compensation strategy followed in the dual-servo mechanism. Since the limitation of the FiTS system is its output displacement, the error

lesser than 5 µm are effectively compensated by the FiTS system and any error value higher than this is compensated by the machines' servo axis.

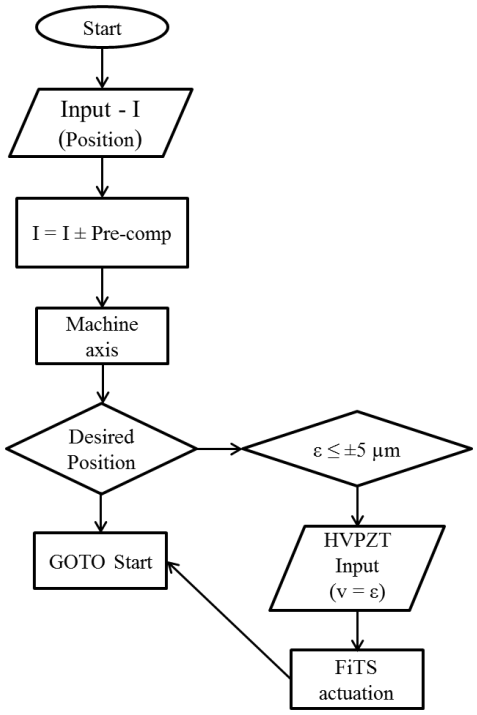

Figure 5-24: Flowchart of the Dual-servo procedure

The synchronization of the machines' servo and the auxiliary servo plays a critical role in the implementation of the FiTS system. The main limitation of the machine axis is their response to compensate finer motion and that of the FiTS system is its achievable output displacement. So both these short-falls are overcome by limiting the machines' axis to compensate coarser errors and FiTS is made to compensate finer errors. Typically the value of the FiTS actuation is limited to 5 µm which is 25 times of the measured following errorFigure 4-9. Since the machines' controller output is used as the input to the auxiliary servo, the priority sequence of operation of the machine controller (Figure 5-25) needs to be understood for effective synchronization of the dual servo mechanism. The primary task of the controller is to maintain the phase cycle of the motor in a controller commutated motor scheme. In this

case, the amplifier is used as a “dumb” voltage amplifier rather than acting as a secondary controller.

The second task is to perform the “servo closed-loop cycle” by reading and converting the encoder feedback with the input reference value. Servo cycle’s default value is set as 442 μsec and can be changed by the user depending on the response of the mechanical system (which is end output in our case). Also the servo cycle for each individual motor in the system can be controlled separately using the controller parameter – *Ixx60* (*xx* – motor number). *Ixx60* defines the extension of the servo update time for Motor xx beyond a single servo interrupt period. The servo loop will be closed every (*Ixx60* + 1) servo interrupts. Using this parameter, the servo for a particular axis can be delayed based on the dynamics and/or feedback resolution.

Thirdly, the real-time interrupt (RTI) is used for the synchronization of the multiple coordinate systems (C.S.) of the machine. Another important task of RTI cycle is execution of a special program called PLC0. PLC0 is provided for performing user defined priority tasks. This PLC0 is executed for every interrupt cycle and can be varied according to the controller parameter - *I8*. So using this parameter, the user can perform a real-time task (every single RTI) or a delayed response of (RTI + I8) servo interrupts. This parameter is not motor dependent and it defines the RTI of the whole controller performance.

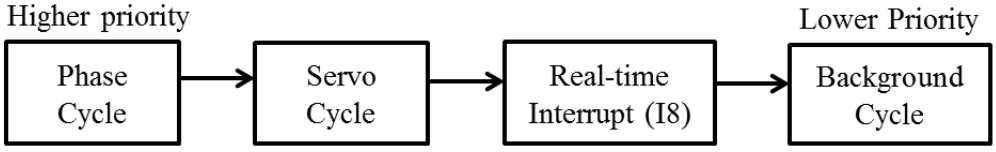

Figure 5-25: Priority of Tasks in Machine Controller

In the following section, the various errors which were described and measured in the previous chapters are studied, a dual-servo algorithm is developed and the results of implementation in measurement and machining experiments are presented.

5.8 Error Compensation mechanism

5.8.1 Following error compensation

The effect of the nanometric following error on machining mirror-finish components is lamentable. In order to explain the effect of following error in the flat-face machining, the schematic of the variation of depth of cut (*d*) is shown in the Figure 5-26. Figure (a) represents change in the depth of cut *d* due to the following error of the Z axis of the DTM and Figure (b) represents the error compensation mechanism to be implemented. Since the controller does not work without a minimal error, there is always a ringing motion of the axis along the reference point. In order to maintain the constant "*d*" throughout the facing operation, the FiTS based dual servo compensation is implemented. The finer error (< 5µm) is compensated in real-time with the auxiliary FiTS system. While the Z-axis produces an error *"-*Δ*d"* in the negative direction and increases the depth of cut by *"d*+Δ*d"* by moving away from the tool-tip. Similarly, the depth of cut is decreased by *"d-*Δ*d"* while the Z-axis produces an error motion in the positive direction. In order to maintain the same depth of cut, a secondary motion by the FiTS should be performed along the error direction to compensate for the change in the depth of cut. The Figure 5-26(b) shows the effective compensation mechanism to maintain the depth of cut to be constant throughout the machining process. As mentioned in

the section 5.7, the synchronization between the two systems is vital. In this study the Z-axis is slowed down by increasing its servo cycle so that the axis does not use the feedback to close the positional loop using the machines' Z-axis. Instead, the FiTS system is actuated using the error value input for every RTI cycle (every servo cycle). By this method, the compensation in real-time is performed by the FiTS system, which is faster and accurate in response due to reduced mass and better performance.

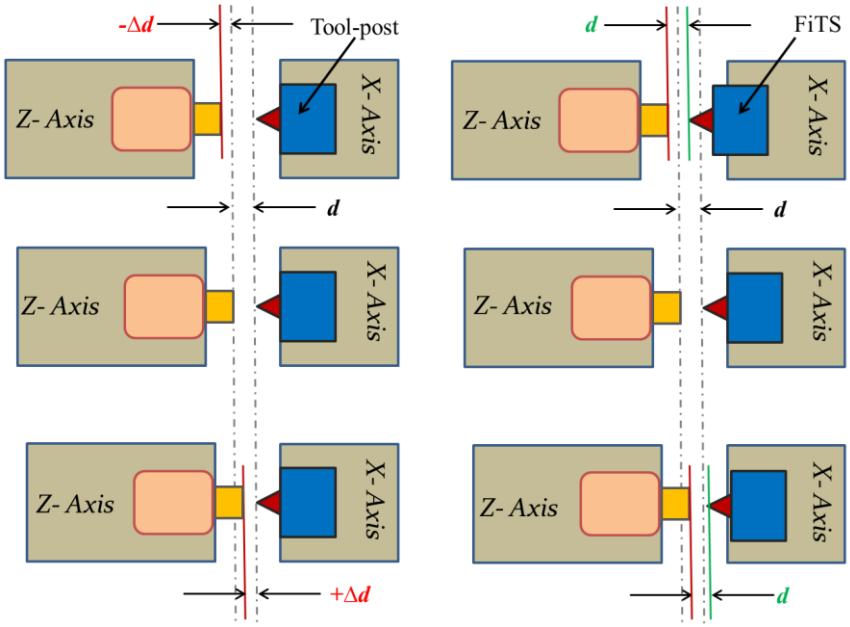

Figure 5-26: (a) FE motion of Z axis (b) FiTS compensation to maintain Depth of cut "*d*"

The code for the PLC0 for the real-time compensation using the developed FiTS system is shown in Figure 5-27. The actual and commanded positions are acquired for every RTI and the command to the HVPZT amplifier is sent through one of the additional amplifier (for voltage output) of machines' controller. PEA forms a closed-loop through its own servo controller. The machine controller sends the command voltage using the proportionate gain value *(Ixx30)*K_p. The K_p value is defined based on the number of machines' controller counts required for producing 0-10V which

corresponds to 0-2^19 counts. Initial voltage of amplitude 5V is applied to the FiTS system, to provide actuation on both forward and backward direction.

```
CLOSE
END GATHER
DELETE GATHER
DELETE TRACE

OPEN PLC 0 CLEAR
P5959=(M261-M262)/3072
If (P5959 < 0)
  AND(P5959>-500)
  P5960= 16385+P5959
  COMMAND"#4J->P5960"
EndIf
If (P5959 > 0)
  AND(P5959<500)
  P5960= 16385-P5959
  COMMAND"#4J->P5960"
EndIf
If (P5959 = 0)
  OR(P5959>500)
  OR(P5959<-500)
  OR(P5959=500)
  OR(P5959=-500)
  P5960= 16385
  COMMAND"#4J->P5960"
EndIf
CLOSE
```

Figure 5-27: PLC0 code for FiTS actuation based on following error

The following error is measured to be around 200 nm at static position when the machine servo alone is activated (Figure 4-9). The Figure 5-28 shows the original and compensated following error of Z-axis. The stage is measured for static following error with and without the compensation mechanism. After the activation of the FiTS based dual servo compensation, the following error is reduced to 20nm. The effect of the compensation is seen clearly in Figure 5-28 where except the intermittent actuators dynamic response (around 10nm) and environmental noise, following error is reduced effectively.

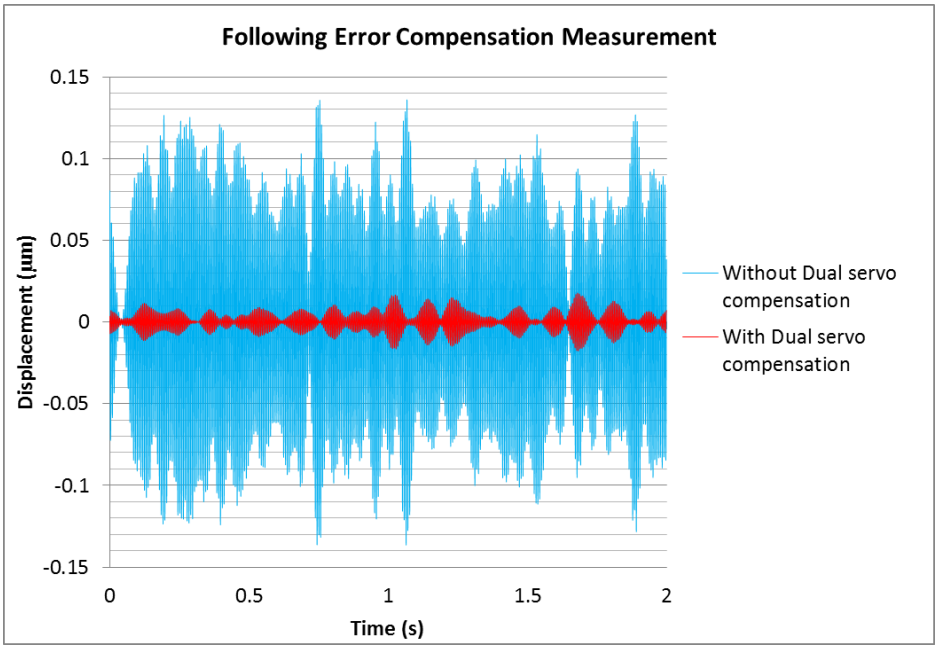

Figure 5-28: Static following error measurement with and without PZT compensation

5.8.2 Form error compensation

In addition to the following error compensation along Z axis, the form of the X axis of the DTM causes the form error in the surface of the machined workpiece. The form of the machine axis is studied by both measurement and machine experiments. To validate the measurement results obtained in section 4.3.1.2, machining experiment is conducted on a brass workpiece. The machined artifacts are measured under the surface profiler to understand the form of the machined surface (Figure 5-29).

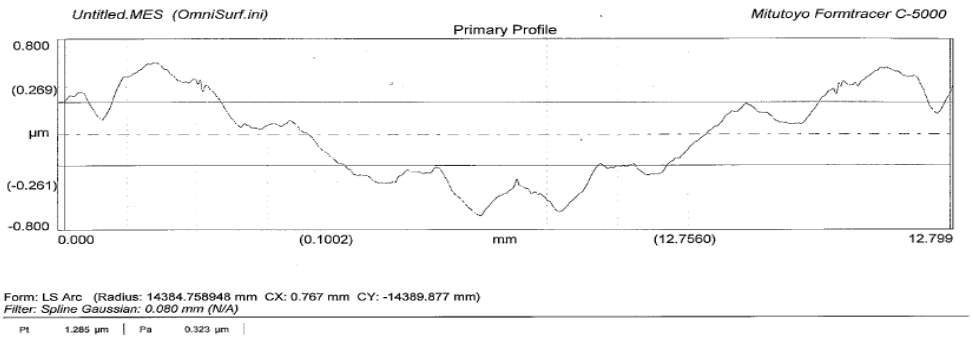

Figure 5-29: Machined profile data

The machined surface replicates the same profile as that of the CAP sensor measured profile between the spindle face and the X-axis (Figure 4-6). A total of measurement of 8 segments have been done in the sample to ensure that there is no major effect of axial error of the spindle on to the workpiece surface. The P_t value of the machined surface is 1.285 µm for the length of 6.5 mm. The result shows that the minor difference in the profile height data between the CAP sensor measurement and the actual machining experiments. Since the CAP sensor is of non-contact type, the error value measure by the sensor corresponds to the real value form error in the X-axis. But from the artifact measurement, the magnitude of form error is reduced due to the "contact damping" created at the tool-workpiece interface. This measured artifact closely matches with the perpendicularity data of 10 µm for the overall 40 mm travel of the X-axis (for 5 mm the error is found to be around 1.5 µm).

In order to compensate the form error, the measured error values are compensated on-line using the auxiliary servo. A PLC logic is developed in order to compute the cumulative effect of both Z-axis following error (Z-axis encoder) and the X-axis form error (Capacitance sensor) along Z axis. Computed error value is fed as corresponding input voltage to the PEA through the machine's controller. This voltage is further amplified at the HVPZT amplifier and actuates the single axis FiTS system to compensate the error along Z-axis. The PLC logic incorporated ensures that the exact error component for each location of X-axis is computed in real-time. Thus the change in federate does not hinder the compensation process.

The raw data recorded using the capacitance sensor is filtered to reduce the low frequency noise and a curve is plotted to fit the filtered data. The data

is used for curve-fitting in order to find the form error of the X axis as shown in Figure 5-30. The equation obtained from this fit curve is a function of X axis location and the corresponding form error. The experiment has been repeated for few times in order to find the repeatability of the measurement value.

This equation is fed to the PLC0 as machines' controller variable to actuate the FiTS system in real-time based on the X-axis position. Since the PZT actuation is a negated Z axis displacement, the equation (5-10) satisfies the compensation motion by the PZT actuated flexure mechanism.

$$z' = 0.3389 + (0.48246 * x) + (-0.00605 * x^2) \quad (5\text{-}10)$$

Where,

z' – PZT displacement value (micron)

x – X axis location captured from machine's controller in real-time (mm)

The equation of the compensation data is stored into the PLC0 of the machine controller (similar to the following error compensation) and the measurements are recorded in order to verify the effect of the compensation using the developed FiTS system. The Figure 5-31 shows the form error and the compensated displacement of the developed FiTS. The error value is reduced drastically to sub-micron level. Though the form is removed completely, there is still the waviness component present in the measured data.

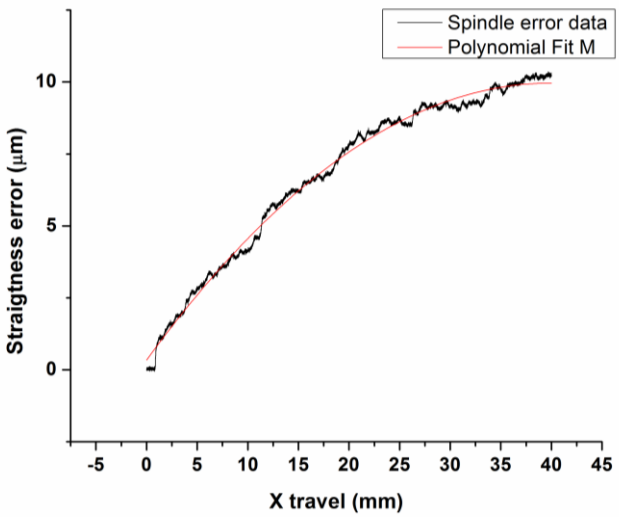

Figure 5-30: CAP sensor assembly for simultaneous X axis straightness with respect spindle

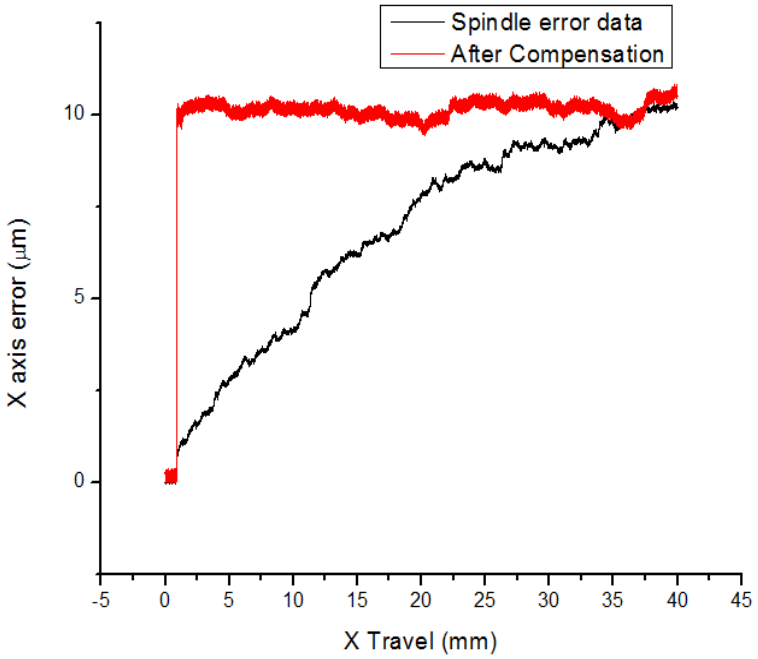

Figure 5-31: CAP sensor measurement with & without error compensation

5.8.3 Waviness Compensation

The waviness is not a repeatable error and machine's feedback sensor does not provide any information about the waviness. An additional sensor is required to capture the waviness of the X-axis but this method will have its own delay in response to compensate the error. Another method is to machine flat surfaces and measure the machined surface for waviness identification.

The measured surface waviness is used as a compensation value and the same is compensated during tool-path generation. In the current research, the waviness of the workpiece is measured using a white light interferometer and the corresponding waviness pattern is compensated using the corrected tool-path in the subsequent machining.

5.9 Machining Performance test

To examine the influences of the errors on the workpiece surface, the geometrical errors of the X-axis translational slide and the kinematic following error of the Z-axis translational slide are compensated. Flat face machining was considered to be the best method to identify the various components error as mentioned in section 4.4. Hence, the governing equation can be derived as:

$$R = R_t \pm \varepsilon$$

where, ε is the cumulative errors caused due to the form, waviness and following error of the machine axes. So for the flat face machining, the following error in Z-axis receives primary attention in terms of the achievable surface roughness since the Z-axis following error forms the surface-normal error component in the machined surface. So the effect of individual and the combined errors are validated experimentally.

5.9.1 Machining Experiments

The actual machining of the workpiece was conducted to understand and compare the surface integrity of the DTM achievable. Figure 5-32 (a) and (b) shows the set-up of the DTM and the close-up view of the single axis FiTS system.

In the machining experiments, three sets of experiments had been performed. Firstly, an experiment with only following error compensation was initiated. In the following error compensation experiments, the surface roughness R_a achieved using the real-time compensation using the following error data from the machines' controller had been studied.

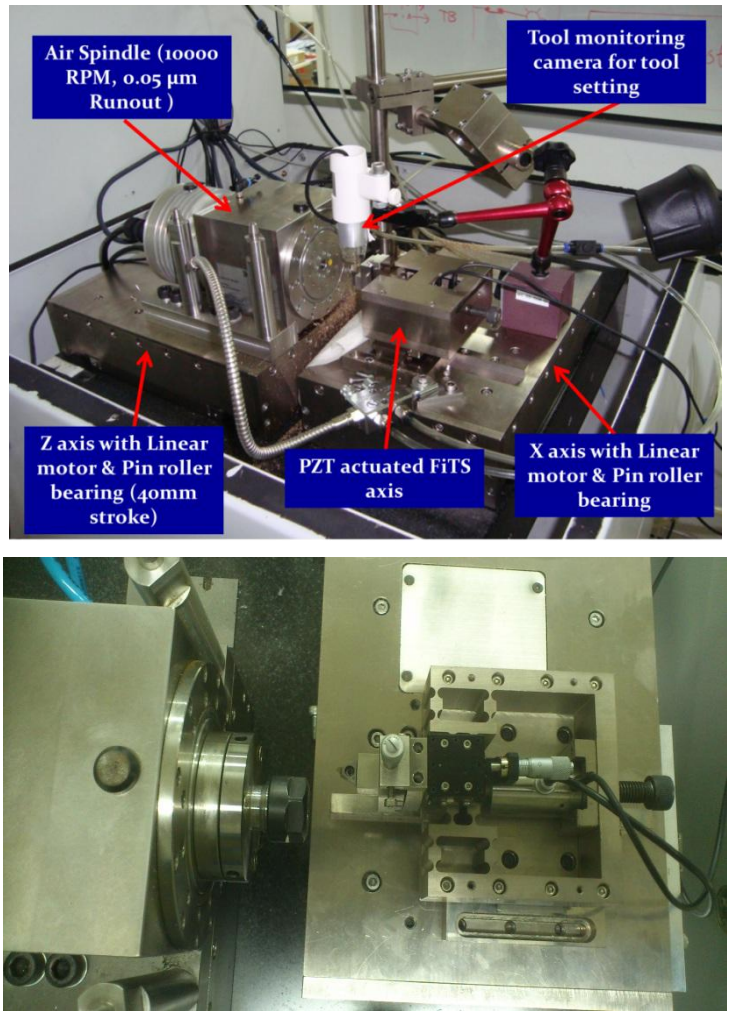

Figure 5-32: Photograph of (a) Machine set-up (b) single axis FiTS

The surface roughness of the workpiece without any compensation mechanism in place has been studied. The surface profile and roughness is measured using ZYGO^{TM} white light interferometer. Figure 5-33(a) shows the surface roughness R_a of the machined brass workpiece. R_a of 48 nm was achieved without any compensation in place. The real-time following error

compensation was enabled by using the PLC0 of the machine controller and the machining with the same process parameters was conducted. The surface roughness of 9 nm (Figure 5-33(b)) has been achieved using the following error compensation mechanism. The results were evident that the machine's performance improved tremendously with the Z-axis following error compensation mechanism.

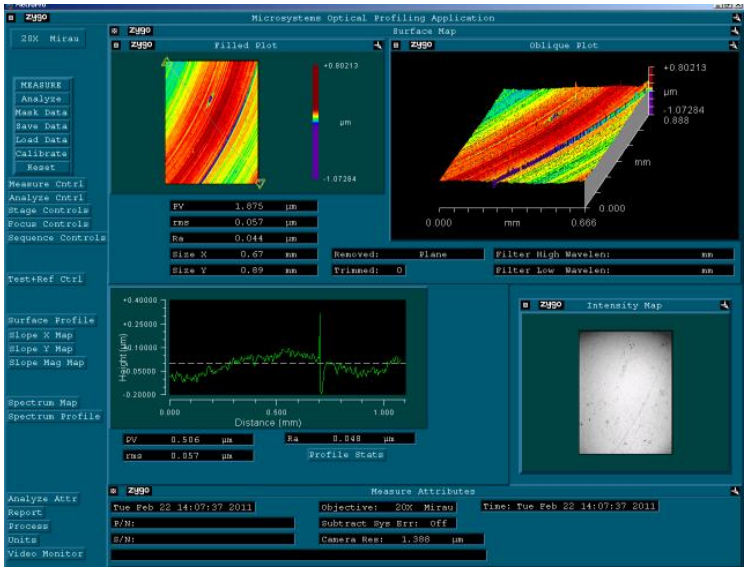

(a)

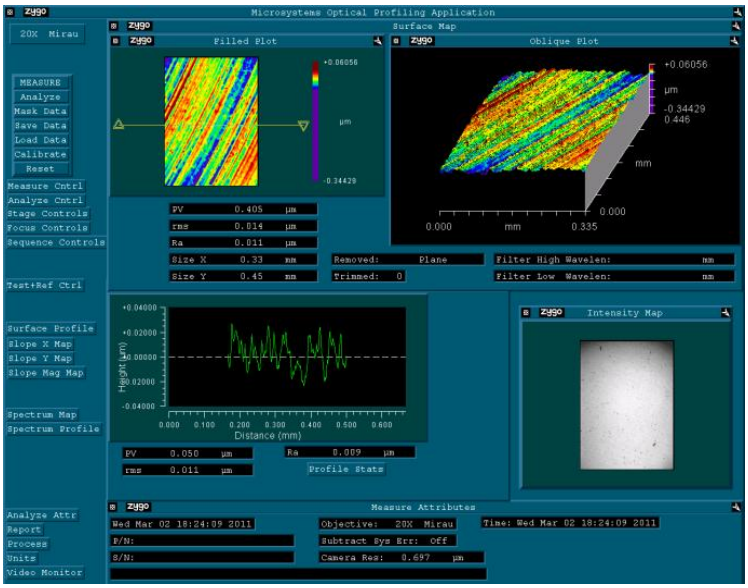

(b)

Figure 5-33: (a) Without compensation Ra 48nm (b) With compensation Ra 9nm

Before conducting the second experiment, the workpiece form was measured using the contact type surface profiler. Since there was no form error compensation is in place, the form error still followed the same trend as in discussed before in section (form error correction).

In the second set of experiment, both the following error compensation and the form error compensation are activated and both the surface profile and roughness have improved. With both the error compensation in place, the surface roughness R_a is 4nm (Figure 5-34(a)) with a total height of the form P_t is reduced to 0.3µm (Figure 5-34 (b)) compared to the P_t value of 1.285µm (Figure 5-29) without the dual error compensation.

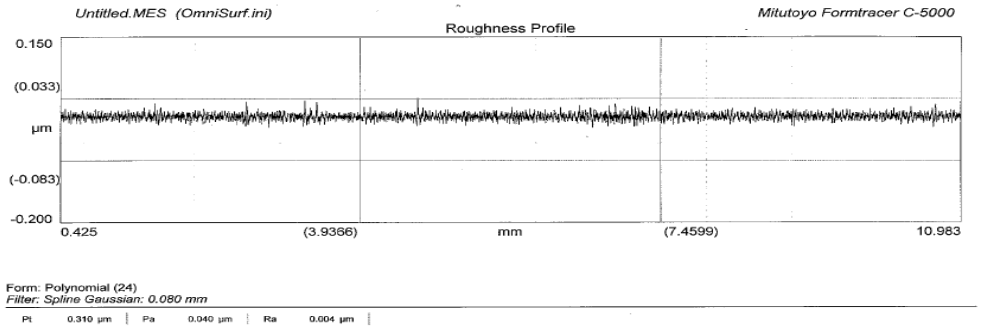

(a)

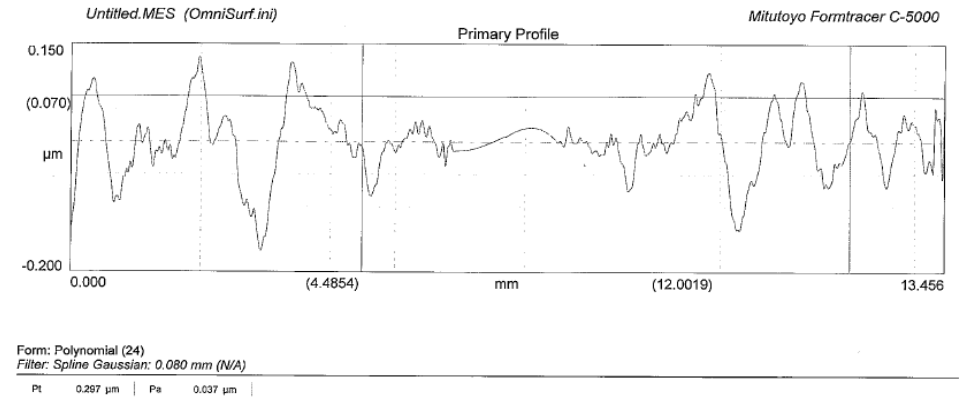

(b)

Figure 5-34: (a) Surface roughness & (b) Primary profile measurement with dual servo compensation

In the third set of experiments, in addition to the following error and form error, the waviness is compensated using the measured sample as mentioned previously. The waviness is measured using the both contact probe and the white light interferometry for the overall surface of the machined surface. Using this data, a section of the surface is taken to study the waviness pattern of the workpiece. In order to verify the repeatability and characteristics of the waviness error on different workpiece material, two samples of aluminum and one brass workpieces were measured using the white light interferometer. The Figure 5-35 (a&b) shows the full profile of the machined aluminum workpiece. Figure 5-35(c) shows the profile of brass workpiece. The two aluminum workpieces showcases identical surface profile while the brass workpiece showcases a slightly different profile with magnitude lesser than the aluminum workpiece. The section view of the three workpiecesFigure 5-36 (a-c) depicts a more clearly the profiles indicating the waviness of higher magnitude for aluminum compared to brass.

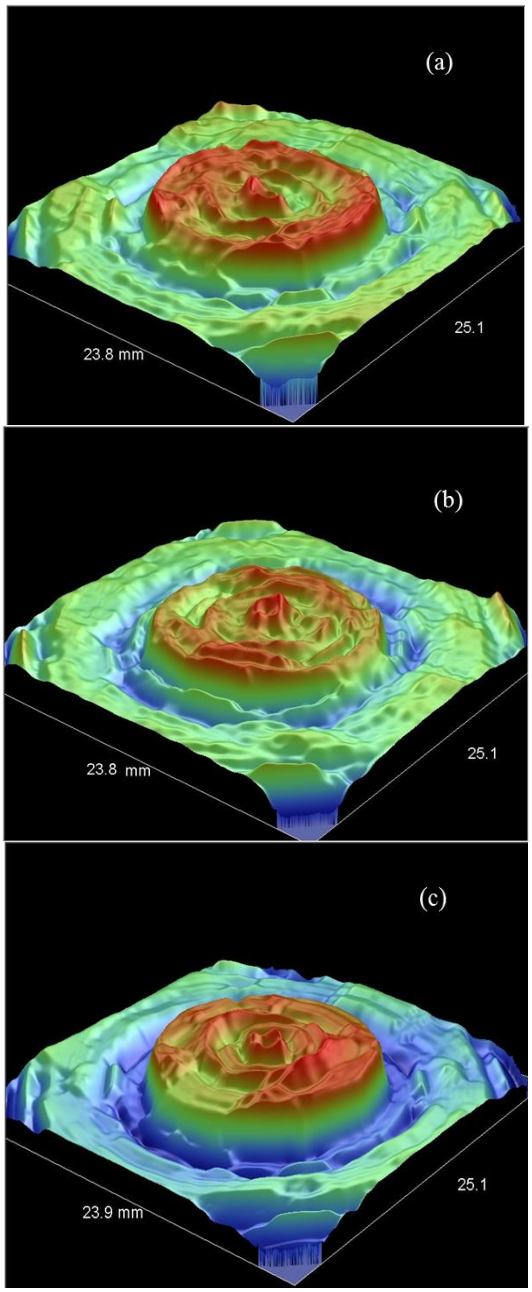

Figure 5-35: White light interferometer imaging of the complete workpiece profile (a & b) Brass (c) Aluminium

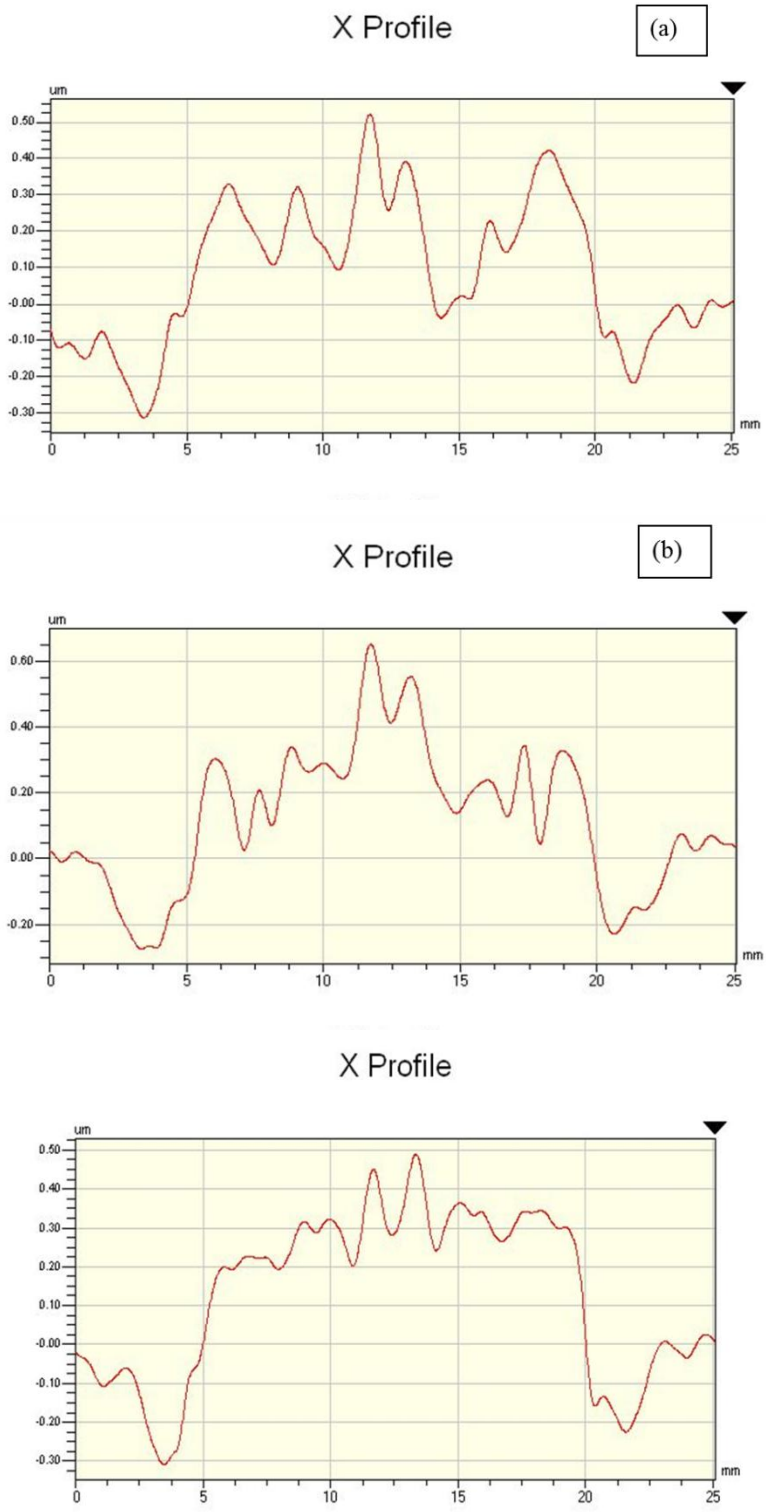

Figure 5-36: Section view of filtered waviness of (a &b) Brass (c) Aluminum

Using the obtained results, the tool-path is generated with compensating for the waviness and the machining of the brass with the same cutting parameters as before was performed. The Figure 5-37 shows the

improvement in the waviness of the workpiece. The reduction through the pre-compensated NC tool-path is effective in waviness compensation with waviness value reduced from 93 nm to 62.8 nm.

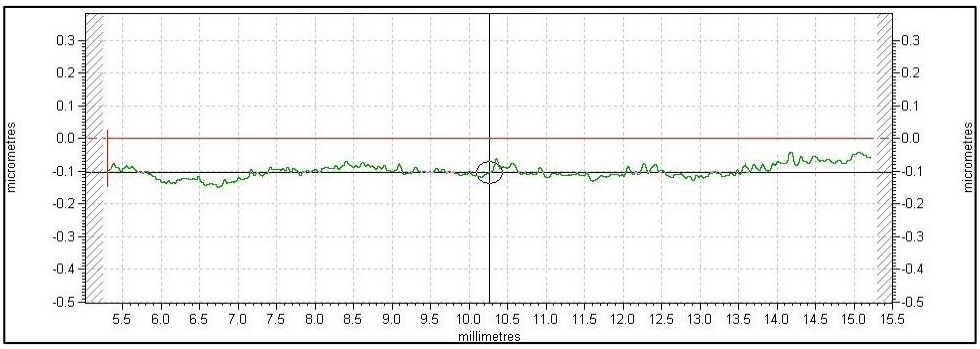

Figure 5-37: Waviness of Brass workpiece after compensation

Figure 5-38 shows the photograph of the mirror finished flat surface profile of brass workpiece with the tool insert reflection.

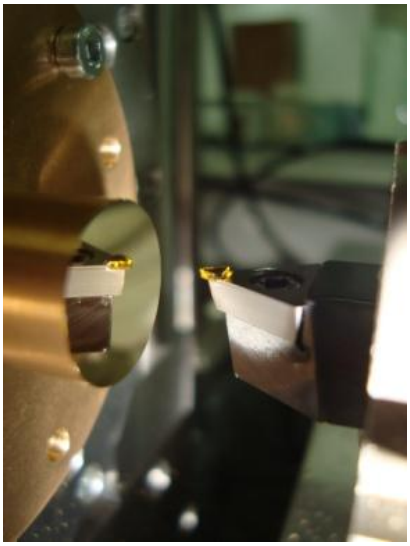

Figure 5-38: Flat machined brass workpiece with tool tip reflection

5.9.2 Contouring Operation

After the successful implementation of the single axis FiTS system for flat facing operation and segregating the error components, the same concept is used in the contouring operation. A concave lens profile is machined and the surface parameters have been studied. The following error and the form error were enabled and the machining cut was performed. The form error seems to

be effective, but the surface roughness and the waviness was not improved in the machined workpiece. Surface roughness R_a of 12.8 nm and waviness of 111 nm was measured. Further study on the surface is conducted to identify the effect of the error compensation in contour machining.

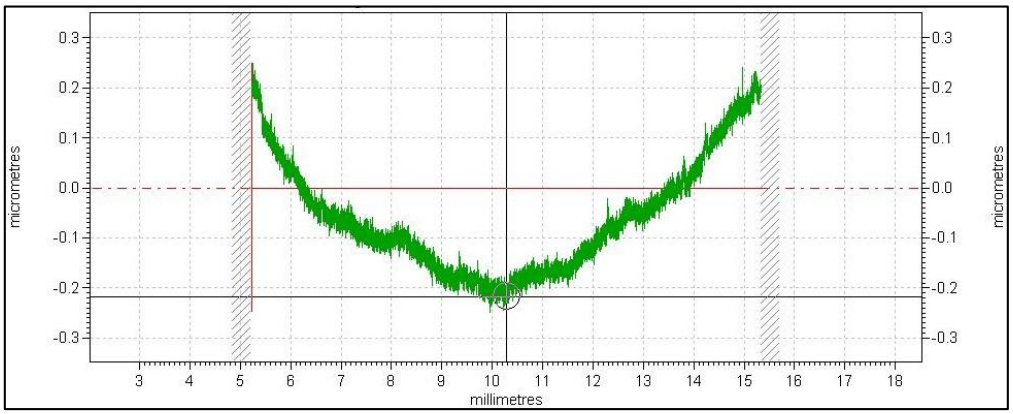

Figure 5-39: Roughness profile of concave surface

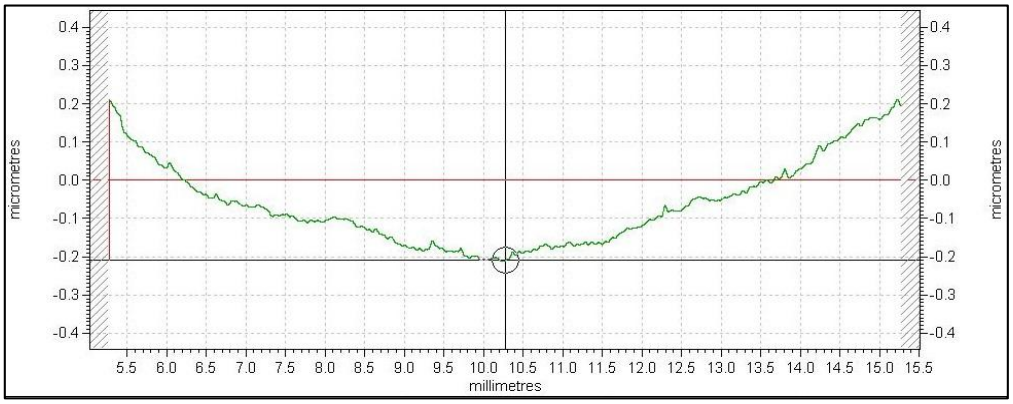

Figure 5-40: Waviness profile of the concave surface

While machining a contour surface, the surface contact between the tool-tip and workpiece occurs at a tangential point. So the error component at the point of contact is the resultant of two error components. So compared to the single axis FiTS which effectively compensated the single axis surface-normal errors during flat facing operation was not sufficient to compensate the two axis error, as in the case of contour profile machining. Hence, for dual axis surface normal error compensation, additional axis is required to compensate the errors due to both the machine slide (X & Z-axes). So in the

next chapter, the focus is to development dual axis dual-servo compensation FiTS system which can be integrated with the DTM machine to improve the surface integrity in contour machining.

5.10 Chapter conclusions

In this chapter, a single axis FiTS system is developed to compensate the geometric and kinematic errors in real-time. The flexure based "inverted double parallelogram" module is introduced and its performance is characteristics revealed that they perform better than the conventional double parallelogram module. The performance of the developed FiTS system is studied analytically and results are compared with the FEM and the actual response of the mechanism. The calibrated single axis FiTS system is incorporated in real-time to compensate the tool positioning error along Z-axis due to the Z-axis following error and X-axis form error along the X travel using dual servo principle. The machining tests were conducted to validate the dual servo principle and results are promising. The Experiments have been conducted to verify the machine's performance characteristics with and without the FiTS compensation. The surface roughness was improved to 4nm from the initial value of 48 nm and the primary profile height P_t was improved to 0.3 μm from the initial value of 1.285μm. The waviness was compensated using the machined sample data and pre-calibrated in the NC tool-path generation and the machining tests shows that the waviness was reduced to 62.8 nm. The objective of developing a single axis FiTS system and implementing it to compensate the systematic and random errors using both real-time and pre-calibrated compensation algorithm without the need for an

auxiliary sensor was successfully implemented. Yet, the required accuracy during contour machining is not been achieved. So as an extension of the current work, development of dual axis dual-servo FiTS system and its implementation in the DTM is discussed in the next chapter.

Chapter 6 Design and Implementation of Dual-axis Dual servo mechanism

6.1 Introduction

In this chapter, the design and implementation of a dual axis FiTS system for the accuracy enhancement of the DTM is presented. The main contribution in this chapter is the development of a novel XY planar flexure based mechanism and study of its performance characteristics. Based on the promising results achieved by implementation of the single axis FiTS system, the novel dual-axis dual-servo compensation mechanism is implemented in this study. Followed by, the effectiveness of the FiTS system is validated by measurement and machining experiments are presented.

6.2 Need for dual axis FiTS system

As mentioned in the conclusion section of the previous chapter, the accuracy of the machined components depends highly on the number of axis required to achieve a particular profile. For example, during a facing operation, the surface-normal error is single axis and most importantly, single slide actuation (X-slide) is enough to achieve the final machined component. But considering a profile as shown in the figure 6-1, the required profile is achieved by simultaneous motion of both X and Z axis of the DTM. But the machined profile represents the error components of both the axes rather than the desired profile. The surface-normal error is a resultant of the two axes error ε_x and ε_y (Y instead of Z) of the machine (Figure 6-1). So for effective

compensation of such errors, a FiTS system which provides the necessary two axis motion is of primary need. The dual axis FiTS system should provide necessary travel range and precise single axis isolated motion for easier control of each axis.

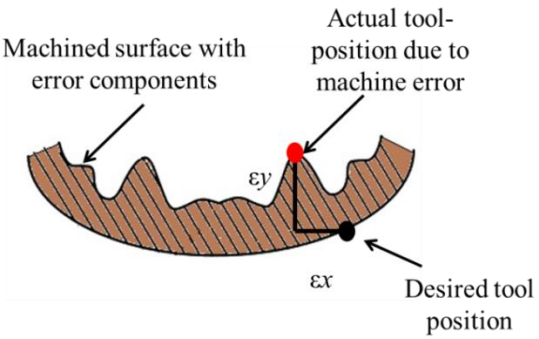

Figure 6-1: Schematic of the contour machined surface

6.3 Dual axis Mechanism Design

Before starting with the design of dual axis flexure based mechanism, basic understandings on the existing design variants are revisited. The design of dual axis flexure based mechanism is complex compared to a single axis mechanism. Based on the literature review presented in the section 2.3.1.4 of chapter 2, there are primarily two kinds of configurations for multi-DOF mechanism – serial and parallel. The various pros and cons of each design type were explained in detail, in chapter 2. A glimpse of the major factors which help in deciding the type of flexure mechanism to proceed with are highlighted with the help of explanation based on the rigid-body counterpart:

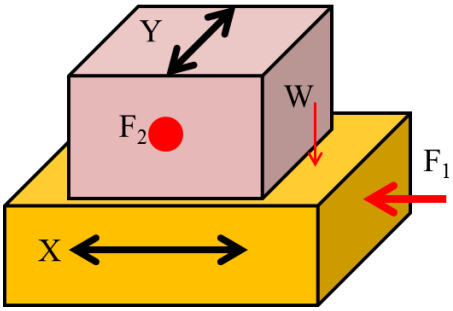

Figure 6-2: Schematic of serial stack type design

6.3.1 Serial stack type mechanism

In serial design, stacked assemblies of several single DOF stages provide the multi DOF mechanism. Figure 6-2 shows the two axes (XY) serial type conventional rigid-body design. The major disadvantage of conventional series design mechanisms is that they are prone to inertial errors due to masses like weight (W) of the Y-axis acting on the base X-axis. The Y-axis actuators/motor and the feedback sensor is not grounded to a reference and is movable since they are mounted on to the X-axis. This produces disturbances to the base X-axis which deteriorates the overall performance of the system. Controlling the axes is another major issue since the axes needs to follow different strategies in terms of tuning parameters and dynamic response/feedback.

6.3.2 Parallel type mechanism

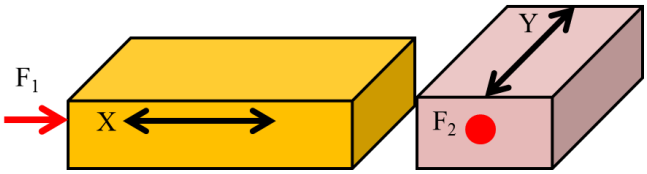

Figure 6-3: Conventional Rigid-body parallel type stage

On the contrary, parallel design (Figure 6-3) is not affected by the above mentioned errors since symmetrical design with same dynamic

characteristics and grounding of the actuator to a reference surface is feasible. The performance of one axis is not dependent on the other and hence the control of parallel type mechanism is relatively easier.

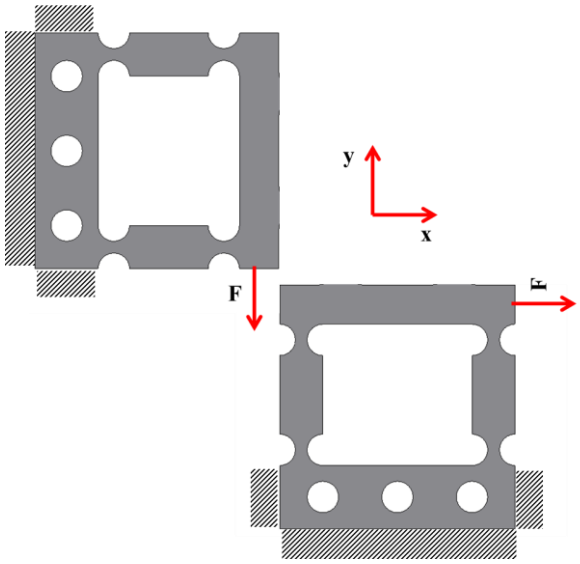

Figure 6-4: Design concept of independent X-Y compliant axis

With this basic analogy of the rigid body mechanism, the flexure based multi DOF mechanisms can be built. Though they are typically different in terms of configuration, the advantages of the parallel design over serial type still remain valid. The major difference in flexure based parallel mechanism is that, the different axis cannot be placed separately as shown in Figure 6-4. For example, in the case of two axis flexure mechanism, the moving workspace cannot be shared between two different axes as in the rigid body counterpart. Since the accurate motion of the flexure mechanisms are achieved due to their planar and monolithic and symmetrical construction, they cannot have two separate motion axes to realize the exact DOF mechanism. Both the axes need to be attached with each other to realize dual axis motion to the end-effector. Also only with this combined configuration, each axis/DOF operates with the knowledge of the other axis/DOF's position. Hence, the design of planar

parallel flexure based mechanism is not a straight-forward approach and certain constraints of the design are explained in the following section.

6.4 Design objectives and constraints

The design of the dual-axis system varies largely from the single axis design. Even though the flexure based serial mechanism overcomes the shortfalls of its rigid body counterpart, the parallel mechanism is compact and more accurate since both the axes have the knowledge of position of the other axis. The following attributes are the key need to be satisfied by the design to effectively implement the dual axis FiTS compensation strategy in the DTM.

- The primary objective of the design is to achieve repeatable system with wide range of motion depending on different actuators. The motion along DOF must be compliant but all other in-plane and out-of-plane stiffness of the system should be higher to prevent the system from erroneous motion.
- In multi-DOF planar, monolithic design, the important factor to be considered is the *cross-axis coupling*. Cross-axis coupling refers to any motion along the Y direction in response to an actuation along the X direction, and vice versa. The cross-axis coupling between the X and Y DOF is an important performance requirement since any cross-axis motion will lead to difficulty in understanding the exact location of each axes and control of the same is very difficult. It also leads to development of a control system to overcome this error motion. Rather, to develop a planar mechanism without inherent cross-axis coupling will be a promising design and its benefits of perfect

rectilinear motion between axis and easier control will increase its implementation to manyfolds.

- The *actuator isolation* is another very important aspect to be considered in the design since PEA cannot withstand any transverse loads and displacements. So the actuation needs to be isolated from the workspace's motion to prevent the motion/displacement transmitting to the actuator. A decoupler is required in-between the point of actuation and the workspace to achieve actuator isolation. The effectiveness of the isolation depends largely on the arrangement of the decoupler in the design.
- Provision for large area of workspace, is required as the proposed dual axis FiTS system has various opportunities such as implementation in accuracy improvement in multi-axis machine tools, precise positioning stage etc., the mounting workspace of mechanism should not be a constraint. So parallel motion with effective utilization of the space is needed. Similarly the reduced mass of the moving system is of a greater concern to achieve better dynamic performance.

With the above mentioned criterion, a new dual axis FiTS system development, performance analysis and effective implementation is mentioned in the rest of this chapter.

6.5 Design of Dual-axis mechanism

A two-axis flexure base is required for the implementation of two identical PEAs as the fine actuators. It was designed based on the same concept as the single-axis flexure base and it has the same material properties.

Figure 6-5 shows an isometric view for the base assembled with the two PEAs. The center mounting platform is 31mm x 31mm. Since the motion of the moving links of the mechanism provides equal displacements on all sides, the rotation effect along the normal *"Z"* axis is negligible. In the current experiments, one of the two ends opposite to the actuation point is used for the mounting the adjustable tool-post. Due to this arrangement, the actuation is axial to the cutting direction and hence the effect of micro cutting force during the contour machining can be compensated by the PEAs' strain-gauge feedback sensor.

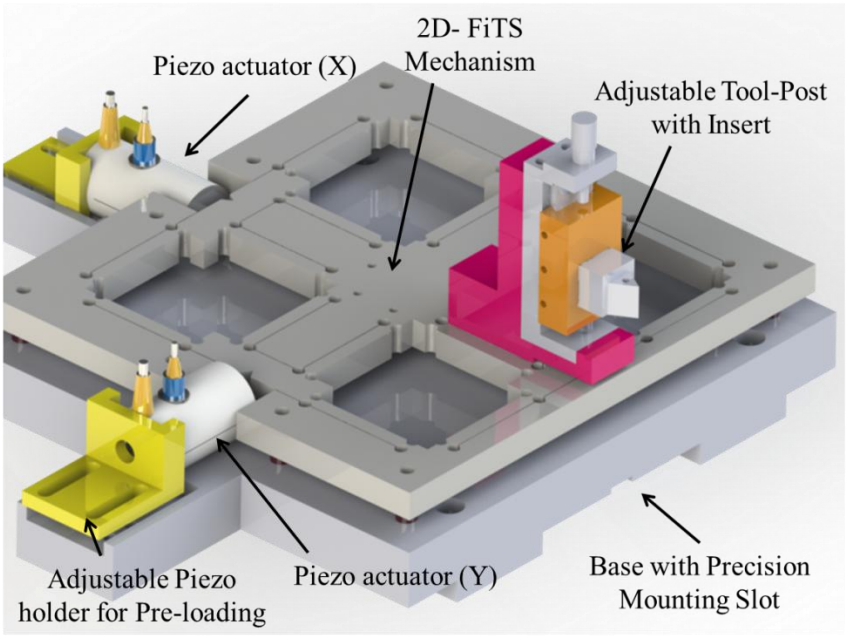

Figure 6-5: CAD model of the developed dual-axis FiTS system assembly

The other advantage of the design is that, due to the rectilinear motion along X and Y axis, without cross-axis coupling, the actual work-holding space can be increased by mounting a base plate on the 4 corners of the moving links as shown in Figure 6-6. Since the stage's displacement is equal on all sides of the moving region, the mounting holes can be extended to the end of the stage. Thus the mounting area of the stage can be increased by

utilizing the four corners of the moving center region. So the effective mounting area of the stage can be increased to 125.50 mmx125.50 mm.

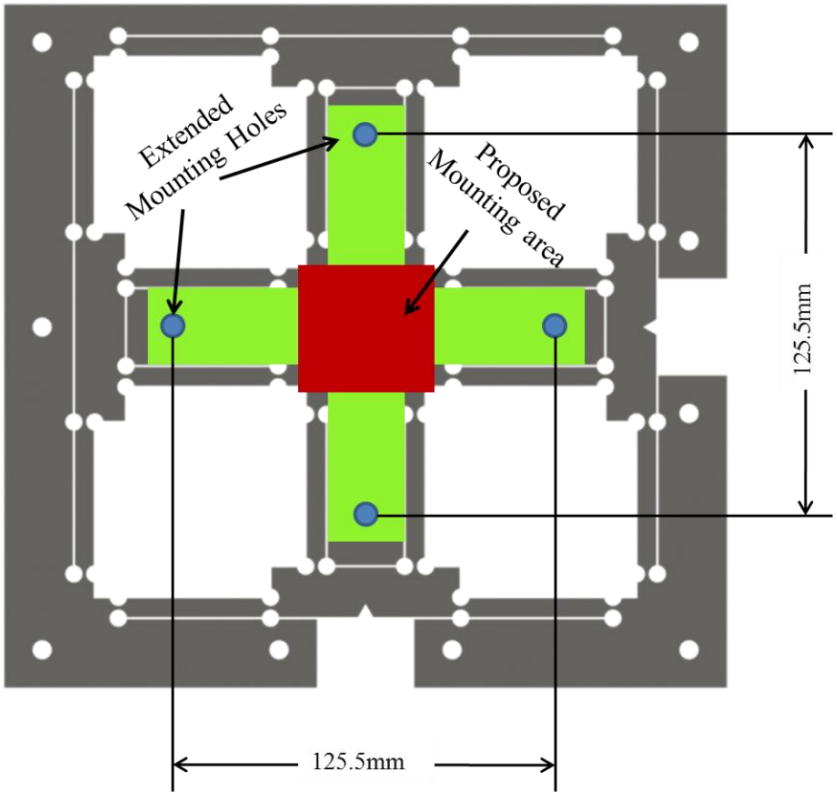

Figure 6-6: Improvement of workspace for larger working area

Another interesting factor worth mentioning about the inverted double parallelogram is that, transverse load which is applied to actuate the orthogonal axis creates either compression or tension in the flexure hinges and the rigid column. An explanation of the same is presented below.

6.5.1 Effect of axial loading of flexure modules

In the single axis FiTS development, the effect of parasitic error was compared between the conventional double parallelogram and inverted double parallelogram. The force act in one single transverse direction of the axis (the most compliant axis of the mechanism) and the axial loading occurs at the hinges alone due to their rotation. But, in the case of the dual axis mechanism,

the flexure modules are provided with both axial and transverse loading to achieve the dual axis displacement. When an axial load is applied to the primary stage of the double parallelogram (Figure 6-7(a)), the inner parallelogram of C and D will tend to buckle under compression and the outer parallelogram of A and B will tend to be in tension due to the load transmitted through the inner parallelogram. When the load applied is reversed, the effect reverses as well. So both tension and compression co-exist between the flexure modules. Due to this effect, they tend have unequal change in the length of the links and hence the parasitic error still exist during axial loading. But in the case of inverted double parallelogram (Figure 6-7 (b)), all the flexure arms A-D either get compressed or be in tension depending on the direction of the force.

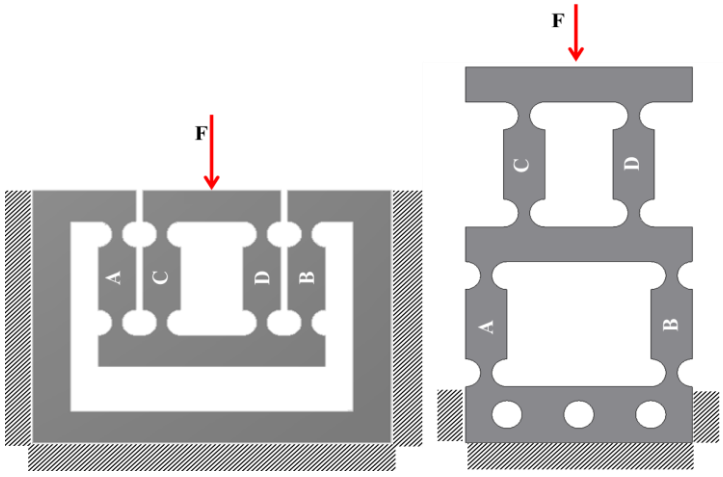

Figure 6-7: Axial loading of double parallelogram and inverted parallelogram modules

Hence, symmetric arrangement of the flexure modules will overcome the deformation by providing an opposite reaction force. Due to this, inverted double parallelogram will produce less error and transmit displacement/force more efficiently.

6.6 Analytical Model of the Dual axis guiding unit

The important factor to be considered in the planar mechanism is the decoupling of the forces acting on the other axes. In the design, there are two kinds of hinge pairs (Figure 6-8). Hinge pair (1) which is the serially arranged hinges fixed at both the ends. They provide the main DOF along the direction of motion and stiffer while a force at orthogonal direction is applied. Hinge pair (2) attached to the inner motion platform acts parallel arrangement to decouple the axial displacement of the stage from transmitting to the actuators in the transverse direction. Due to this decoupling effect, the stage acts as a decoupled system which can be proved from the compliance and stiffness equation along the axial and radial directions. The transverse stiffness of the inner stage will prevent cross-axis error and effective transfer of the displacement from the actuator to the workspace without any lost motion.

To analyze the flexure mechanism, the PRB model which was used in the single axis design cannot be utilized for a complete compliance/stiffness analysis of the dual axis stage since it only considers the compliances of flexures in their working directions. To establish a full kinematic or compliance/stiffness model of the dual axis mechanism, the lumped model of a flexure with the consideration of 6-D compliance in space can be employed. Such a lumped model can be derived effectively by the matrix, since matrix operations can be easily conducted with higher calculation efficiency [103-106].

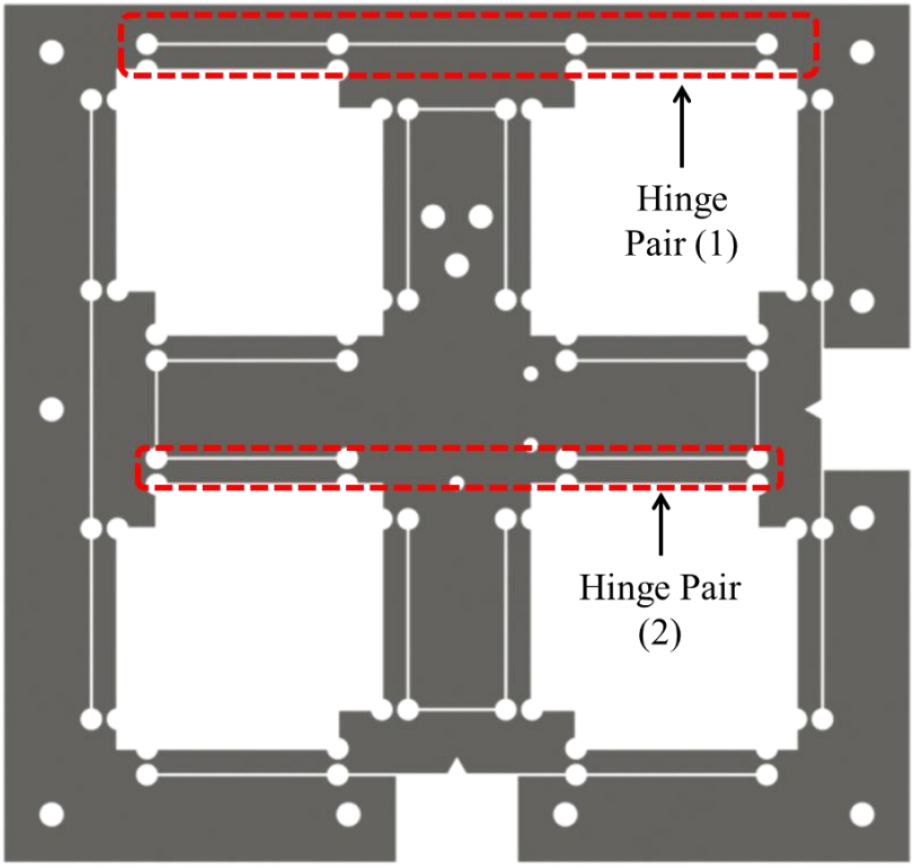

Figure 6-8: Dual-axis mechanism with two different hinge pair

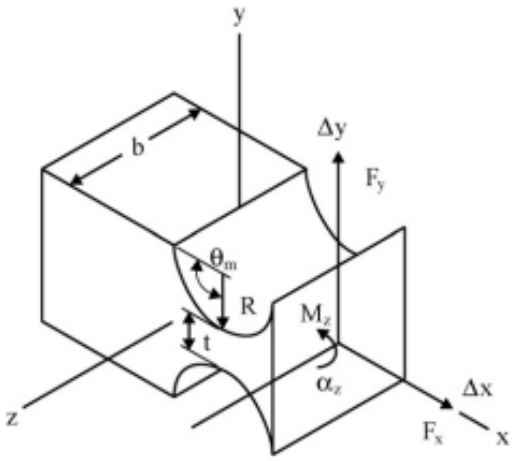

Figure 6-9: Right circular hinge with 6D compliance/stiffness

The compliance matrix for a right circular flexure hinge with the coordinate frame assigned in Figure 6-9 can be written as

$$C = \begin{bmatrix} \frac{\Delta x}{\Delta F_x} & 0 & 0 & 0 & 0 & 0 \\ 0 & \frac{\Delta y}{\Delta F_y} & 0 & 0 & 0 & \frac{\Delta y}{\Delta M_z} \\ 0 & 0 & \frac{\Delta z}{\Delta F_z} & 0 & \frac{\Delta z}{\Delta M_y} & 0 \\ 0 & 0 & 0 & \frac{\Delta \theta_x}{\Delta M_x} & 0 & 0 \\ 0 & 0 & \frac{\Delta \theta_y}{\Delta F_z} & 0 & \frac{\Delta \theta_y}{\Delta M_y} & 0 \\ 0 & \frac{\Delta \theta_z}{\Delta F_y} & 0 & 0 & 0 & \frac{\Delta \theta_z}{\Delta M_x} \end{bmatrix} \quad (6\text{-}1)$$

where, Δx, Δy and $\Delta\theta_z$ represents the linear deflection along *X* and *Y* axes and angular deflection along *Z* axis. ΔF_x, ΔF_y and $\Delta\theta_z$ are the force vector along x,y and z axis respectively.

From the matrix (eqn. (6-1)), the elements C (1, 1), C (2, 2) and C (6, 6) are the most critical in the analysis of the dual axis stage. To find these compliance components, the value of deflection and load vector needs to be computed. The deflection formulae for the elliptical hinges are provided in the following compliance matrix form [103] eqn. 6-2. This can be reduced to a circular hinge with ε=1 and l_o as radius of the circular hinge "*r*".

$$\begin{bmatrix} \Delta x_o \\ \Delta y_o \\ \theta_{zo} \end{bmatrix} = \begin{bmatrix} P_3 & 0 & 0 \\ rP_1 & r^2P_1+P_2 & 0 \\ 0 & rP_1 & P_1 \end{bmatrix} \begin{bmatrix} F_x \\ F_y \\ M_z \end{bmatrix} \quad (6\text{-}2)$$

where, P_1, P_2,and P_3 are compliances along angular deflection direction α_z and linear deflection along Δy and Δx. The values are given by the following equation (6-3 to 6-5) [103].

$$P_1 = \frac{3\varepsilon}{2Edb^2}\int_{-\theta_m}^{\theta_m}\frac{cos\theta}{(1+\beta-cos\theta)^3}d\theta \quad (6\text{-}3)$$

$$P_2 = \frac{3\varepsilon^3}{2Ed}\int_{-\theta_m}^{\theta_m}\frac{sin^2cos\theta}{(1+\beta-cos\theta)^3}d\theta \quad (6\text{-}4)$$

$$P_3 = \frac{\varepsilon}{2Ed}\int_{-\theta_m}^{\theta_m}\frac{cos\theta}{(1+\beta-cos\theta)}d\theta \quad (6\text{-}5)$$

where θ_m is $\pi/2$ and $\varepsilon=1$ for right circular hinges

Since the circular hinges provide the single axis of rotation, the reaction forces and moments at the hinge center provides an understanding of the compliances/stiffness of the stage. The analysis consists of two parts: firstly the hinge pair (1) which forms the outer linkage in the system. They transmit the forces in the axial direction and also they resist the disturbance due to transverse loading. They prevent the transverse loading of the actuator and helps in actuator isolation. The structure is statically indeterminate in nature with two ends clamped. The Figure 6-10 (a) shows the forces acting and the dimensions of the hinge pair (1).

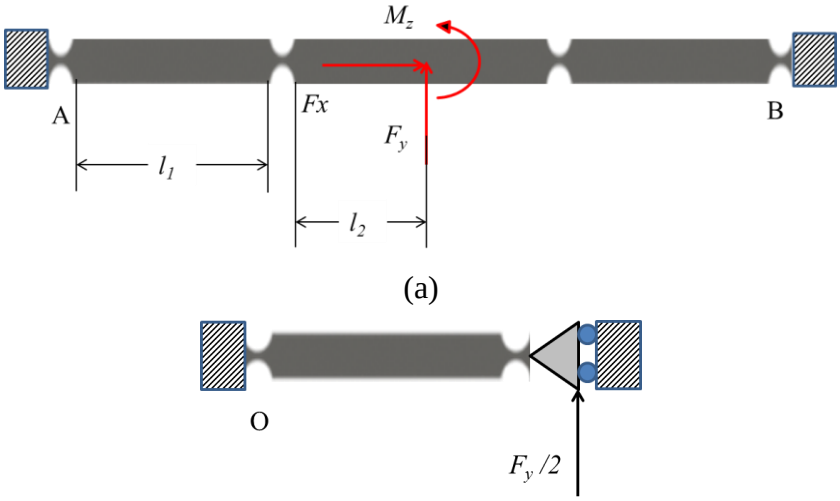

Figure 6-10: Free-body diagram of hinge pair (1) and (2)

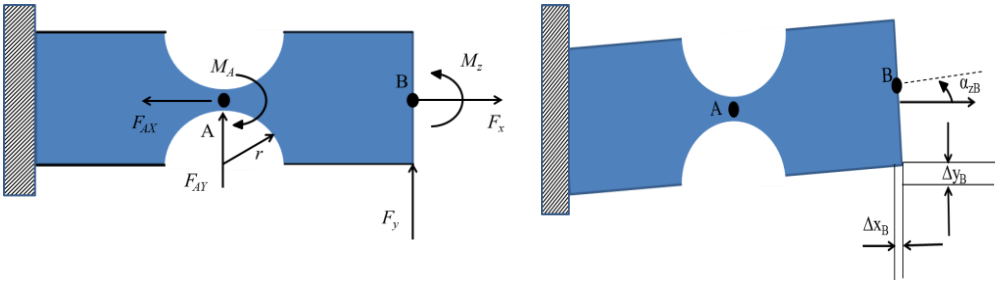

Figure 6-11: Forces and Moments due to deflection of single hinge in hinge pair (2)

From static equilibrium conditions Figure 6-11 for applied force F_y along y direction, we develop the following two equations:

$$F_{AY} = -\frac{F_y}{2} \tag{6-6}$$

$$M_A = -(3r + l_1 + l_2)\frac{F_y}{2} \tag{6-7}$$

where, F_{AY} and M_A is the reaction force and the moment at the hinge center (A) caused due to the half of the input force (Figure 6-10 (b)). Since no moment is applied at the center of the stage, M_z can be neglected.

From the compliance matrix equation 6-1, two main elements C (1, 1) and C (2, 2) can be computed. Since the effect of M_z is compensated by the opposite pairs of hinge pair (2) the term C (6, 6) is neglected.

From the following compliance value, the characteristics of hinge pair the stiffness and compliance along Y axis can be identified.

$$\frac{\Delta x_0}{F_x} = P_3 \tag{6-8}$$

$$\frac{\Delta y_0}{F_y} = P_1\frac{(3r + l_{1+}l_2)^2}{4} + P_2 \tag{6-9}$$

From the above equations 6-8 and 6-9, it is observed the compliance along Y axis is more than that of X axis. The hinge pair (1) behaves as an

actuator isolator by preventing the forces along X axis while actuation along Y is provided. Similarly, the inner hinge pair (2) provides the necessary decoupling effect by being rigid on the transverse direction and preventing the motion (cross-axis coupling) from transferring to the transverse actuator due to the presence of roller support on the workspace side.

Figure 6-12 shows the approximate model of the dual-axis FiTS parallel mechanism. The design of dual axis stage is also conceived with the similar inverted double parallelogram flexure module as explained in chapter 5. The inverted double parallelogram is configured in such a way that the inner pair C-D is connected to the workspace mounting region but, opposite to the outer pair A-B. Each of the total 4 inverted double parallelograms is mentioned in different 4 different colors to differentiate them. The symmetrical arrangement of a pair of inverted double parallelogram is provided for each axis. Since the FEM of the single axis FiTS guiding mechanism provided the same trend as that of actual displacement, a detailed FEM analysis is performed to validate the dual axis FiTS system.

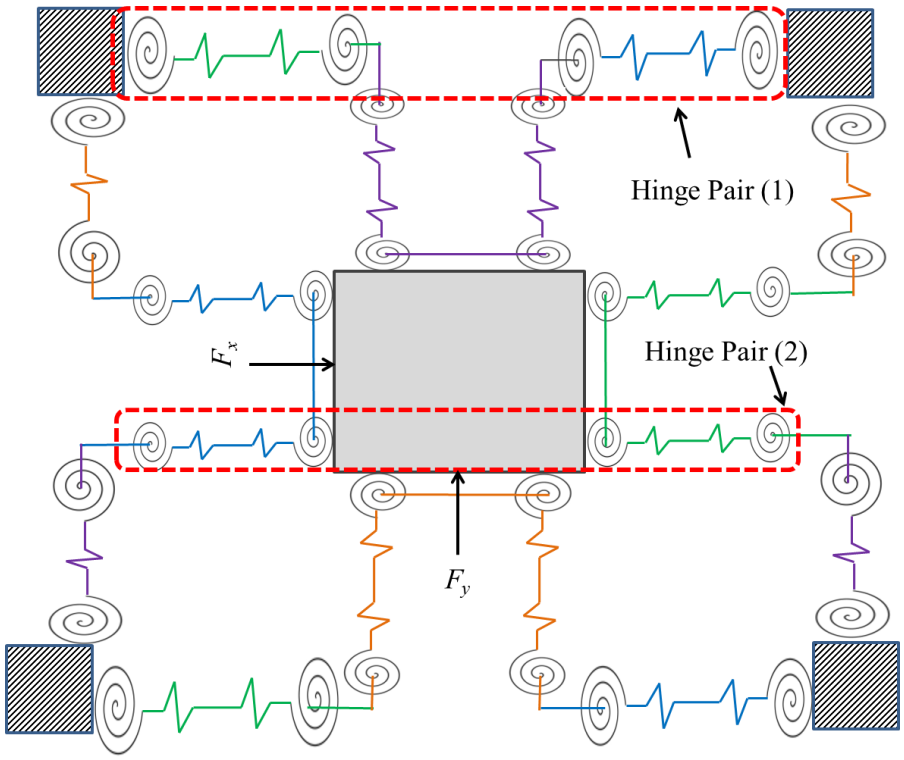

Figure 6-12: Approximate model of the dual-axis FiTS parallel mechanism

6.7 Finite Element Method

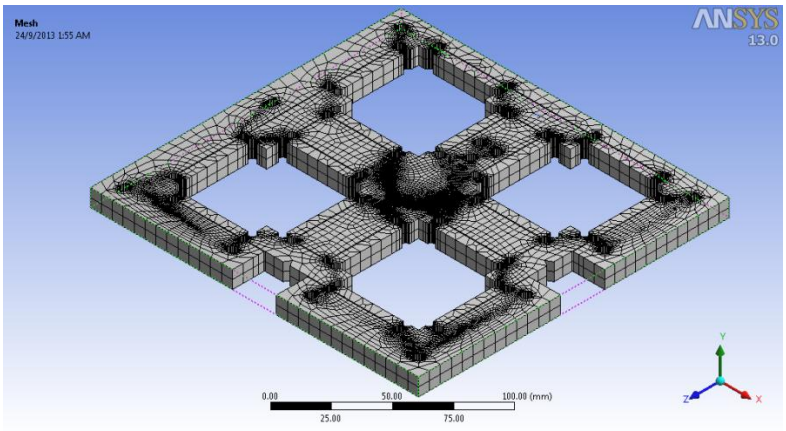

Figure 6-13: FEM model with mesh refinement in hinge region

In the FEM analysis, the material is assigned as carbon steel with a Young's Modulus of 210 GPa, a density of 7800 kg/m^3, and a Poisson's ratio of 0.3. 2-dimensional element PLANE 82 is selected with large deformation to include the axial tension influences on the flexure hinges. The refinement of level 3 is provided to the hinges. The Figure 6-13 shows

FEM mesh model with the refinement in the hinge regions. The force-displacement and the maximum stresses on the flexure hinges are studied for single and coupled XY axes. Figure 6-14 shows the force-displacement characteristics of dual axis mode actuation of the stage. The single axis mode of the dual axis stage also exhibit displacement output. The cross axis error is negligible in the dual axis coupled motion with error obtained is lesser in magnitude by an order of two of the given displacement; the stage is considered decoupled. The moving platform of the dual axis stage provides equal displacement and thus concluding that the extension of the stage workspace (Figure 6-6) is feasible in the design.

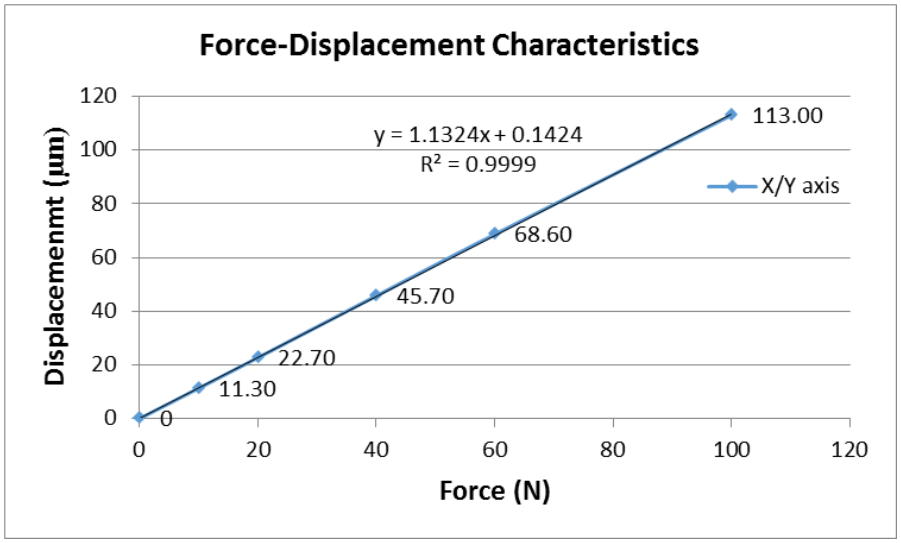

Figure 6-14: Force-displacement characteristics of dual-axis stage

The modal analysis of the stage reveals that both first and second mode exhibit similar frequency of operation due to their symmetry in design.

Table 6-1 shows the frequencies for the 6 modes. The first and second mode has a frequency more than 200Hz which along the actuation direction (XY) can be sufficient for the FiTS system.

Table 6-1: Modal analysis of dual axis stage

Mode	Frequency (Hz)
1	213.35
2	217.63
3	523.35
4	567.71
5	996.67
6	1004.1

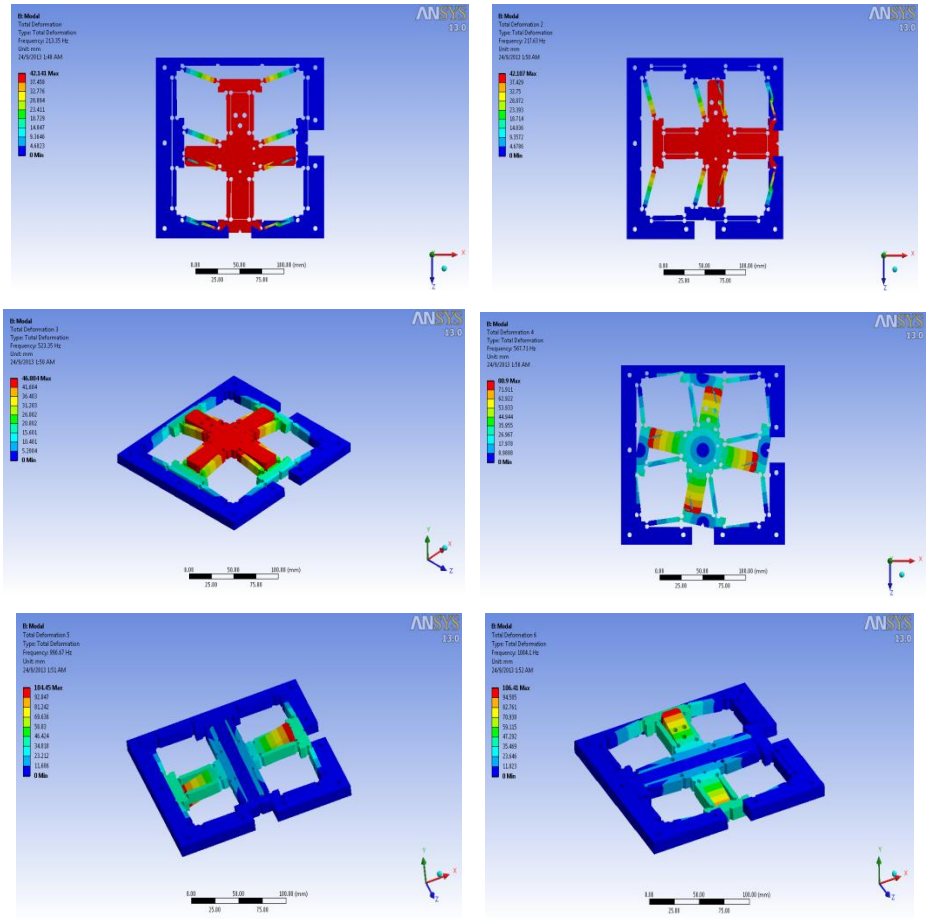

Figure 6-15: Modal Analysis results for dual axis

6.8 Mechanical Calibration

6.8.1 Displacement analysis

The displacement measurement of the dual axis FiTS system is studied to analyze the decoupled motion characteristics of the system. Figure 6-16 shows the photograph of the displacement measurement. Two pair of PEA and CAP sensor is used to perform the calibration of the stage. The stage is calibrated by actuating in single axis mode and dual axis mode. The single axis actuation helps in understanding the input versus output displacement of the FiTS system. But in dual axis mode, the performance of the stage can be analyzed in detail. The cross-axis coupling and the actuator isolation, which were mentioned in the design constraint, can be understood by dual-axis mode.

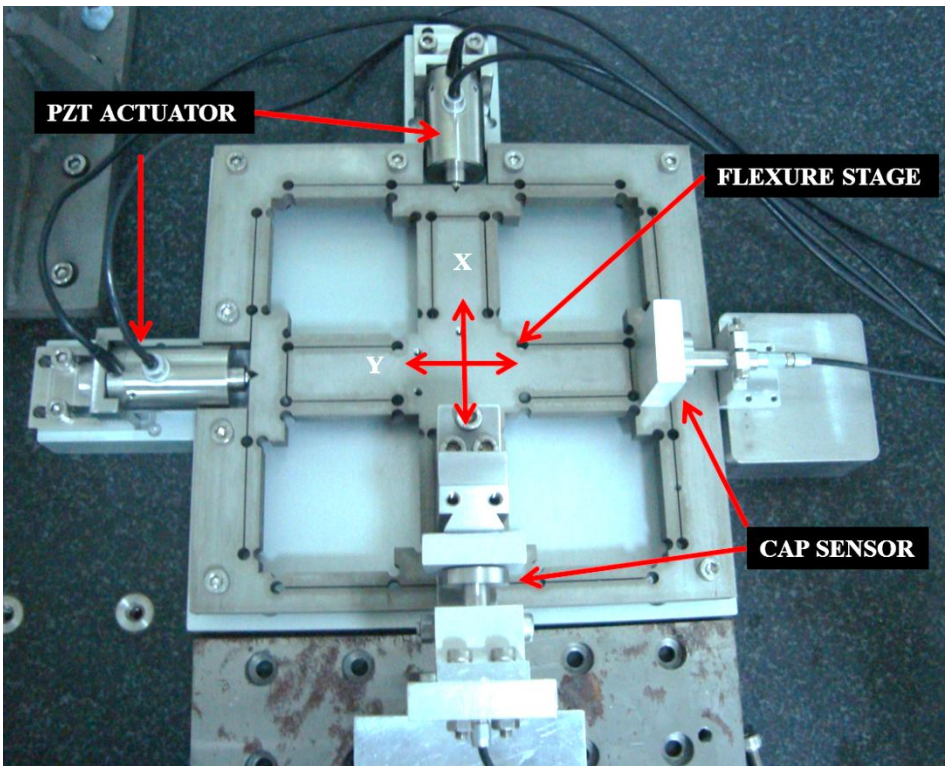

Figure 6-16: Photograph of X-Y axis displacement measurement

Similar to the Labview code developed in single axis FiTS system, an extension of the same is developed in this study. A synchronized X and Y actuation and simultaneous data recording to capture the displacement measured by the CAP sensor was developed to study the dual axis mode. The screenshot is added in the Appendix D.

6.8.1.1 Step Response study

The step response of the developed dual axis FiTS system is studied similar to section 5.6.3.2. It is understood from the single axis FiTS system that only closed-loop performance provides the necessary output, the step response calibration is conducted only in closed-loop. Figure 6-18 shows actual screenshot of the output displacement for dual axis mode. The step response of dual axis displacement output is studied to identify the cross-axis errors and performance in stair-case step mode. Figure 6-18 shows the step response of the stage in coupled dual axis mode. The predictions from the analytical and FEM are validated from the results. The X and Y simultaneous actuation provided an exact following of the command by individual X and Y axes in the dual axis mode. The effect of one axis motion with the other is not evident at lower displacement range upto around 7 µm and further displacement provided a deviation lesser than 5% of the overall travel length. Since in the dual axis FiTS system implementation, the motion is limited to 5 µm similar to the single axis FiTS, the design can be considered effective. The deviation could be eliminated by incorporating an external sensor to measure the actual stage motion. Either a dual axis linear glass scales or the similar set-up of CAP sensor which is used in the calibration test can be used to form the closed-loop system for the stage instead of the PEAs' strain-gauge sensor.

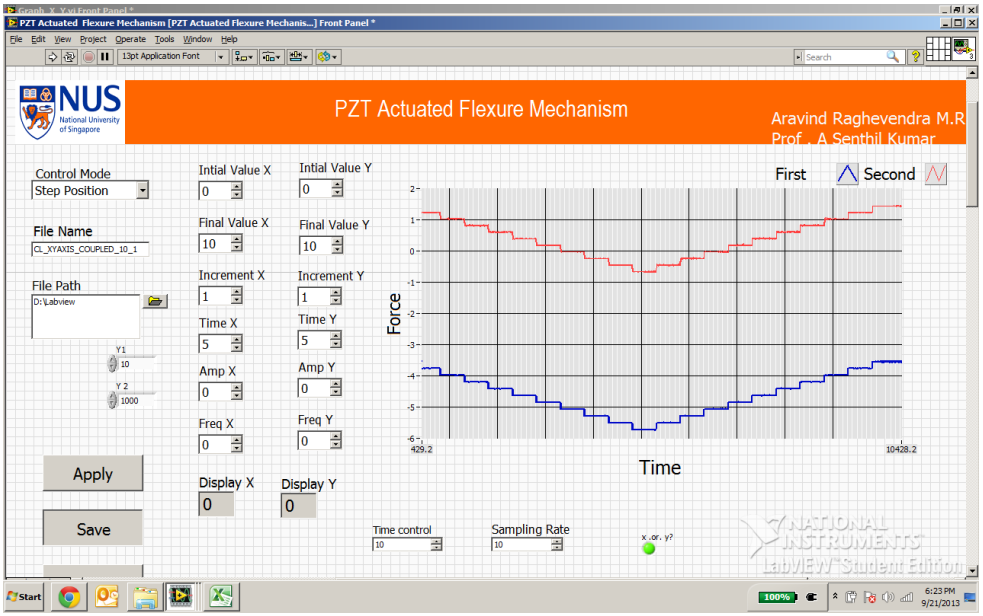

Figure 6-17: Actual Labview screenshot of step-response in Dual axis mode

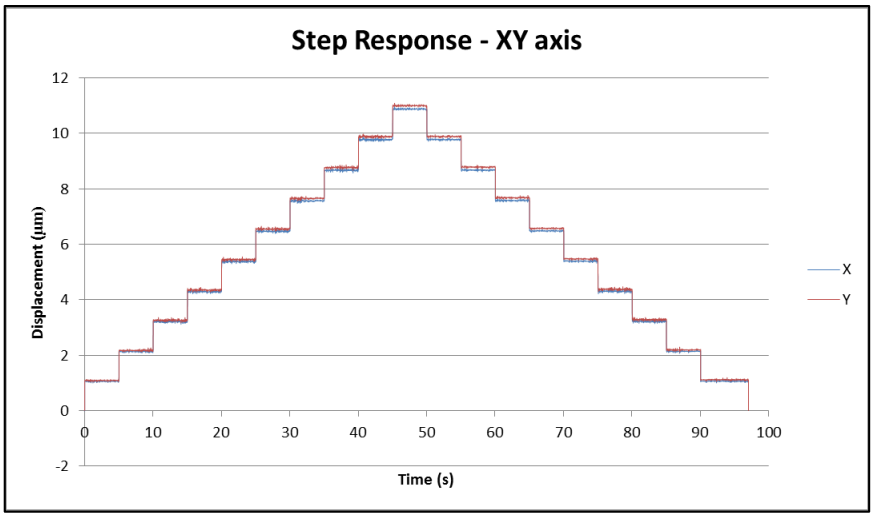

Figure 6-18: Step response of simultaneous X-Y actuation

6.8.1.2 Single step response study

In the single step study, the displacement of the X and Y axes are studied for the given input of 1V. The performance of the developed dual axis FiTS is similar to that of single axis FiTS with actuator rise time (60% of commanded value) is 6 ms, and the overshoot is 19.78nm (Figure 6-19) for both X and Y axis. The steady state error is 20 nm, which is predominantly due to sensor dynamic noise level and dynamic response of the PEA. The

closed-loop response shows excellent agreement with the simulated response without any considerable error motion between the axes.

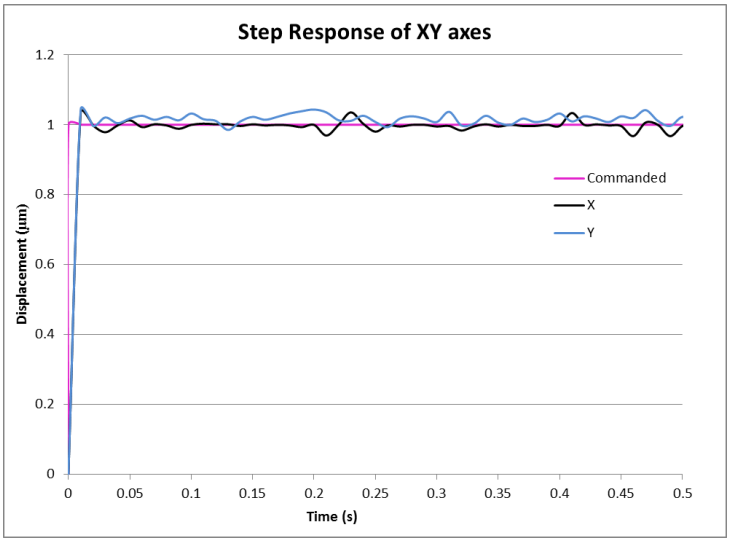

Figure 6-19: Single Step response of coupled XY motion

6.8.1.3 Sine waveform study

In order to validate the dynamic response of the system, a sine waveform input with varying frequency was applied to the actuators. The response clearly shows the system is decoupled and response of system follows the command upto 100 Hz. This response limitation could also be due to the actuators maximum closed-loop response of 150 Hz. The Figure 6-20 (a) and (b) shows the sine response of the system for 10 and 100 Hz, respectively. The error at the region where the axis changes its direction of motion (peak and valley) is critical in determining performance of the stage. The error value is lesser than 50 nm and this value can be improved by providing an external sensor to actively close the displacement loop of the stage. From the results it is understood that the dynamic performance of the stage is not affected with the input operating frequency. These calibration results are promising to incorporate the dual axis FiTS system to compensate the form and following error of both X and Z slide of the DTM.

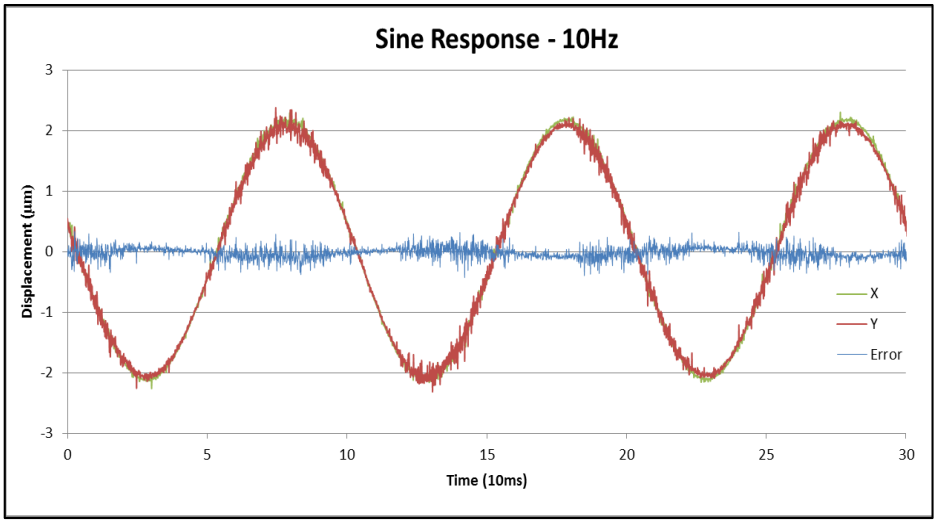

(a)

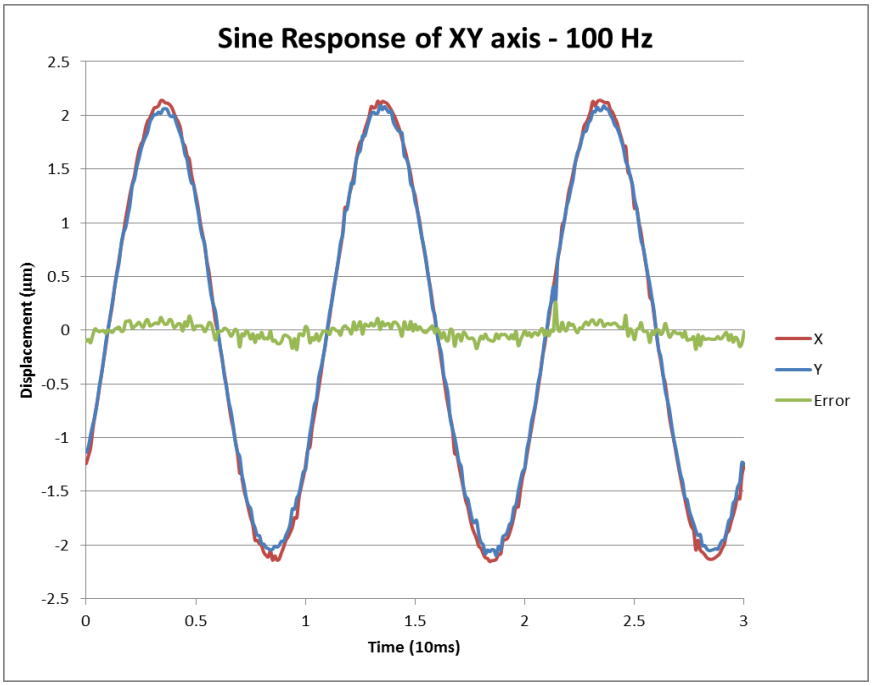

(b)

Figure 6-20: Response of the XY coupled motion for sine wave input at (a) 10 and (b) 100 Hz

6.9 Dual Axis error compensation mechanism

Similar to the single axis compensation mechanism, in the dual axis compensation, the error components mentioned in section 4.4 is measured and recorded for both X and Z axis slide. Figure 6-21 shows the error components of combined X and Z axis slide. Similar to the X-slide measurements, the Z-

slide form errors were measured and the compensation was formulated into the PLC0. Since the form error is slide's position dependent, the real-time data needs to be gathered for X and Z axis separately and compensated by the respective Y and X axes of the dual axis FiTS. The following error of the X and Z axis is computed and compensated in real-time by the X and Y axis of the developed dual axis FiTS system. The compensation methodology was followed as similar to the single axis FiTS system with the additional error components being compensated by the axes defined above.

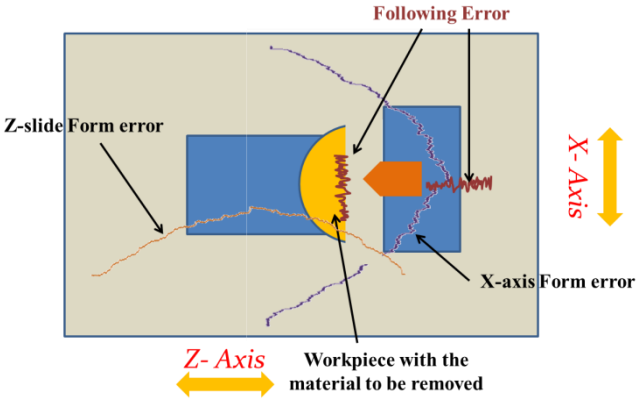

Figure 6-21: Schematic of the dual axis form and following error

6.10 Machining performance

The machining test was performed using the dual axis FiTS system. Figure 6-22 shows the designed CAD model of the dual-axis assembly in the machine. The tool-post is mounted axially to the X-axis of the FiTS system. Similar micrometer adjustment is provided to alter the tool height for the new dual axis FiTS system.

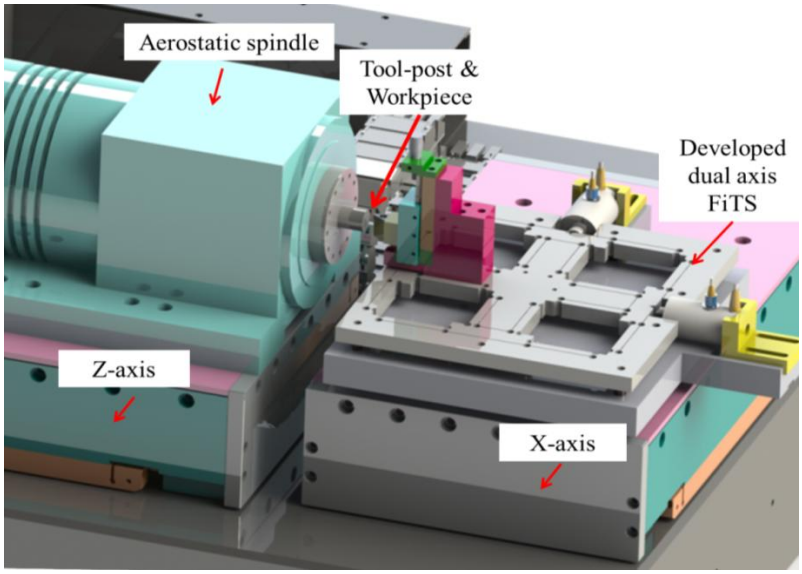

Figure 6-22: CAD model of dual axis FiTS system assembly in DTM

The machine of brass and aluminum workpieces where conducted with same parameters as followed in single axis FiTS machining study. The Figure 6-23 shows the photograph of the dual axis FiTS system set-up.

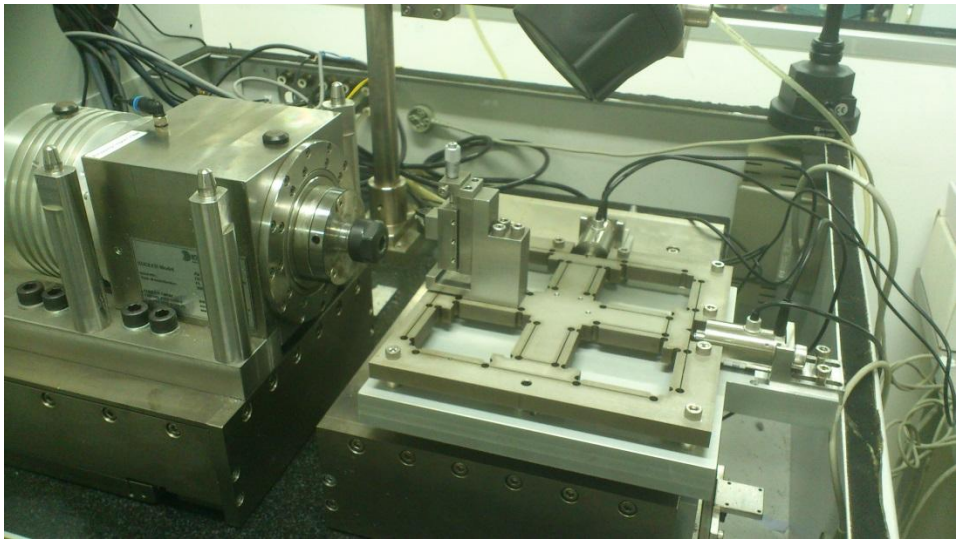

Figure 6-23: Photograph of the dual-axis FiTS set-up

6.10.1 Machining Experiments

The compensation mechanism using the developed dual axis FiTS system works effectively and the improvement in the surface integrity of the contour machining is visible from the results. The Figure 6-24 shows the surface roughness value which had been improved to 6.5nm from the previous

value of 12.8 nm. Figure 6-25 shows the profile of the machined concave surface. Figure 6-26 shows the mirror finished brass and aluminum workpiece with the contour (concave) profile showing no signs of surface irregularities. Thus improvement due to dual axis FiTS system is promising to compensate the dual axis contour machining errors in machine tools.

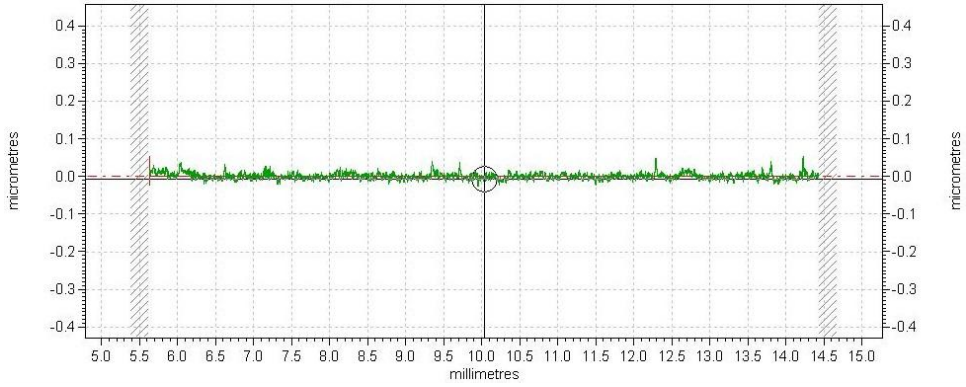

Figure 6-24: Surface roughness of contour (concave) machined surface

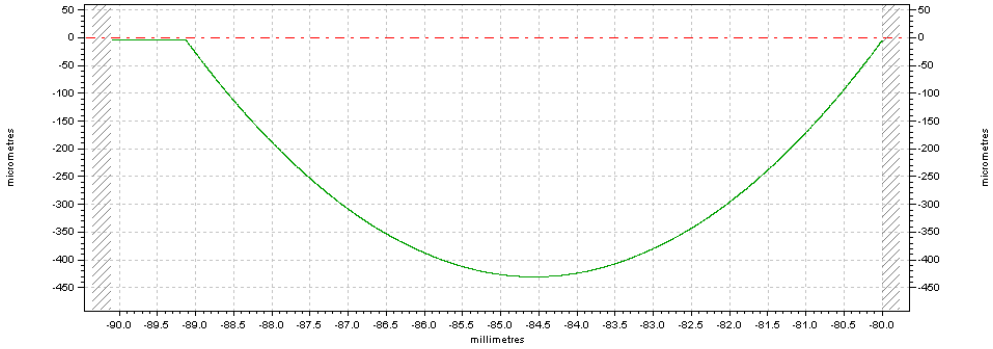

Figure 6-25: Profile plot of contour (concave) machined surface

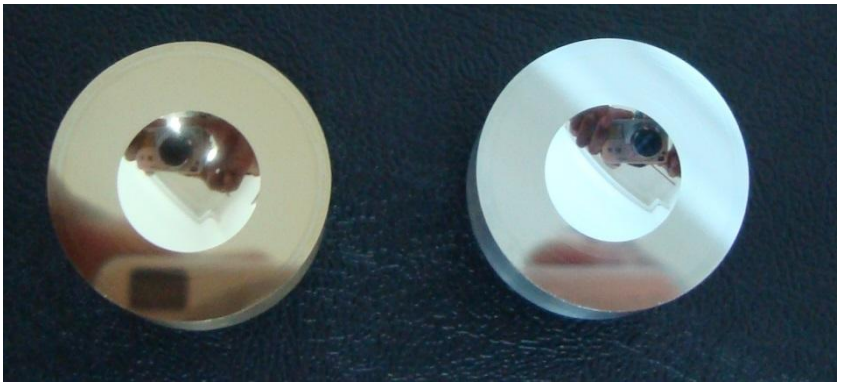

Figure 6-26: Mirror-finish concave profile machined on brass and aluminum workpiece

6.11 Chapter conclusion

The requirement of the dual axis FiTS for diamond turned contour surfaces. The FiTS axis enhancement to dual axis is mandate to achieve the surface integrity which has two components to compensate for. The developed dual axis FiTS systems' performance is studied from its mechanical characteristics. The actuator isolation is achieved for the whole range of displacement and cross-axis error is negligible for a range of 7 µm displacement. Further displacement provides a cross-axis error of 5% of the overall travel. The reason for this is not limited to the mechanical design but to the lack of external feedback sensor to measure the dual axis stage. The design has the provision for mounting the external sensor for real-time monitoring of the stage and it will definitely improve the performance of the dual axis FiTS system. The sine response of the system is also tested and results shows error lesser than 50 nm between the axes. The dual axis dual servo FiTS compensation is implemented on the DTM and the surface quality of the contour workpiece is improved to 6.5 nm from 12.8 nm.

Chapter 7 Conclusions and Future Work

7.1 Main Contribution of the Research

The main objective of the research is to develop a two dimensional compliant mechanism for enhancement of machine tool accuracy by active error compensation using dual servo principle. A dual servo concept is developed and implemented in a DTM to achieve real-time enhancement of the machine tool accuracy. The single axis and dual axis FiTS system is designed, analyzed and integrated on a DTM to improve the accuracy of the flat face and contour mirror finishing operation.

As mentioned in the section 2.5, the aim of the research is achieved by accomplishing the following major contributions of the research:

1) A systematic study on flexure hinge parameter is conducted with the design, analysis and testing of a microgripper with "class 2" mechanical leverage to amplify the output displacement. The circular hinges provide better displacement characteristics (around 25%) for a given input force compared to elliptical hinges. The radius of the flexure hinge (r) and the web-thickness (t) predominatly defines the bending stiffness of the flexure hinges. The right-left orientation of the flexure hinge location in which the distance between the two hinges are least provides the maximum displacement.
2) A novel efficient compliant mechanism module called "Inverted Double Parallelogram" was introduced. The performance study of the

new design revealed that for both axial and transverse loading, parasitic error, which is one of the important aspect in deciding the accuracy of the mechanism is reduced significantly. FEM study revealed that for a maximum output displacement of 145 µm, the parasitic error value of the developed inverted double parallelogram is 65 nm which is only 0.04 times the parasitic error value (1.54 µm) attained by the conventional double parallelogram design. Effective actuator isolation and avoidance of cross-axis error are achieved due to the improved axial stiffness of the developed design, which is an important factor in multi-DOF mechanisms.

3) A real-time dual servo compensation mechanism is developed with the machines' controller and the auxiliary servo working in synchronization to achieve better machine tool accuracy. Control logic for effective implementation of the dual servo principle is developed with the single machine controller controlling the machine and auxiliary axes, simultaneously.

4) The single axis FiTS system is developed using the new inverted parallelogram module. The mechanical performance characteristics of revealed that a maximum of 14.1 µm displacement is achieved for a 10V input. An analytical model of the single axis FiTS is developed and the overall stiffness of the system is 4.943 N/µm with the effective displacement of 15.68 µm. The deviation found between the two values is found to be due to sensor's uncertainty of 15%, the manufacturing error in the flexure hinge fabrication and the deviation for the rated PEA stiffness. The open and closed loop study was

conducted and the response time of single axis FiTS system was 20 ms and 800 ms, respectively. The error components which cause the surface-normal error were identified in the DTM and are compensated in real-time. The following error was reduced from 200 nm to 20 nm and the form error is reduced from 1.285 µm to 0.3 µm. The waviness was improved from 93 nm to 62.8 nm. Due to error compensation along single axis (normal to Z-slide), the contour machining did not improve significantly. The surface roughness of 12.8 nm and waviness of 111 nm was achieved.

5) In the second development, a dual axis, planar, compliant FiTS system achieve actively decoupled XY axis stroke of 7 µm with stiffness of 1.132 N/µm and good dynamic response of upto 100 Hz. The results demonstrated that the dual axis dual servo compensation implementation in contour machining significantly improved the finished surface roughness to 6.5 nm.

The above implementation of dual axis compliant mechanism for error compensation of DTM revealed that machine tool accuracy can be significantly improved and the resulting machined workpiece accuracy can also be improved effectively.

7.2 Recommendations for Future Work

Dual axis fine tool servo is new and not much of research effort has been contributed. There are several possible research directions for future work in the FiTS system. The direct extension from this study and possible

application of the developed FiTS in the related research provides greater scope for improvement in micro/nano machining

i. The closed-loop performance of the single and dual axis FiTS can be improved using an external sensor for accurate positioning and hence achieve better surface integrity. Detailed dynamic response and modeling study can be performed on the stage and their characteristics can be optimized building a controller with specific control system.

ii. The developed stage can be implemented in micro milling and EDM process where the extended workspace can be used to mount the workpiece during micro array machining.

iii. Since the stage has the nano-metric positioning accuracy, ductile-mode machining with real-time force feedback on two dimensional feature generation in material ranging from ductile to brittle spectrum can be implemented.

iv. Other machine tool systematic and random errors along the any two machine coordinates which are caused by a three axes machine can be effectively compensated to achieve better surface quality workpiece.

v. Online measurement of the machine workpiece can be implemented with non-contact sensor and the measured value can be compensated in the subsequent process. By this method both pre-compensation and real-time compensation can be achieved in one single setup.

REFERENCES

[1] Taniguchi N. Current status in, and future trends of, ultraprecision machining and ultrafine materials processing. CIRP Annals-Manufacturing Technology 1983;32:573-82.

[2] Schellekens P. Design for precision: Current status and trends. Annals of the CIRP. 1998;47:557-86.

[3] Wu SM, Ni J. Precision Machining without Precise Machinery. CIRP Annals - Manufacturing Technology. 1989;38:533-6.

[4] Ramesh R, Mannan MA, Poo AN. Error compensation in machine tools — a review: Part I: geometric, cutting-force induced and fixture-dependent errors. International Journal of Machine Tools and Manufacture. 2000;40:1235-56.

[5] Jedrzejewski J, Modrzycki W. Intelligent supervision of thermal deformations in high precision machine tools. PROCEEDINGS OF THE INTERNATIONAL MATADOR CONFERENCE: MACMILLAN PRESS LTD, 1997. p. 457-62.

[6] Sartori S, Zhang G. Geometric error measurement and compensation of machines. CIRP Annals-Manufacturing Technology. 1995;44:599-609.

[7] C.J. Evans JBB. "Structured", "Textured" or "Engineered" Surfaces. CIRP Annals - Manufacturing Technology. 1999;48:541-56.

[8] C. Sodtke PS. Spray cooling on micro structured surfaces. International Journal of Heat and Mass Transfer. 2007;59:4089-97.

[9] W. Gao TA, S. Kiyono, Y. Okazaki, M. Yamanaka. Precision nanofabrication and evaluation of a large area sinusoidal grid surface for a surface encoder. Precision engineering. 2003;27:289-98.

[10] E. Brinksmeier OR, S. Twardy. Tribological behavior of micro structured surfaces for micro forming tools. International Journal of Machine Tools and Manufacture. 2010;50:425-30.

[11] T. Obikawa AK, H. Takaoka, A. Osada. Micro-texture at the coated tool face for high performance cutting. International Journal of Machine Tools and Manufacture. 2011;51:966-72.

[12] K. Tsujino MM. Formation of a low reflective surface on crystalline silicon solar cells by chemical treatment using Ag electrodes as the catalyst. Solar Energy Materials and Solar Cells. 2006;90:1527-32.

[13] A.P. Pop PU, G. BejinaruMihoc. Applications of microlens arrays. Fascicle of Management and Technological Engineering.VI:675-80.

[14] Meinel A, Meinel M, Stacy J, Saito T, Patterson S. Wave-front correctors by diamond turning. Applied optics. 1986;25:997-1007.

[15] Luttrell DE. Machining non-axisymmetric optics. American Society for Precision Engineering-Annual Meeting1990.

[16] http://www.iiviinfrared.com.

[17] Jones R. Parallel and rectilinear spring movements. Journal of Scientific Instruments. 1951;28:38.

[18] G. J. Monkman SH, R. Steinmann, H. Schunk Robot Grippers. 2007.

[19] Rabenorosoa. K HY, Lutz. P, In: Ratchev S, Koelemeijer S Micro-Assembly Technologies and Applications. IFIP International Federation for Information Processing. 2003:235–42

[20] Raghavendra MRA, A. Senthil Kumar, Bhat Nikhil Jagdish. Design and analysis of flexure-hinge parameter in microgripper. The International Journal of Advanced Manufacturing Technology. 2010;49:1185-93.

[21] Howell LL. Compliant Mechanisms: Wiley –Interscience, 2002.

[22] NicolaeLobontiu. Compliant Mechanisms Design of Flexure Hinges: CRC Press, 2003.

[23] Smith ST. Flexures: elements of elastic mechanisms: Gordon and Breach Science Publications, 2000.

[24] Awtar S. Synthesis and analysis of parallel kinematic XY flexure mechanisms: Massachusetts Institute of Technology, 2003.

[25] Howell LL, Midha, Ashok. . The Development of Force-Deflection Relationships for Compliant Mechanism. Machine Elements and Machine Dynamics. 1994;71:501-8.

[26] Paros JM. How to design flexure hinges. Mach Des. 1965;37:151-6.

[27] Awtar S, Slocum A. A large range XY flexure stage for nanopositioning. Proceedings of the 5th Euspen International Conference2005. p. 491-4.

[28] Douglass S. A machining system for turning non-axis-symmetric surfaces: University of Tennessee, 1983.

[29] A.H. El-Sinawi RK. Improving surface roughness in turning using optimal control of tool's radial position. Journal of Materials Processing Technology. 2005;165:54–61.

[30] Al-Zaharnah IT. Suppressing vibrations of machining processes in both feed and radial directions using an optimal control strategy: the case of interrupted cutting. Journal of Materials Processing Technology. 2006;172:305–10.

[31] Brent A. Stancil HMG, and Paul I. Ro. Design of a long range fast tool servo system using magnetic servo levitation. 9th Annual Meeting - American Society for Precision Engineering1995. p. 301-4.

[32] Chopra I. Review of state of art of smart structures and integrated systems. AIAA Journal. 2002;40:2145–87.

[33] Cuttino MWTaJF. Development of a long range, traction drive fast tool servo for diamond turning applications. ASPE Annual Meeting1997.

[34] D. Liu JWS, K. S. Moon, T. J. Sturos, A. R. Kashani. Surface texture improvement in the turning process via application of a magnetostrictively actuated tool holder. ASME Journal of Dynamic Systems, Measurement, and Control. 1998;120:193-9.

[35] DeBra HTaD. Design of a fast short-stroke hydraulic actuator. Annals of the CIRP. 1994;43:469-72.

[36] E. Quandt FC. Magnetostrictive materials and actuators (review). Proceedings of Seventh International Conference on New Actuators2005. p. 100–5.

[37] G.P. Carman MM. Nonlinear constitutive relations for magnetostrictive materials with applications to 1-D problems. Journal of Intelligent Material Systems and Structures. 1995;6:673–83.

[38] H. Eda EO, M. Sahashi, T. Kobayashi. Ultra-precise machine tool equipped with a giant magnetostrictive actuator. Annals of the CIRP. 1992;41:421–4.

[39] H. Eda JS, L. Zhou. Study on ultra-precision machining of ceramics for optical components. The International Society for Optical Engineering1999. p. 420–3.

[40] Hector M. Gutierrez BAS, and Paul I. Ro. Design of a magnetic servo-levitated fast tool servo system for precision turning. IMECE: ASME Dynamic Systems and Control Division. San Francisco, CA1995. p. 491-6.

[41] J.L. Butler SCB, A.E. Clark. Unidirectional magnetostrictive piezoelectric hybrid transducer. Journal of the Acoustical Society of America. 1990;88:7–11.

[42] J.R. Michler KSM, J.W. Sutherland, A.R. Kashani. Development of a magnetostriction based cutting tool positioner. Transactions of the North American Manufacturing Research Institute of SME. 1993:421–7.

[43] Lu X. Electromagnetically-driven ultra-fast tool servos for diamond turning: Massachusetts Institute of Technology, 2005.

[44] M. Weck HO, K. Kehlkopp, and T. Terwei. A new hybrid concept for a long stroke fast-tool-servo system. American Society for Precision Engineering1995. p. 211-4.

[45] M. Weck HO, K. Kehlkopp, and T. Terwei. A long stroke fast-tool servo with air bearings. In: Kunzmann H, editor. Progress in Precision Engineering and Nanotechnology1997. p. 393-6.

[46] M.J. Dapino RS, L.E. Faidley, A.B. Flatau. A coupled structural magnetic strain and stress model for magnetostrictive transducers. Journal of Intelligent Material Systems and Structures. 2000;11:135–52.

[47] Montesanti RC. High bandwidth rotary fast tool servos and a hybrid rotary/linear electromagnetic actuator: Massachusetts Institute of Technology, 2005.

[48] Park G, Matthew T. Bement, Daniel A. Hartman, Ronald E. Smith, and Charles R. Farrar. The use of active materials for machining processes: A review. International Journal of Machine Tools and Manufacture. 2007;47:2189-206.

[49] Ro HMGaPI. Parametric modeling and control of a long-range actuator using magnetic servo-levitation. IEEE Transactions on Magnetics. 1998;34.

[50] Ro HMGaPI. Sliding-mode control of a nonlinear-input system: application to a magnetically levitated fast tool servo. IEEE Transactions on Industrial Electronics. 1998;45.

[51] Shinstock WGaD. Design of a linear voice coil actuator for fast tool servo applications. ASPE 1997.

[52] T. Higuchi TY, and M. Tanaka. Development of a high speed noncircular machining NC-Iathe for cutting a piston-head of a reciprocating engine by use of a new servomechanism actuated by electromagnetic attractive force. Journal of the Japan Society of Precision Engineering. 1989;62:453.

[53] T. J. Sturos JWS, K. S. Moon, D. Liu, A. R. Kashani. Application of an actively controlled magnetostrictive actuator to vibration abatement in the turning process. Proceedings of the ASME Dynamic Systems and Control Division. San Francisco, CA1995. p. 539-44.

[54] T.B. Thoe DKA, M.L.H. Wise. Review on ultrasonic machining. International Journal of Machine Tools & Manufacture. 1997;38:239–55.

[55] Tomizuka T-CTM. Robust adaptive and repetitive digital tracking control and application to hydraulic servo for noncircular machining. Mar 1994;116:9.

[56] Trumper XLaDL. Electromagnetically driven fast tool servo. ASPE 2003 Annual Meeting2003. p. 103–6.

[57] Trumper XLaDL. High bandwidth fast tool servo control. American Control Conference 2004.

[58] Trumper XLaDL. Electromagnetically driven ultrafast tool servo. ASPE 2004 Annual Meeting2004. p. 269–72.

[59] Tsao DHKaT-C. Identification and control of electrohydraulic actuator modeled as a linear periodic system. American Control Conference.

[60] Tsao DHKaT-C. Robust performance control of electrohydraulic actuators for camshaft machining. Fluid Power Systems and Technology: Collected Papers1997. p. 6.

[61] Tsao T-C. Non-circular turning for camshaft machining - fast response actuators, sensors, and motion control for cam profile tracking. In: Lettieri JCBaTR, editor. Advanced Technology Program Motor Vehicle Manufacturing Technology Public WorkshopOctober 1997.

[62] Tsao ZSaT-C. Adaptive repetitive control design with application to an electrohydraulic servo. Fluid Power Systems and Technology1997. p. 15.

[63] Tsu-Chin Tsao RDH, Z. SUD, and A. Babinski. Motion control of non-circular turning process for camshaft machining. Proceedings of the Japan-USA Symposium on Flexible Automation1998.

[64] Wang X. Experimental research on the linear motor micro-feed devices with high frequency response, long travel and high accuracy. Annals of the CIRP. 1991;40:379–82.

[65] Y. Yamamoto HE, J. Shimizu. Application of giant magnetostrictive materials to positioning actuator. International Conference on Advanced Intelligent Mechatronics1999. p. 215–20.

[66] Z. Tang ZX, F. Lv. Modeling and control method study of magnetostrictive micropositioner and its application. IEEE International Conference on Systems, Man, and Cybernetics2004. p. 4296–300.

[67] Patterson S, Magrab E. Design and testing of a fast tool servo for diamond turning. Precision Engineering. 1985;7:123-8.

[68] Falter P, Dow T. Design and performance of a small—scale diamond turning machine. Precision Engineering. 1987;9:185-90.

[69] Falter PJ, Dow TA. A diamond turning apparatus for fabrication of non-rotationally symmetric surfaces. Ultraprecision in Manufacturing Engineering. 1988.

[70] Thomas A. Dow MHM, and Peter J. Falter. Application of a fasttool servo for diamond turning of nonrotationally symmetric surfaces. PrecisionEngineering. Oct 1991;13:243-50.

[71] Falter PJ. Diamond Turning of Non-Rotationally Symmetric Surfaces: North Carolina State University, 1990.

[72] J.F. Cuttino ACM, D.E. Schinstock. Performance optimization of a fast tool servo for single-point diamond turning machines. IEEE/ASME Transactions on Mechatronics. 1999;4:169-79.

[73] Okazaki Y. A micro-positioning tool post using a piezoelectric actuator for diamond turning machines. 12. 1990;3.

[74] Hara Y, Motonishi S, Yoshida K, Ikawa N. A new micro-cutting device with high stiffness and resolution. CIRP Annals-Manufacturing Technology. 1990;39:375-8.

[75] J. D. Rasmussen T-CT, R. D. Hanson, and S. G. Kapoor. A piezoelectric tool servo system for variable depth of cut machining. Precision Machining: Technology and,Machine Development and Improvement, ASME. 1992;PED-58:119-30.

[76] J. D. Rasmussen T-CT, R. D. Hanson, and S. G. Kapoor. Dynamic variable depth of cut machining using piezoelectric actuators. International Journal of Machine Tools and Manufacturing. 1994;34:379-92.

[77] Weck M, Hartel R, Bispink T. Limits of workpiece accuracy caused by the geometrical and dynamical behaviour of ultraprecision diamond turning machines, ultra-precision manufacturing engineering. Proceedings of the International Congress for Ultra-precision Technology, Springer, Berlin1988. p. 153-70.

[78] E. Kouno PAM. A Fast Response Piezoelectric Actuator for Servo Correction of Systematic Errors in Precision Machining. CIRP Annals - Manufacturing Technology. 1984;33:369-72.

[79] W.H. Zhu MBJ, Y. Altintas. A fast tool servo design for precision turning of shafts on conventional CNC lathes. International Journal of Machine Tools & Manufacture 2001;41:953-65.

[80] A. Woronko JH, Y. Altintas. Piezoelectric tool actuator for precision machining on conventional CNC turning centers. Precision Engineering 2003;24:335-45.

[81] Takasu S, et al. Influence of study vibration with small amplitude upon surface roughness in diamond machining. Annals-Manufacturing Technology 1985;34:463-7.

[82] Fawcett SC. Small amplitude vibration compensation for precisiondiamond turning. Precision Engineering. 1990;12:91-6.

[83] Kim J-DKaD-S. Waviness compensation of precision machining by piezoelectric micro cutting device. International Journal of Machine Tools and Manufacture. 1998;38:1305-22.

[84] Kim H-S, and Eui-Jung Kim. Feed-forward control of fast tool servo for real-time correction of spindle error in diamond turning of flat surfaces. International Journal of Machine Tools and Manufacture. 2003;43:1177-83.

[85] Osamu Horiuchi HK, and Noriyuki Ohira. Compensation of therelative motion errors between tool and work in ultra precision machining. In International Progress in Precision Engineering: Proceedings of the 8th International Precision Engineering Seminar. 1995:253-6.

[86] T. Kohno YO, N. Ozawa, K. Mitui, M. Omoda. In-process measurement and a workpiece-referred form accuracy control system (WORFAC): concept of the method and preliminary experiment. Precision Engineering. 1989;11:9-14.

[87] Miller MH, Kenneth P. Garrard, Thomas A. Dow, and Lauren W. Taylor. A controller architecture for integrating a fast tool servo into a diamond turning machine. Precision engineering 1994;16:42-8.

[88] Pahk HJ, Dong Sung Lee, and Jong Ho Park. . Ultra precision positioning system for servo motor–piezo actuator using the dual servo loop and digital filter implementation. International Journal of Machine Tools and Manufacture 2001;41:51-63.

[89] McCue HK. The motion control system for the large optics diamond turning machine (LODTM). 27th Annual Techincal Symposium: International Society for Optics and Photonics, 1983. p. 68-75.

[90] Gao W, Makoto Tano, Takeshi Araki, Satoshi Kiyono, Chun Hong Park. Measurement and compensation of error motions of a diamond turning machine. Precision engineering 2007;31:310-6.

[91] Xu. W. L LH. Piezoelectric actuator based active error compensation of precision machining. Measurement Science and Technology 1999;10:106.

[92] WEI GS. Development of Hybrid Fine Tool Servo System for Nano-machining. 2009.

[93] Park S, Yang S. A mathematical approach for analyzing ultra precision positioning system with compliant mechanism. Journal of materials processing technology. 2005;164:1584-9.

[94] Yong YK, Lu T-F, Handley DC. Review of circular flexure hinge design equations and derivation of empirical formulations. Precision engineering. 2008;32:63-70.

[95] Chen G, Howell LL. Two general solutions of torsional compliance for variable rectangular cross-section hinges in compliant mechanisms. Precision Engineering. 2009;33:268-74.

[96] McClure E. Manufacturers turn precision optics with diamond. Laser Focus World. 1991;27:95-105.

[97] Software Reference Manual, www.deltatau.com/manuals/pdfs/Turbo%20SRM.pdf.

[98] Gao W, Tano M, Araki T, Kiyono S, Park CH. Measurement and compensation of error motions of a diamond turning machine. Precision Engineering. 2007;31:310-6.

[99] Bisshopp K, Drucker D. Large deflection of cantilever beams. Quarterly of Applied Mathematics. 1945;3.

[100] Frisch-Fay R. Flexible bars: Butterworths, 1962.

[101] Mattiasson K. Numerical results from large deflection beam and frame problems analysed by means of elliptic integrals. International journal for numerical methods in engineering. 1981;17:145-53.

[102] Mobility Formula, http://en.wikipedia.org/wiki/Degrees_of_freedom_(mechanics).

[103] Qin Y, Shirinzadeh B, Zhang D, Tian Y. Compliance modeling and analysis of statically indeterminate symmetric flexure structures. Precision Engineering. 2012.

LIST OF PUBLICATIONS

JOURNALS

1. "Design and analysis of Flexure-hinge parameter in microgripper" in THE INTERNATIONAL JOURNAL OF ADVANCED MANUFACTURING TECHNOLOGY Volume 49, Numbers 9-12, 1185-1193, DOI: 10.1007/s00170-009-2478-9.
2. "Single Axis Error Compensation of Ultra Precision Lathe Using Dual Servo Actuation", ASIAN INTERNATIONAL JOURNAL OF SCIENCE AND TECHNOLOGY IN PRODUCTION AND MANUFACTURING ENGINEERING, Vol. 6, No.2, May - August, 2013, ISSN:1906-151X
3. Design and implementation of Single axis Fine tool servo for machine tool enhancement *(Pending)*
4. Development of Novel dual axis planar compliant mechanism for real-time error compensation *(Pending)*

CONFERENCES

1. "Following Error-compensation of Ultra Precision Lathe using Dual-servo Mechanism" 14th International Conference on Advanced Materials and Processing Technologies, Istanbul, Turkey, 13-16 July, 2011, Paper no. DPO-135.
2. "Novel Nano-positioning XY Stage using Flexures" selected for presentation at 5th International Conference on Micro Manufacturing, Wisconsin, USA, 5th -8th April 2010, Paper no. 1876.

3. “A study on various flexure-hinge parameters in a micro-gripper” selected for poster presentation at LAMDAMAP 9th International Conference, UK, 29th June – 2nd July, 2009.

APPENDIX A

Diamond Turning Machine - X/Z Axes

Classification	No.	Item	Units	X	Z
Externals specification	1	Structure	-	Horizontal stage	Horizontal stage
	2	Stroke (Effective)	mm	40	40
	3	Stroke (Maximum)	mm	50	50
	4	Size	mm	800W 800D 400H(Machine), 1200W 1000D 1200 H (with control box)	
	5	Size of table	mm	300 x 200	300 x 200
	6	Mass of moving parts	kg	20	30 (with Spindle)
	7	Mass of unit total	kg	184	
Static accuracy	8	Straightness	µm	0.1	0.1
Dynamic performance	9	Maximum velocity	m/min	10	10
	10	Maximum acceleration	G	0.1	0.1
	11	Feedback		Full closed by linear encoder	
	12	Glass sclae grating	µm	0.02	0.02
	13	Interpolated Resolution	nm	5	5
	14	Following error	µm	±0.1	±0.1
Main mechanical parts	15	Accuator		Linear motor (Sodick CA010D - water cooling)	
	16	Guide		Pin Roller guide (Maker SKF, Model LWRV6)	
	17	Material of main structure parts		Base: Granite, Machine:S45C	
Electrical specification	18	Motion controller		UMAC Analog torque mode	
	19	Voltage		DC85V	
	20	Linear encoder		5nm (Micro-e)	
Environmental condition	21	Motor cooling		Water cooling	
	22	Room temperature	°C	21± 0.5	

APPENDIX B

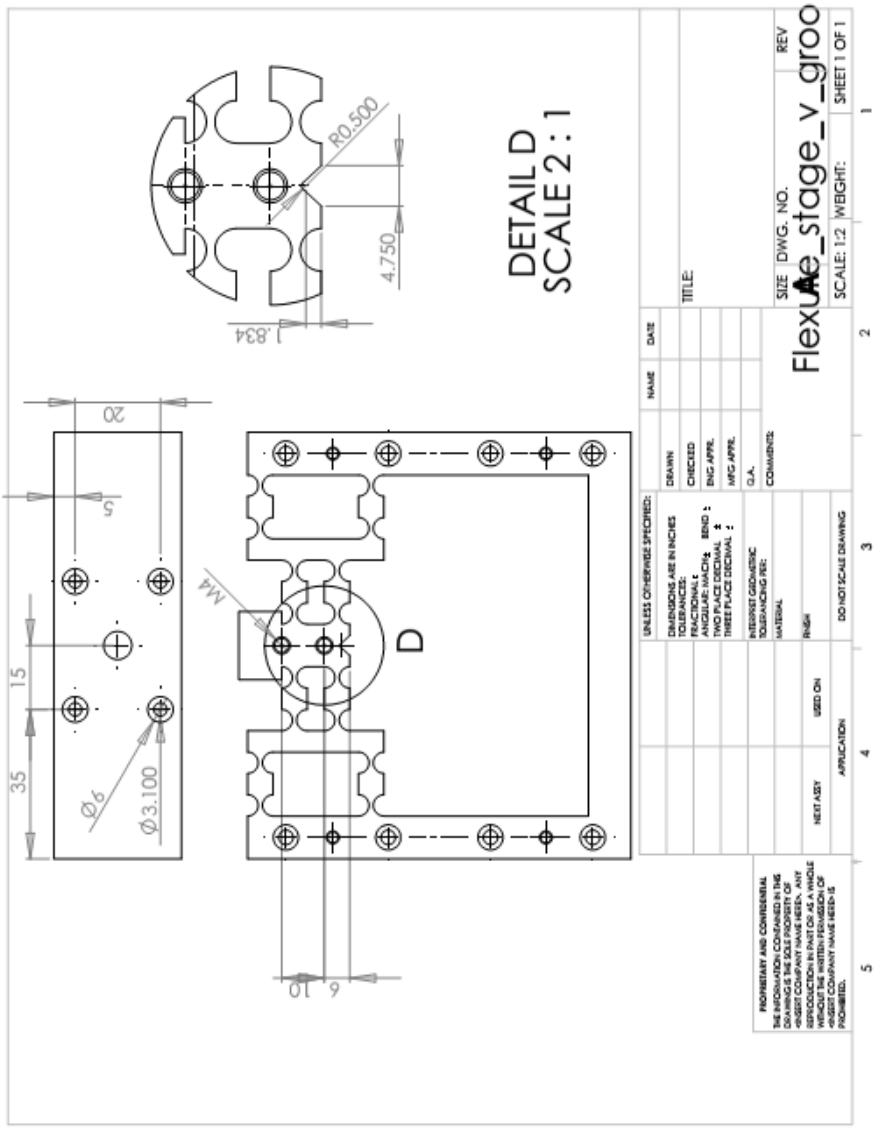
DETAIL D
SCALE 2 : 1
R0.500
4.750
1.834
20
5
15
35
Ø6
Ø3.100
M4
D
6
10
Flexure_stage_v_groo
SIZE
DWG. NO.
REV
SCALE: 1:2
WEIGHT:
SHEET 1 OF 1
TITLE:
DRAWN
CHECKED
ENG APPR.
MFG APPR.
Q.A.
COMMENTS:
NAME
DATE
UNLESS OTHERWISE SPECIFIED:
DIMENSIONS ARE IN INCHES
TOLERANCES:
FRACTIONAL ±
ANGULAR: MACH ± BEND ±
TWO PLACE DECIMAL ±
THREE PLACE DECIMAL ±
INTERPRET GEOMETRIC
TOLERANCING PER:
MATERIAL
Rs64
DO NOT SCALE DRAWING
APPLICATION
USED ON
NEXT ASSY
PROPRIETARY AND CONFIDENTIAL
THE INFORMATION CONTAINED IN THE
DRAWING IS THE SOLE PROPERTY OF
<INSERT COMPANY NAME HERE>. ANY
REPRODUCTION IN PART OR AS A WHOLE
WITHOUT THE WRITTEN PERMISSION OF
<INSERT COMPANY NAME HERE> IS
PROHIBITED.

APPENDIX C

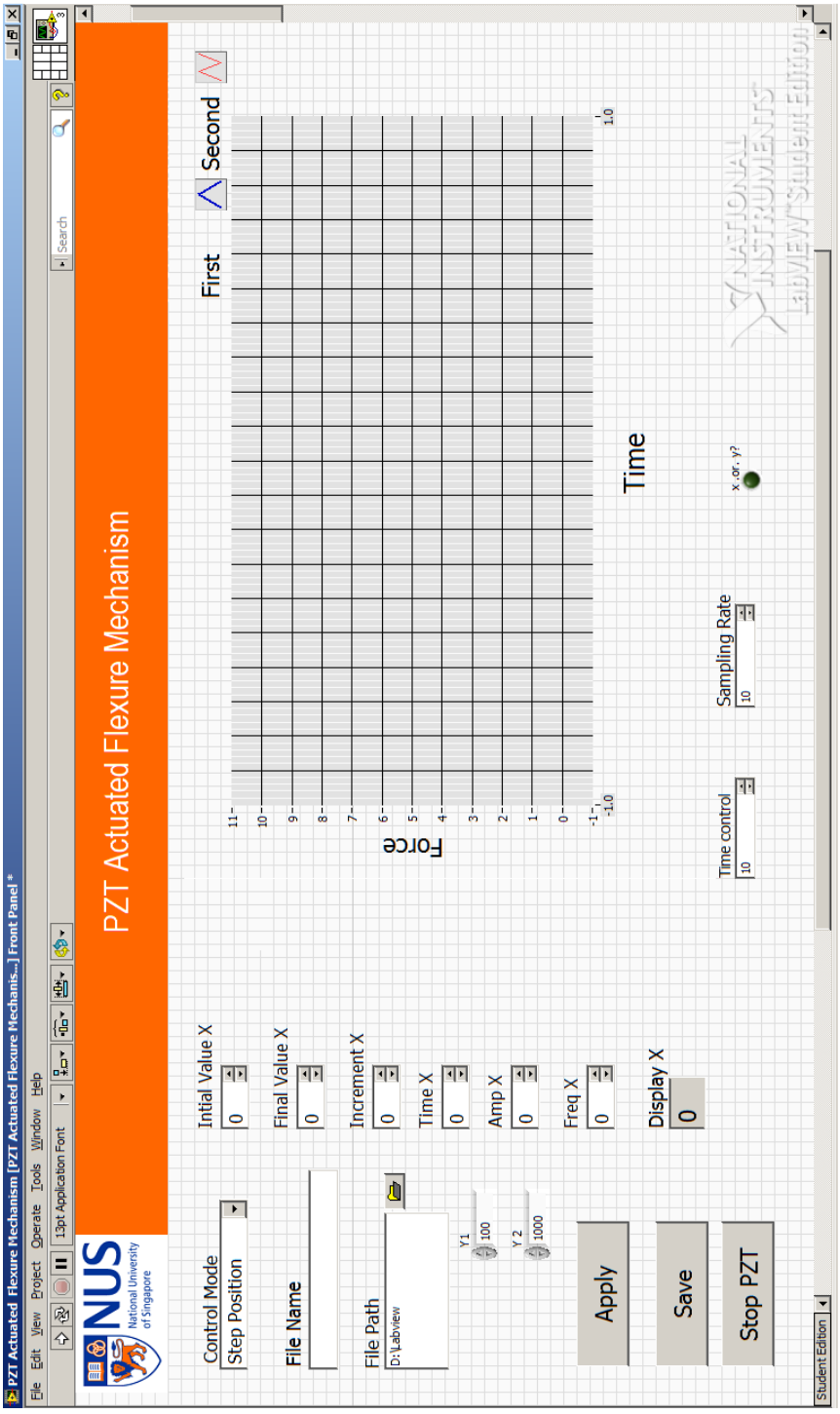
PZT Actuated Flexure Mechanism [PZT Actuated Flexure Mechanis...] Front Panel *
File Edit View Project Operate Tools Window Help
13pt Application Font
Search
NUS National University of Singapore
PZT Actuated Flexure Mechanism
Control Mode
Step Position
Intial Value X
Final Value X
Increment X
Time X
Amp X
Freq X
File Name
File Path
D:\Labview
Y1
100
Y 2
1000
Apply
Save
Stop PZT
Display X
Time control
Sampling Rate
First
Second
Force
Time
x or, y?
NATIONAL INSTRUMENTS
LabVIEW Student Edition
Student Edition

APPENDIX D

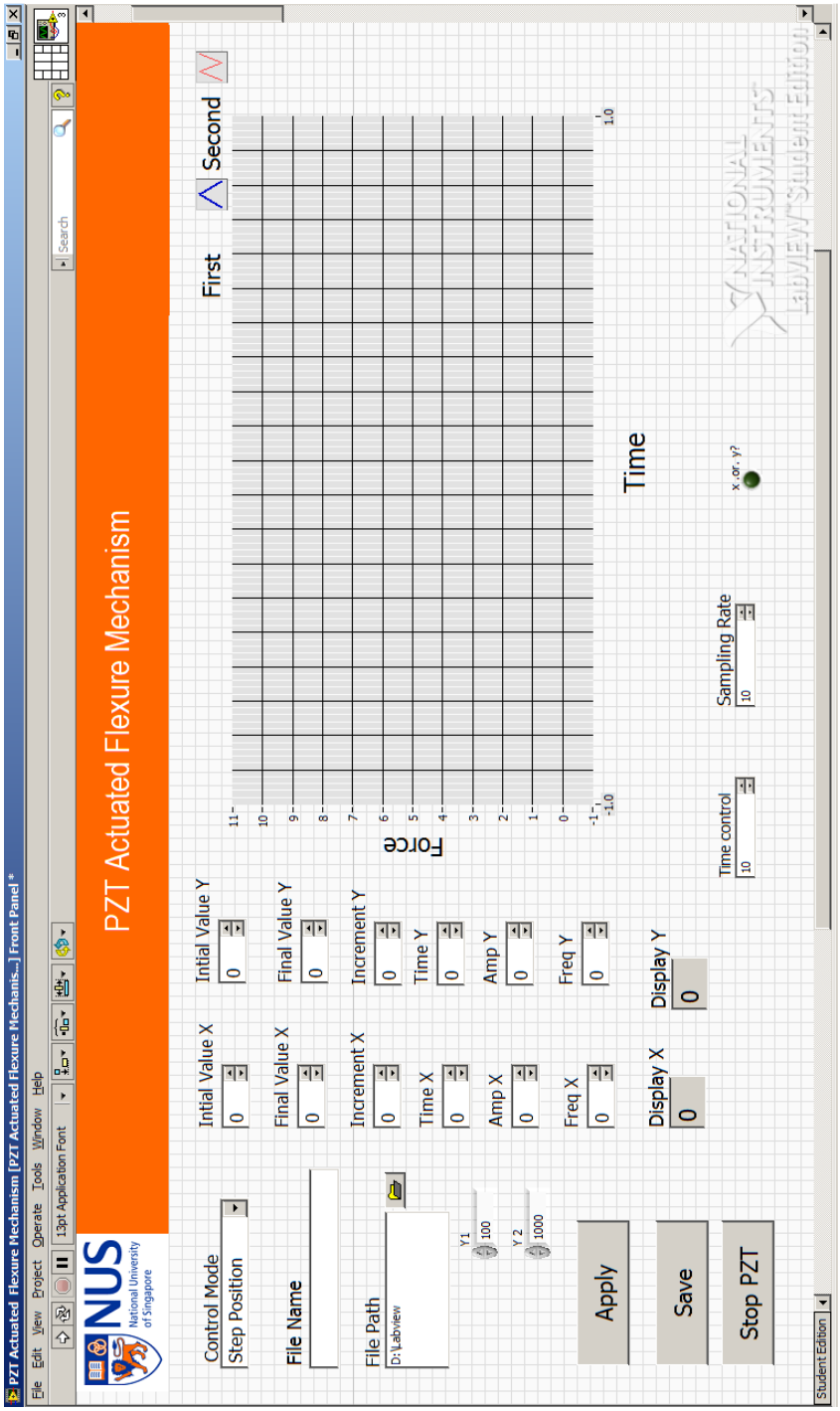
PZT Actuated Flexure Mechanism [PZT Actuated Flexure Mechanis...] Front Panel *
File Edit View Project Operate Tools Window Help
PZT Actuated Flexure Mechanism
NUS National University of Singapore
Control Mode
Step Position
File Name
File Path
D:\Labview
Intial Value X
Final Value X
Increment X
Time X
Amp X
Freq X
Display X
Intial Value Y
Final Value Y
Increment Y
Time Y
Amp Y
Freq Y
Display Y
Apply
Save
Stop PZT
Force
Time
First
Second
Time control
Sampling Rate
x or y?
Student Edition